Politecnico di Torino

Politecnico di Torino

Department of Mechanical and Aerospace Engineering

Master's degree program in Mechanical Engineering
Academic Year 2024/2025

Laser powder bed fusion of AlSi10Mg alloy; productivity and cost analysis

Supervisor:
Prof. Abdollah Saboori

Candidate:
Amin Mohammadzadeh Qamat

Contents

Abstract

Laser Powder Bed Fusion (L-PBF) has emerged as a transformative additive manufacturing (AM) technique, enabling the fabrication of highly intricate metal components with excellent mechanical properties and design flexibility. Among the various alloys used in L-PBF, AlSi10Mg has gained significant industrial relevance, particularly in aerospace and automotive applications, due to its favorable strength-to-weight ratio, corrosion resistance, and thermal stability. However, despite its advantages, achieving an optimal balance between productivity, part quality, and manufacturing cost remains a challenge. This study aims to systematically investigate and optimize the influence of key L-PBF process parameters—laser power, scan speed, hatch distance, and layer thickness—on the densification behavior, surface quality, mechanical performance, and overall economic feasibility of AlSi10Mg components.

To achieve these objectives, an extensive experimental campaign was conducted in which 54 cubic samples were fabricated under varying parameter conditions. The samples underwent a rigorous characterization process that included density analysis using the Archimedes method, X-ray computed tomography (XCT), and metallographic image analysis. Surface quality was assessed using profilometry and optical microscopy, while mechanical performance was evaluated through compression testing. Additionally, a comprehensive cost analysis was performed using a turbine wheel case study to quantify the financial implications of different processing strategies.

The findings of this research reveal that scan speed and layer thickness are the most influential factors in determining relative density, with an optimal volumetric energy density (VED) range identified to maximize densification while minimizing porosity. The results also highlight that laser power and scan strategy play a pivotal role in surface roughness, with higher power levels generally improving fusion but potentially introducing defects if not carefully controlled. Furthermore, a strong correlation was observed between build rate and both part quality and economic efficiency. By optimizing process parameters, it was possible to significantly enhance productivity without compromising mechanical integrity. Compression test showed that optimized parameters preserved high strength and stable deformation, even at higher build rates. The cost analysis demonstrated that adopting higher build rates and batch production can substantially reduce per-part manufacturing costs, reinforcing the importance of process optimization for industrial scalability.

This study contributes valuable insights into the complex interplay between process parameters, material behavior, and economic viability in L-PBF of AlSi10Mg. By presenting a structured framework for parameter optimization, it provides a pathway for improving manufacturing efficiency while maintaining high-performance standards. The findings not only enhance the fundamental understanding of L-PBF processing but also offer practical guidelines for industries seeking to leverage additive manufacturing for high-quality, cost-effective production.

Acknowledgements

I would like to express my heartfelt gratitude to Professor Abdollah Saboori for his invaluable guidance, patience, and encouragement throughout this journey. His expertise and support have been instrumental in shaping not only this research but also my growth as a researcher.

A special thanks to the Integrated Additive Manufacturing (IAM) center at Politecnico di Torino**,** led by Professor Luca Iuliano, for fostering an inspiring and collaborative research environment. The discussions, shared knowledge, and hands-on experiences within the lab have greatly enriched my understanding of additive manufacturing. I am truly grateful to the researchers, and fellow students who have shared their insights, provided technical support, and offered words of motivation along the way. Your support and willingness to collaborate have made this journey both productive and enjoyable.

I also want to extend my appreciation to my friends and family for their constant encouragement and belief in me. Your support, patience, and reminders to take breaks when needed have been invaluable.

This work would not have been possible without the collective contributions of so many people, and I feel incredibly fortunate to have had such a supportive network throughout this experience. Thank you all.

List of Figures

List of Tables

Chapter 1: Introduction

Additive Manufacturing (AM) is a groundbreaking technology that has significantly changed today's manufacturing processes by making it possible to create three-dimensional objects directly from digital models. In contrast to conventional subtractive manufacturing techniques of removing material to achieve the required shape, AM constructs components layer by layer, depositing material only where necessary. This fundamental transformation not only minimizes material waste but also allows to produce extremely complex geometries that are ordinarily impossible to achieve using conventional manufacturing techniques. AM has, in the past decades, evolved from a rapid prototyping technique to a viable means of producing functional, end-use components in a variety of industries. Among the many applications of additive manufacturing (AM), metal additive manufacturing is a game-changing technology, especially in sectors such as aerospace, automotive, medicine, and energy, where precision, performance, and innovation are key. Among such technologies in the domain of metal AM, Laser Powder Bed Fusion (L-PBF) is one of the most developed and versatile technologies.

Laser Powder Bed Fusion (L-PBF) is an advanced manufacturing technique that has transformed the production of high-performance metal parts. The technique works by adding a thin layer of metal powder onto a build platform, which is selectively melted and fused using a focused laser beam. The layer-by-layer process allows to produce complex and detailed parts with high precision and structural integrity. What renders L-PBF specifically beneficial is that it can create geometries that cannot be attained with conventional manufacturing techniques, including internal cooling channels, lattice structures, and light-weight designs. These possibilities have rendered L-PBF an essential technology across industries in which weight reduction, customization, and performance are critical. Aerospace applications, for example, often utilize L-PBF to create parts that are both light in weight but strong, enhancing fuel efficiency and diminishing emissions. L-PBF is also used in the medical field to produce patient-specific prosthetics and implants with precise fit and improved function.

One of the main advantages of L-PBF is that it can process a wide range of sophisticated materials like titanium alloys, stainless steel, nickel-based superalloys, and aluminum alloys. In doing so, L-PBF can meet different industrial applications from the lightweight structures needed by automotive applications to the high-temperature components needed by energy systems. The precision of L-PBF is another defining feature, with layer thicknesses typically ranging from 20 to 100 microns, which allows to produce components with fine surface finish and high detail. Additionally, L-PBF is extremely environmentally friendly in that it minimizes material wastage and allows for easy reuse of unused powder, which aligns with global efforts at adopting greener production methods.

Among the materials commonly used in L-PBF, one of the most widely used for lightweight and high-strength applications is AlSi10Mg. AlSi10Mg is an aluminum-silicon alloy containing magnesium with excellent mechanical properties, corrosion resistance, and thermal stability. All these characteristics render it extremely suitable for application in fields where lightness and performance are critical, such as aerospace and automotive. In aerospace, the alloy finds extensive application in the manufacture of structural components, brackets, and heat exchangers owing to its lightweight nature, which enhances fuel efficiency and diminishes emissions. In the automotive industry, AlSi10Mg is employed in the manufacture of engine components, brackets, and other parts where a compromise between strength and thermal conductivity is required. L-PBF's high cooling rates also enhance the microstructural properties of AlSi10Mg, such as increased tensile strength, fatigue life, and dimensional stability. Such properties have made AlSi10Mg a suitable material for prototyping and large-scale production in hostile environments.

Despite its numerous benefits, the industrial use of Laser Powder Bed Fusion on a large scale is confronted with a variety of challenges. Finding a balance between productivity, quality, and cost is one of the primary challenges. The L-PBF process is highly parameter-sensitive, and parameters such as laser power, scanning speed, hatch distance, and layer thickness play a vital role in deciding the ultimate characteristics of the part. Lack of control of the above parameters leads to defects such as porosity, residual stress, and anisotropic mechanical behavior that compromise the performance as well as reliability of the parts. Additionally, L-PBF cost remains a significant barrier because of the high price of metal powders, energy consumption, and operation of the machine. These economic challenges, along with the need for post-processing procedures such as heat treatment and surface finishing, also complicate the scalability of L-PBF for mass production.

The focus of this research is to bridge these gaps and explore the possibilities of L-PBF in the optimization of AlSi10Mg part production. By analyzing the effects of key process parameters on productivity, quality, and cost, this study aims to provide valuable information on the optimization of L-PBF for industrial applications. The study particularly investigates critical quality attributes like surface roughness, density, porosity, and microstructure to establish a profound comprehension of their interlinks with process parameters. Moreover, a comprehensive cost analysis is carried out to unveil methods aimed at minimizing operational costs while upholding high-quality results. The primary objective is to give a comprehensive framework that will be utilized in advancing L-PBF processes to produce AlSi10Mg parts that satisfy the requirements of contemporary industries without sacrificing economic efficiency.

This dissertation is organized in a manner that methodically deals with the research aims and gives a comprehensive understanding of the subject. The introductory section delineates the background and scope of the study, highlighting the overriding importance of Laser Powder Bed Fusion and the application of AlSi10Mg in industrial practice while stating the primary challenges linked with the process. The second chapter synthesizes the state of the art, covering new trends in L-PBF technology, the influence of process parameters, and the gap in research studies. The third chapter

describes the material and methods used in the study, including the experimental setup, process parameters, and techniques for productivity, quality, and cost evaluation. Chapter four presents and discusses the results, analyzing critically the interrelationships between process parameters, part performance, and economics. Lastly, chapter five concludes the thesis by summarizing the findings.

By addressing these critical aspects, this thesis aims to contribute to existing literature on Laser Powder Bed Fusion and its application in AlSi10Mg alloy, and hence pave the way for more extensive industrial implementation of this new generation production technique.

Chapter 2: State of the Art

2.1. Additive Manufacturing (AM)

Additive Manufacturing (AM), alternatively referred to as 3D printing, is a modern production technology that creates three-dimensional (3D) parts through an additive process, adding them layer by layer.

Fundamentally, AM is in contrast with traditional manufacturing processes, which involve predominantly material subtraction to produce parts, such as machining, or molding materials into a desired shape. In contrast, AM creates parts directly out of a computer model, adding material in incremental form exclusively in regions considered to be in demand.[1], [2]

Despite the increasing number of variations in AM technology, all follow a similar sequence of sequential operations. AM processing begins with part conceptualization and creation with Computer-Aided Design (CAD) software specifically designed for AM use. In this stage, not only is part geometry determined, but tolerance, material property, and end-use requirements are included in consideration, too.

Once completed, the part is translated into a Standard Tessellation Language (STL) file, in which the model is discretized into thin, two-dimensional sections. Next, preparation for printing involves modifications in its orientation, dimensions, and location in preparation for build efficiency and compatibility with printing device capabilities. The following stage involves AM apparatus configuration, in which settings such as layer height, material, and environment (e.g., temperature, atmosphere) are determined.

Construction of the part itself is largely an automated process. The AM machine builds the part through the exact deposition of material, one layer at a time, as per the digital design, by means of consolidated processes such as extrusion, melting, or curing such that once that layer is laid down, it solidifies before another layer can be added. Once the object is finished, it is removed from the machine, usually needing careful handling so as not to damage it.

Depending on the purpose, the part could need further post-processing steps-such as support removal, surface finish, or heat treatment to achieve functional, dimensional, or aesthetic specifications. In the end, the finished part is now ready for application, be it as a prototype, a functional component, or a custom solution. (Figure 1)[3]

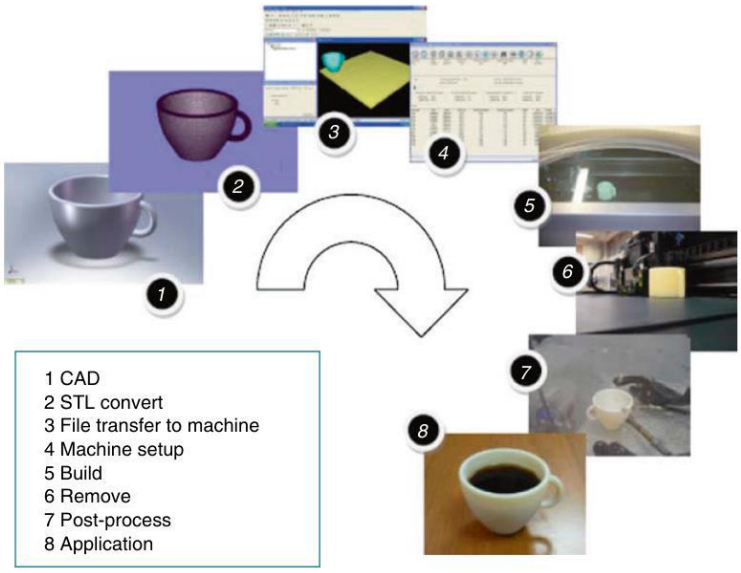

Figure 1: overall route of AM process starting from CAD model to the final part.[3]

Additive manufacturing overlaps with a plethora of technologies that are categorized depending on how material is deposited and consolidated-inherently varying with respect to light-cured vat photopolymerization, material extrusion, and powder bed fusion, which is melting selectively targeted areas of a powder bed using a laser or an electron beam, To extend the reach of AM, there are other methods: those of binder jetting, in which a liquid binder is selectively deposited onto a powder bed to bond like-particle powders; sheet lamination, in which thin sheets of material are adhered together by glue, heat, or ultrasonic welding; and directed energy deposition, where powder or wire is fed into a focused energy source, such as an electron beam or laser, to then be melted and deposited-which allows AM to address a wide variety of needs in the industrial and commercial arenas. [4]

Several types of materials have been deployed in AM applications for specific purposes. These include polymers, metals, ceramics, composites, and even biological materials. Materials are supplied in various forms-a powder, liquid, or solid filament-depending on the technology employed.

2.2. Metal Additive Manufacturing

With metallic powders, wires, or other forms of feedstock at the heart of Metal AM, production of essential components has reached a new level of high performance and high technological complexity, proving to be a critical and fundamental tool in areas that demand high-level precision, strength, and durability.

Powder Bed Fusion (PBF), which includes the process of application of very fine layers of metal powder on a build plate, is one of the most used technologies. In PBF, the powder is subjected to selective melting on each layer of the part by a high-energy source such as a laser in Laser Powder Bed Fusion (L-PBF) or an electron beam in Electron Beam Melting (EBM). These repeating iterations create highly precise components with exceptional mechanical properties and represent some of the highest quality surface finishes. [5], [6]

Another important Metal AM method is Directed Energy Deposition (DED), which deposits metal powder or wire directly into a melt pool created by a focused energy source, such as a laser or electron beam. Not to be confused with PBF, DED is not limited to a powder bed for manufacturing, which means it can work with great flexibility to produce large component parts or for the repair of desirable parts that could otherwise be considered scrap. This type of repair application is for turbine blades, where DED great flexibility is in its ability to add material where needed, allowing the component to return to full function. The downside is that DED precision is somewhat less than PBF methods.[7]

Binder Jetting is another option for powder-form metal additive manufacturing and is characterized by high-speed production. In this process, the liquid binding agent is selectively jetted on a bed of metal powder, fusing the particles together into a green part. After that, the green part goes through the removal of the binding agent in a furnace, followed by its final cooling and dry solidification from a powder to achieve its final properties.[8] Although Binder Jetting provides strategic opportunities for the efficient manufacture of larger parts, shrinkage during the sintering stage must be managed correctly to ensure dimensional fidelity.

Metal Extrusion, a derivation of material extrusion, utilizes metal-filled filaments or pastes deposited layer by layer through a nozzle. Following extrusion, parts undergo debinding and sintering to achieve their final properties. Though Metal Extrusion is less mature compared to other Metal AM technologies, it is rapidly growing in popularity as an economically viable means for prototyping and for small-scale production.[9]

The metal AM process known as sheet lamination-a uncommon method-involves the bonding together of thin metal sheets, which are then cut to shape. This technique works well for making laminated structures and is the second most used, mainly for niche applications.

The selected materials for Metal AM process are once again fine-tuned and optimized for meeting the stringiest requirements of several industries. Most prominent among these are titanium alloys, which are crucial in aerospace application and medical implants because of their outstanding

strength-to-weight ratio, corrosion-resistant, and biocompatible.[10] Nickel-based superalloys are extensively used in jet engines, gas turbines, and other applications within energy sectors in which oxidation resistance and durability are crucial.[11] Stainless steels provide a strong combination of wear resistance, strength, and corrosion resistance, making them applicable for industrial, tooling, and automotive components.

Aluminum alloys, particularly those like AlSi10Mg, have been regarded as essential for aerospace and automotive industry due to their lightness and high thermal conductivity, thus contributing to fuel efficiency and energy conservation.[12] Cobalt-chrome alloys have been widely employed for medical applications in dentistry, orthopedic implants, and prosthetics, among others, owing to their biocompatibility and wear resistance.[13]

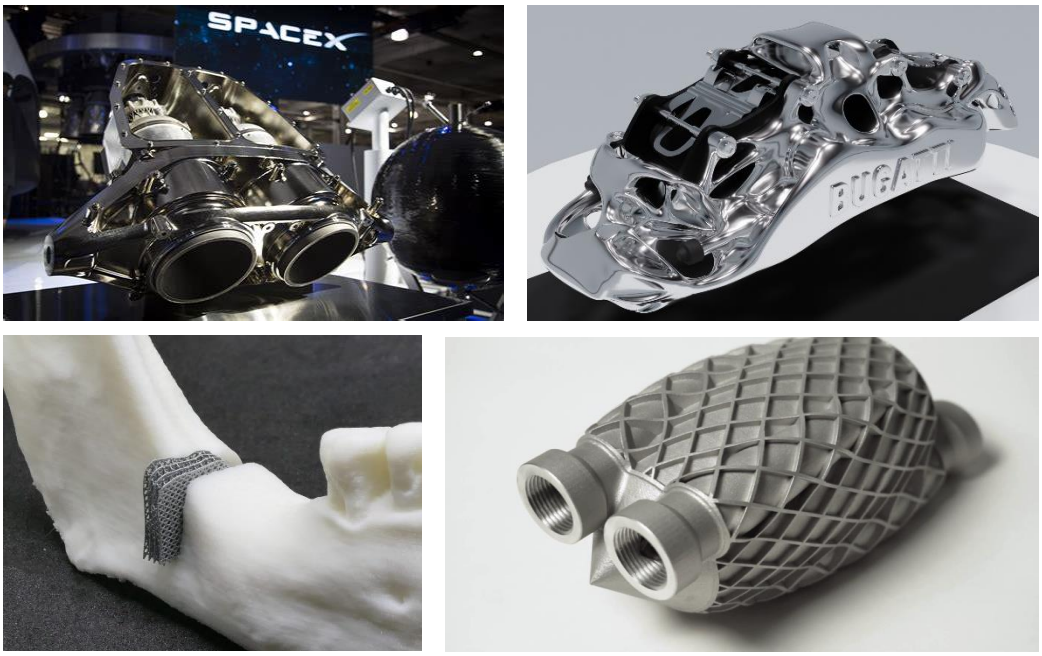

Figure 2: Metal AM aplications: SpaceX's SuperDraco engine chamber, Bugatti brake caliper, A patient-specific medical implant, Heat Exchanger

Metal AM is a great innovation in the field of aviation, such as in the manufacture of different aircraft components including brackets, fuel nozzles, and structural support in which the weight is lessened, or functionality improved. With the internal cooling channels, optimization of aerodynamics, and lightweight lattice structures, ease of manufacture that offers significant fuel efficiency improvements and emission reduction for the entire production process, has made it easy for the manufacturer while increasing performance [14], [15] .In the automotive sector, Metal AM forms a greater part of the tooling for the manufacture of certain high-performance components such as turbocharger housings, custom fixtures for other parts used, as well as accounting for urgency in the making of samples in the design drafting phase. In this sector, Metal

AM has created customized implants for the patient, such as hip and knee replacements, and specially designed, highly precise surgical instruments. This is achieved owing to its ability to copy intricate anatomical structures. Metal AM is used in the manufacture of other components like turbines, heat exchangers, and other high-temperature applications aimed to grant good performance with reliability even under extreme conditions in the energy sector.[16] Figure 2 shows some application of metal additive manufacturing in industry

2.3. Laser Powder Bed Fusion (L-PBF)

L-PBF is a new and promising additive manufacturing technology, building increasingly complicated and precise components layer by layer. It uses the enormous energy of a finely controlled laser beam to selectively fuse powdered material, meaning L-PBF constructs objects directly from digital designs. It is acclaimed for making forms with remarkable complexity and accuracy.[14]

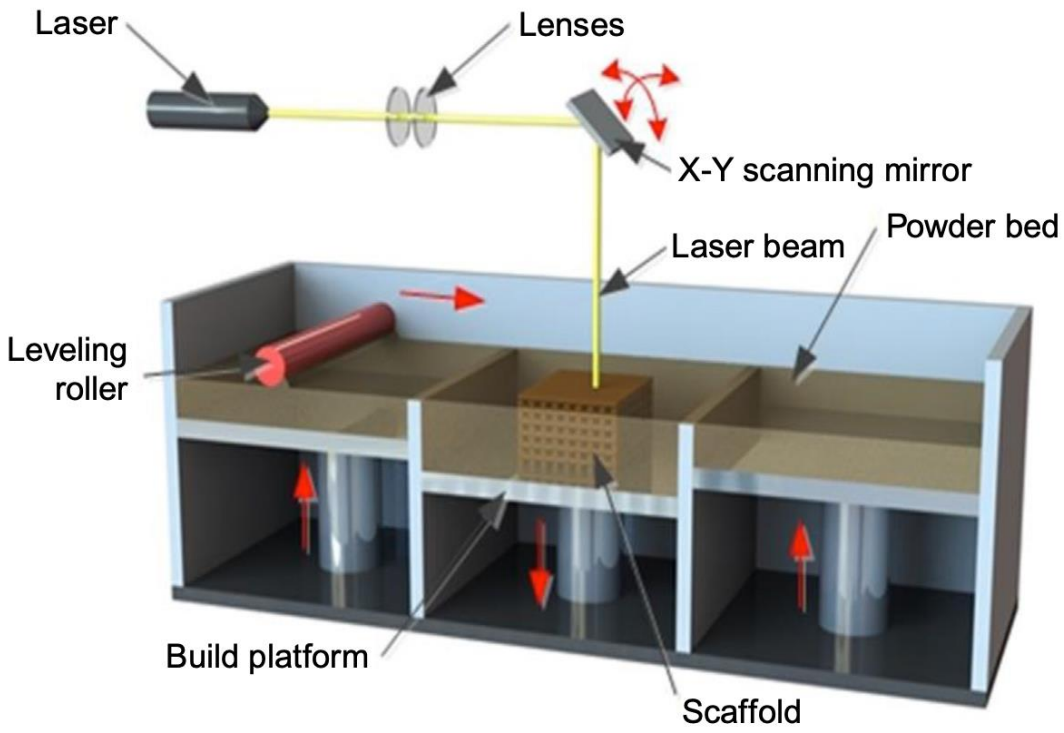

Figure 3: Schematic of the Laser Powder Bed Fusion (L-PBF) Process

At the start of the L-PBF process, the powder bed is carefully prepared to form the base for building the object. Powdered metal, polymer, or ceramics are usually the starting materials. Ensuring a very thin, even layer, between 20 and 100 microns, is deposited on a flat build platform. There needs to be a consistent distribution of powder to obtain intimate fusion and structural qualities in

the build. A specialized mechanism (for instance, a blade or roller) achieves this uniformity. This process is performed in a controlled atmosphere, most commonly an enclosure with an inert gas (typically argon or nitrogen) to prevent the powder from becoming oxidized or absorbing moisture from the air. The necessity of such a controlled atmosphere is further enhanced when reactive and high-performance materials, like titanium or aluminum alloys, are involved.[15]

Once the powder bed is established, we move straight to the heart of the L-PBF process. A high-power laser guided by a three-dimensional (3D) digital model traces the cross-section outline of the object on the powder bed. The laser selectively melts the powder in precise areas corresponding to the design, thereby turning the powder into a solid layer of the object. The heat generated by the laser is intense and carefully calibrated to ensure complete melting and bonding of the particles without overheating or distorting the material. The movement of the laser is governed by advanced optics such as galvanometer mirrors, which guide the laser path with extremely high precision and speed and every melted section sets seamlessly to older portions, creating a robust continuous layer.

After completing one layer, the build platform will descend by a minute distance equal to the thickness of the next layer. A fresh layer of powder is then respectively spread over the fused material, and the process is repeated. This stepwise mechanism permits the object to grow in increments, with each succeeding layer perfectly uniting with its predecessor.

Once the last layer is prepared, the build platform will hold the finished object adorned with powder that did not melt around it. Powder removal is very important as the unfused powder is usually removed using vacuuming, air jets, and sieving techniques. Remaining powder is normally recycled for use in other builds, reducing material wastage and thereby rendering L-PBF a sustainable alternative to traditional subtractive manufacturing. The removed object commonly referred to as the "green" part shall then undergo further post-processing in order to meet specification requirements and improve properties.[16]

Post-treatment processes vary widely according to both the application and the material. However, conventional post-treatment could be thermal treating to mitigate internal stresses induced in the build process as a result of the rapid heating and cooling steps. It could enhance its mechanical properties and its toughness.[17] Additional surface finishing techniques, such as polishing, machining, or surface coating, may be frequently performed to achieve the desired visual appeal and functional attributes. In aerospace applications, for example, parts are polished to reduce drag, while in medical applications, biocompatible coatings are frequently applied to implants.

Another advantage is that L-PBF has the capability to produce complex geometries that were once deemed to be impossible to manufacture. Utilizing the high-power laser, the process rapidly forms a part by selectively fusing fine powder material layer by layer, hence allowing the production of parts with inner channels, lattice structures, and undercuts, all nudging away from tooling and mold processes. [18]This design freedom allows new possibilities in aerospace applications, requiring weight-saving components with optimized geometries, and in the medical industry, where there is an increasing demand for highly customized features on patients' implants.

Another significant advantage is that L-PBF is very material efficient. Unlike ordinary subtractive methods, where a huge block is being cut and hence waste material is generated, L-PBF uses only what is necessary for the generation of individual layers. The excess powder is not fused, and is often recycled and sieved for further use, which lowers excess powder, which in turn lowers material costs, and drastically cuts down on waste of materials. Apart from this, L-PBF fabricates parts with superior mechanical parameters. The energy inputs from the laser completely melt the material, producing on the order of almost full density and similar mechanical strength as that achieved by using other forms of conventional methods. As such, L-PBF emerges as the right choice for safety and serviceability in crucial applications in the aerospace and automotive industries.

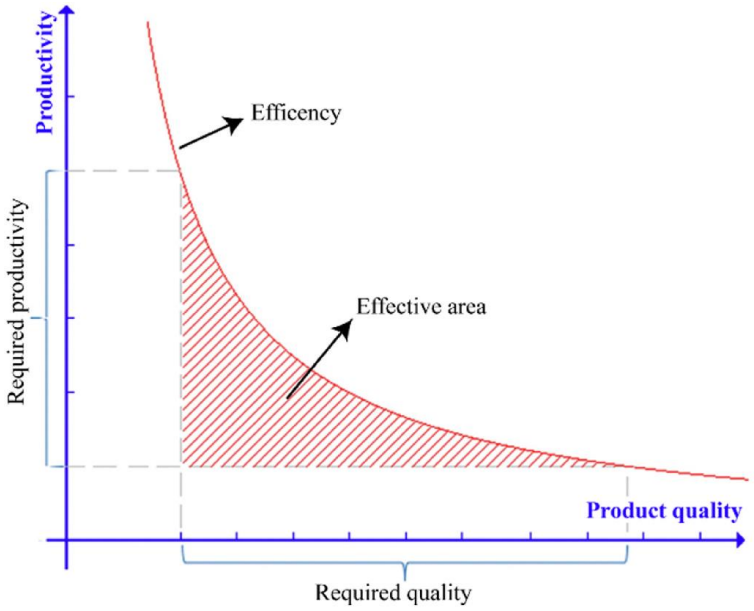

Figure 4: Basic principles of L-PBF that are inversely related to its expansion and range of application compared with conventional metalworking processes [19]

While L-PBF presents great advantages, it still holds several limitations. Slow build rate is one of its biggest challenges. Because of the layer-wise nature of the process, large components or highly intricate details can take many hours or days to accomplish.

Unfortunately, mass production is hardly an option when compared to conventional means of production. Some L-PBF parts undergo considerable post-processing. Post-printing, the introduced internal stresses, due to rapid thermal cycling, may need relieving by heat treatment. Surface finishing requirements such as polishing or machining often arise to ensure texture and dimensional accuracy, especially for critical applications. So, to produce components with enhanced accuracy and quality, the L-PBF machine is limited by a substantial production time, resulting in a drastic productivity reduction, as shown in Figure 4.

In addition to production speed, operating cost is another consideration. The capital cost of equipment is high: industrial L-PBF systems employ advanced lasers requiring costly optics and robust environmental controls. The materials for L-PBF, particularly fine metal powders, are expensive owing to stringent quality requirements with respect to particle size and composition. These factors further contribute to the inaccessibility of the process to small-scale manufacturers or those on a tight budget.[20]

Another area of importance in L-PBF systems is environmental control. The build chamber is filled with inert gases to prevent oxidation or contamination of the powder during fusion, adding further complexity to L-PBF operation and maintenance. Due to health and safety risks surrounding fine powders used in L-PBF, specific facility management and protocols must be carried out. Researchers have, therefore, adopted varied innovative techniques focused on productivity and applicability enhancement in L-PBF. One such application attracting substantial interest is the multi-laser systems. In such systems, several regions of the powder bed are melted simultaneously, therefore increasing the build rate and possibility for fast production cycles.[21] Along with it, there also exists an increasing interest in using powders with preheating treatment since preheated powders consume less energy for melting, thus allowing faster melting and solidification. This not only improves efficiency but also enhances the quality of the final products.[22]

Scanning strategy improvements are yet another important advance in optimization thus impacting L-PBF processes. Various scanning strategies like bidirectional scanning and checkerboard patterns are likely to decrease build time without conceding part quality. These strategies ensure a divergent scanning of the parts so that material can be evenly distributed across the build platform and ensure homogeneous fusion of materials.[23]

A further transformative advancement in the L-PBF landscape incorporates Artificial Intelligence (AI) and Machine Learning (ML) algorithms. The real-time optimization of process parameters such as laser power, scan speed, and layer thickness, which leads to faster and more efficient

production, rests upon these technologies.[24] The incorporation of AI and ML not only allows productivity enhancement but also reduces material wastage and production costs, demonstrating their ability to revolutionize the field of additive manufacturing. [25]

L-PBF technology evolution continues to focus on the improvement of productivity and part quality.

Key parameters such as laser power, scan speed, and hatch distance have all been extensively studied concerning efficiency and quality of the L-PBF process. These parameters are critical in establishing overall productivity as well as structural integrity of the final product. Hence, the study presents an in-depth analysis of key process variables affecting manufacturing performance, subsequently describing equation-based models for productivity and cost evaluation, paving the way for optimization. Furthermore, the study also identifies major strategies for achieving maximum build rate parameter combinations.

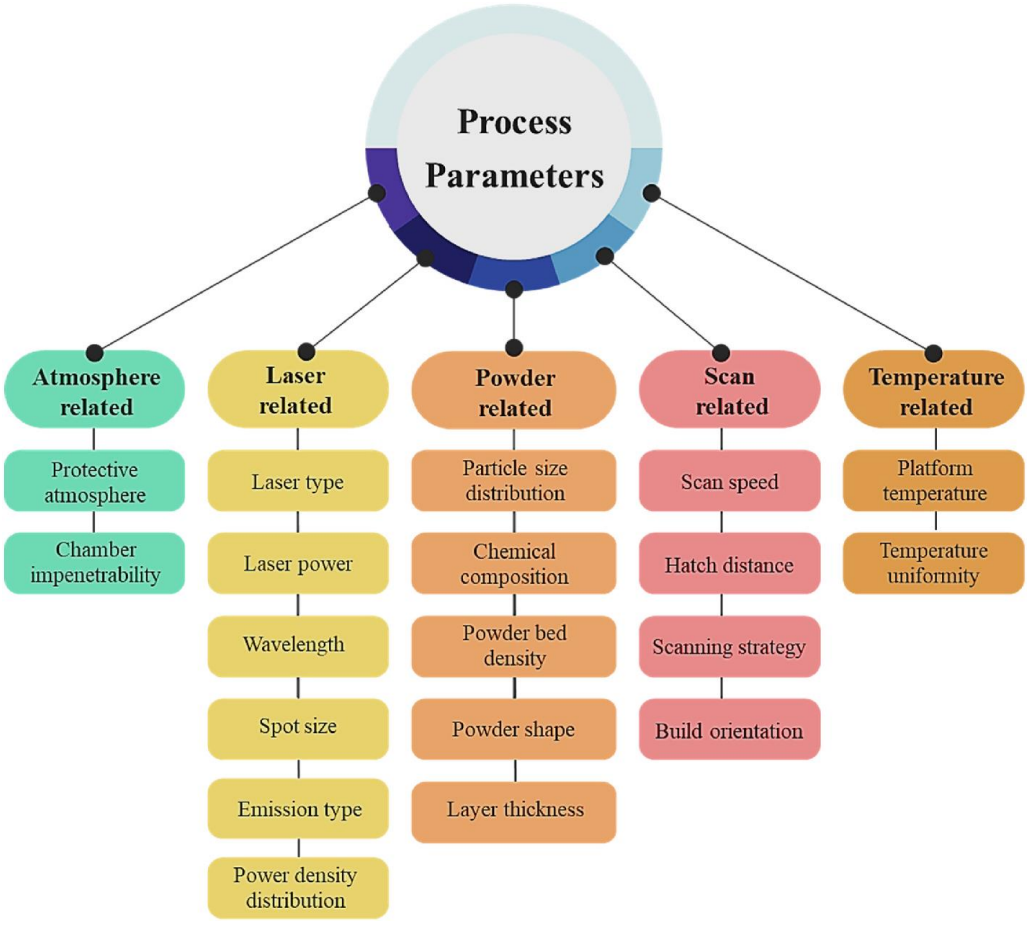

Figure 5: classificaton of process parameters

2.4. Process Parameters

The conditions for processing in various Laser-Powder-Bed-Fusion (L-PBF) systems consist of a combination of fixed machine settings and adjustable process parameters, which usually can be altered to suit some specific manufacturing need. Modern L-PBF systems have over 100 processing parameters arranged in 5 general categories: laser-related, scan-related, powder-related, atmosphere-related, and temperature-related ones (Figure 5). This division is meant to display the intricate entanglement of variables working together to influence the L-PBF.[26]

Parameter optimization in L-PBF is pursued for many goals: 100% densification, high dimensional accuracy, the lowest surface roughness, and maximizing mechanical performance. The exact parameters selected for change often depend on the alloy being used and the final application of the manufactured component, allowing for tailoring the process to meet various industrial needs to a large degree.[27]

The mechanical performance, cost-efficiency, and overall production quality of an object produced via L-PBF are affected by many variables, out of which a few will have a pronounced effect. Important factors affecting the trade-off between speed, cost, and quality of the finished product include laser power, scan speed, hatch distance, layer thickness, and scanning strategy.[28], [29]

The interaction between the key parameters has often been assessed using aggregate metrics, giving a more global picture of how they interfere with one another to contribute to the process. A more rigorous examination of their effects on densification and integrity of the material will follow and thus highlighted their importance inside the L-PBF paradigm. The importance of parameter optimization in enhancing the industrial use of L-PBF technology is a major leverage point that this insight emphasizes.

2.4.1. Laser power (P)

laser power strongly dictates the temperature gradient across the powder bed, so influential in melting behavior and key material characteristics such as density, surface quality, morphology, and mechanical properties.[30] The correct laser power setting involves considering several factors, namely the melting point of material, platform temperature, overlapping effect of layer thickness, scanning speed, and hatch distance, where all together yield proper fusion of the processed substrates.

Generally, increased laser power results in the production of denser parts with lesser porosity. This relationship was established by Pragana et al., who argued that very high laser power settings would yield acceptable density levels, allowing for more freedom in adjusting other process parameters[31] Likewise, Leicht and Cacace showed how running the laser at its maximum allowable power at 200 W enabled the optimizing of various properties of the produced components by varying other parameters.[32], [33]

On the other hand, increased power tends to have drawbacks during extreme magnifications. Excessively increased laser power causes vaporization phenomena and melt-pool instability causing residual stresses, curling, and deformation of parts. [3] On the contrary, owing to high dimensional accuracy, low laser power is also susceptible to low densification and more chances of layer delamination. This trade-off makes it essential to balance laser power to optimize mechanical properties along with process efficiency.[3]

With varying laser power capabilities, modern L-PBF systems are very versatile. Conventional machines are typically in the range of 100 W to 400 W, and state-of-the-art systems have approaches of power of about 1 kW. These advanced laser systems, generally with dual or quad laser arrangements, help boost productivity tremendously by augmenting the number of alloys being processed and economically producing large parts.

The effects of laser power exerted on the microstructure and material properties have been researched extensively. Keller et al., for example, studied the effects of varying laser power during a rescanning strategy on the performance alloy Hastelloy X. They found that lowering the laser power by 40% during the second scan improved mechanical properties, thereby emphasizing the possible dynamic changes of power.[34], [35] In similar research, high-power lasers increased production rates, but caused coarser microstructures, decreased hardness, and reduced yield strength, as stated by Montero-Sistiaga et al. This illustrates the complex relationship between laser power and material performance. [35]

New approaches for controlling laser power are being developed. Ho Yeung et al. propose a laser power control method driven by the geometric conductance factor (GCF), dynamically adjusting laser power depending on the ratio of solid to powder material next to the melt pool. Improvements were seen in melt pool intensity and part qualities like surface finish and distortion.[36]

Overall, high-power lasers, generally coupled with advanced scanning strategies and optimization algorithms, represent some of the latest advancements in L-PBF technology. These advancements have been instrumental in advancing productivity, material flexibility, and component quality, achieving cost-effective and efficient manufacture of complex parts for diverse industries.

2.4.2. Scan speed (V_s)

Scanning speed is an important parameter in Laser Powder Bed Fusion (L-PBF) signifying the forward velocity by which the laser beam traverses the powder bed. This parameter is heavily responsible for altering the energy input to the melting process, thus affecting the surface quality of the manufactured part and the overall speed and efficiency of production. [37]

Today's L-PBF machines can theoretically be operated at an extremely high scanning speed up to 10,000 mm/s, according to technical datasheets. In research and industrial practice, however, most applications would be within the range of 220-3000 mm/s.[38], [39] Scanning speed must be calculated as it has a direct impact on some process parameters. Higher scanning speeds improve productivity by reducing build time but may also result in insufficient melt pool heating and low dwell time-conditions that may have caused incomplete melting, increased porosity, formation of defects, and higher residual thermal stresses.[40] Therefore, to solve these problems, scan speed should be combined with sufficient laser power and hatch distance parameters to obtain dense and defect-free material.[41]

The links between scanning speed and material characteristics have been studied extensively. For example, Liu et al. examined its influence on 316L stainless steel production using L-PBF, establishing that reduced scanning speeds allowed the formation of fine grains with high-low angle grain boundaries and fine cellular structures. These improvements at the microstructural level led to an enhancement in ultimate tensile strength (UTS) and total elongation of the material.[42] In parallel, Mohd Faizal Sadali et al. investigated Ti6Al4V parts and found that scanning speed at 775 mm/s produced high integrity surface morphology and microstructure with very minimal splashing and balling effects.[43] The above clearly illustrates the necessity to optimize the scanning speed for generating demanded mechanical properties along with good surface characteristics.

Scanning speed also influences the dynamics of the molten pool in L-PBF. An example is the work of Weihao Yuan et al., who carried out numerical simulations and experimental tests to study the temperature and velocity fields within the molten pool at different scanning speeds.[43], [44] Their experiments were able to distinguish three distinctly different states of the molten pool-unstable, transitional and stable-with the dynamics of these states influencing surface defects and bulk density. A slight depression in the melt pool induced by recoil pressure was noted to enhance bulk density, while excessive energy input could lead to keyhole formation giving rise to residual porosity. All these observations highlight how delicate the balance must be to optimize scanning speed for desired materials and process results.

The productivity gained from high scanning speeds speaks for itself, as it can effectively cut down build time by half if scanning speed is doubled. However, this is contrary to the trade-offs with

material density and quality, where applications will sometimes permit slightly lower density but compromising quality for the sake of maximizing build rate will diminish the performance of the component.[45] Thus, the balance of productivity and quality is still considered a great challenge in obtaining an optimized L-PBF process, increasing the need for tighter control of scanning speed and its correlation with other parameters.[46]

With support from ongoing research and innovations, scanning speed is creating yet another opportunity for the improvement of efficiency and material performance in L-PBF. Thus, its paramount importance in contemporary additive manufacturing can never be overstated.

2.4.3. Hatch Distance (h)

The hatch distance is another important variable in laser powder bed fusion (L-PBF), which is defined as the distance between two parallel laser tracks. Together with laser spot size, this parameter also influences powder melting and promotes a strong bond between adjacent tracks. As can be seen in Figure 6 he intentional overlap between laser passes discourages the formation of defects such as pores or unfused areas that are detrimental to the density of the L-PBF parts and their structural integrity. Smaller hatch distances produce more overlap, contributing to surface quality, reduced porosity, and better mechanical properties. [47] However, excessively small hatch distances bring in problems, ranging from increased energy density that creates overheating along the edges of the laser track, distortion and warping of the processed layer, increased scanning time, and higher overall losses in productivity due to the greater availability of laser tracks. [48]

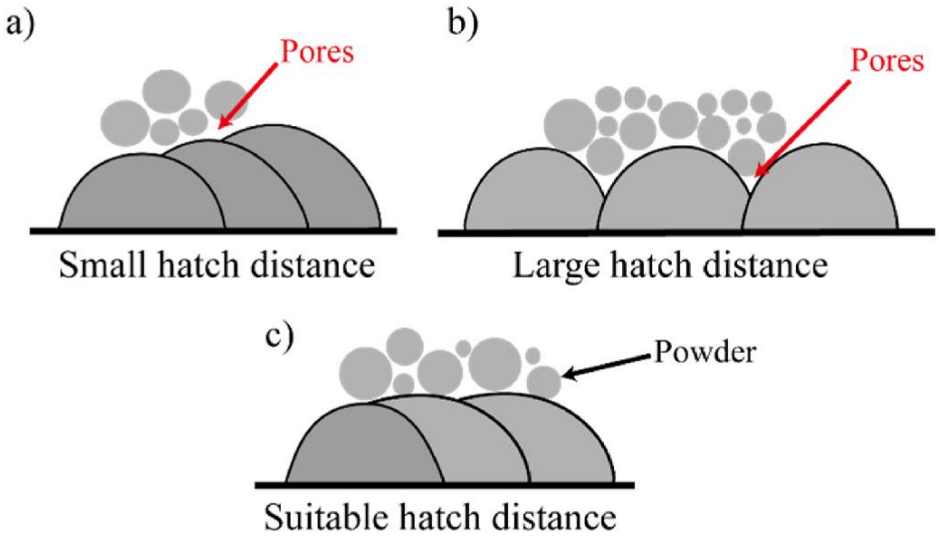

Figure 6: Hatch distance and overlap[49]

Indeed, the hatch distance should, when optimized, consider a fine balance between these factors. Studies show a typical approach with the spacing kept below the diameter of the laser beam to ensure quality.[50] The optimal hatch distance (h_{opt}) is calculated using Eq. 1:

$$h_{opt} = 0.25 \cdot d \tag{1}$$

where d is the laser spot size. The hatch distance is usually sized from 0.05 mm to 0.4 mm, depending on the material properties and process parameters. [31]

Recent studies have shed great light on understanding how hatch distance affects the behavior of materials and the outcomes of fabrication. Dong et al. looked at hatch spacing on 316L stainless steel and found that with the increase in hatch spacing, narrower melt pools were formed, deeper penetration was attained, and coarsening of microstructures occurred due to slower cooling rates. An optimal hatch distance of 100 μm was determined, resulting in the production of dense parts with smooth surfaces.[51] Saghaian studied NiTi alloys and concluded that the decrease of hatch distance improved shape memory effects and recoverable strain. The results of this study provided 120 μm as the optimal spacing for minimal surface roughness, allowing uses for the material in biomedical fields such as bone implants. [52]

Feng[53]investigated hatch distances regarding defects, phase transformations, and mechanical properties for NiTi; they documented an evolution of defect type as hatch distance increased, from predominant keyholes to gas pores to unfused areas. An optimal setting of 110 μm, they concluded, kept porosity low, favored almost spherical gas pores, and improved tensile properties, as well as shape recovery rates. Also analyzed were residual stresses and metallurgical alterations, mainly phase transformations and nickel evaporation, turning into a huge factor during the martensite transformation process. Notably, other involved residual stresses were mostly located along the B2-(100) plane, thereby hinting at a complex interaction between material science and process parameters.

Productivity is another prime consideration affected by hatch distance. Short hatch distances tend to require more laser passes and, therefore, will slow down the process and increase production cost. The chosen hatch spacing must be carefully balanced in terms of quality, mechanical performance, and efficiency to achieve the required compromise.

The results highlight that hatch distance stands as an influential parameter in the L-PBF process, determining not only part quality but also mechanical response, productivity, and cost efficiency.

2.4.4. Scanning Strategy

Laser power bed fusion (L-PBF) scanning strategies describe the specific physical path the laser travels over the build substrate.[54] This trajectory is one of the critical aspects of the process; it may vary within a single layer or contrast between consecutive layers, depending on the specific strategy being implemented.[55] The two dominant scanning modes are contour mode and hatch mode (or fill mode). The most common hatch patterns are indicated in Figure 7.

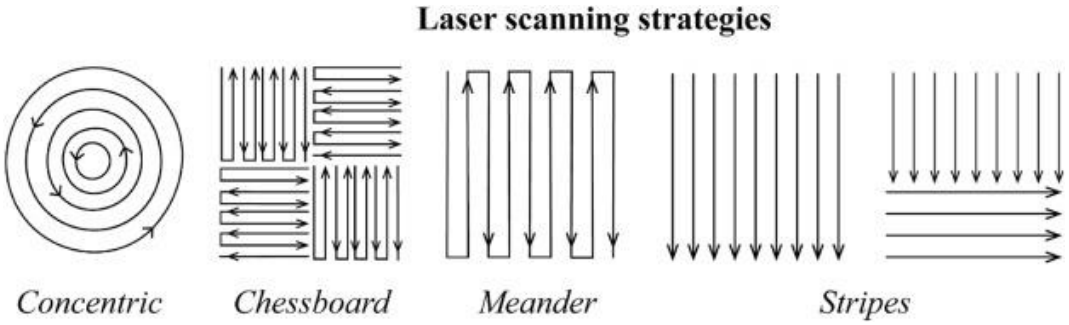

Figure 7: Examples of scanning strategies usied in L-PBF method [56]

Firstly, in contour mode, laser scanning happens along the outer edges of the layer, thereby outlining the boundaries of the part and guaranteeing higher accuracy and surface quality. In hatch mode, the laser now directs its attention toward the fill of the layer, thereby forming the bulk of the part. Typically, a hatching operation occurs after the contouring operation has been completed. In concert, these strategies integrate accuracy and efficiency.

Different hatch patterns have been studied and applied to promote mechanical and thermal properties of fabricated components. Straight lines scanned serially in parallel stripes with alternating rotational angle from layer to layer are the most common trajectories used to enhance isotropy. Other pattern types that are also widely used include concentric or meandering routes and chessboard configurations that work on one square at a time.[3] The selection of any one path deeply influences the quality of the processed parts, especially concerning residual stress generation leading to deformation and/or failure. Studies show that longer, uninterrupted scan lines tend to cause increased residual stress and resultant deflection of the part [57], while methods that disrupt this type of continuous path, such as breaking up the scan area into smaller-sized squares or alternating rotational angle between adjacent layers, help to reduce residual stresses.

Although a wide variety of scanning trajectories allow the possibility of making accurate parts with less residual stress, they increase the processing times. Consequently, an important requirement is the optimization of laser motion to minimize layer build times and to improve

productivity. However, one must be careful during this optimization since strategies that are most favorable in producing quality do not necessarily correspond to the quickest ways to produce.[58] Additionally, the component geometry influences the scanning strategy choice; for instance, for parts with sharp corners where precision is important, contour scanning is preferred, while hatch scans are adopted for parts with gentle slopes to yield smoother surface finishes and faster production rates. [59]

Various scanning strategies have been examined for their effects on microstructure, density, and mechanical properties. For example, it has been reported for 316L stainless steel that reversing the scanning direction between layers disturbed the directed columnar grain growth, yielding refined equiaxed grains with improved tensile strength and ductility properties.[60] Similar optimization of scanning strategies and laser energy density was performed on 24CrNiMo low alloy, maintaining the specimen density and surface quality while obtaining desired prints with a bainite microstructure for strength.[61] The island scanning strategy applied on 15-5 PH stainless steel generated fully dense samples with finer-grained structures and improved strength and elongation without the need for any extra precipitation hardening treatment.[62]

2.4.5. Layer Thickness (*l*)

Layer thickness is the height of an individual slice made from the CAD model and is directly affected by the downward movement of the machine's build platform. This parameter is central to L-PBF processes as it directly affects the quality, mechanical properties, and productivity of the fabricated part. Normal values of layer thickness are about 20 μm to 80 μm; although values outside this range have been recorded in applications pertaining to specific materials. [38]

Thin layer thickness is favorable for the manufacture of high-resolution parts since it improves dimensional accuracy and reduces surface roughness, thereby providing smoother finishes. [59]Increasing the thickness, however, comes with complications. Once the thickness reaches a certain limit, it is possible that the energy supplied by the laser would have become inadequate to ensure proper fusion and cohesion among the subsequent layers. This lack can result in defects like porosity and inadequate bonding strength, thereby reducing the density and mechanical properties of the made part.[63]

Despite these challenges, larger layer thicknesses offer significant advantages in terms of productivity. L-PBF, being a layered manufacturing process, benefits from fewer layers and shorter build times when the layer thickness is increased. Because the layer numbers are reduced,

the approach is called for increased production and decreased overall costs, assuming identical other parameters. However, the acceleration of production must be balanced against any possible diminishment of mechanical property performance due to increased layer thickness. Hence achieving an optimal compromise between productivity and the performance of mechanical parameters will be a serious consideration for L-PBF optimization.[47]

The influence of layer thickness on the quality and performance of components produced has been studied in various works made on this topic. In the study conducted by Shi et al.,[64] the layer thickness on Ti-6Al-4V was analyzed on the effect of surface roughness, which was shown to deteriorate significantly with an increase in layer thickness, while up to 100 μm relative density and tensile properties remained unchanged. But with an increase in thickness to 200 μm, the effect of defects and microstructural changes compromised tensile strength significantly. Cutolo et al. [65]also showed with CoCr scaffolds that productivity increased enormously when increasing layer thickness from 30 μm to 60 μm with no disadvantage to geometry of the final structure. They performed fatigue tests in which no noticeable differences were observed in performance with respect to change in thickness.

Leicht et al. [38]studied the effect of increasing layer thickness on stainless steel 316L parts with results showing an increase in fabrication speed by four times as they changed the thickness from 20 to 80 μm. Though the thicker layer caused fusion defects and lowered fracture elongation, the tensile strength was still well within the specification limits for cold-rolled stainless steel 316L. Thus, larger layer thicknesses could compromise some mechanical properties; nonetheless, these will still be acceptable under industrial quality standards when proper conditions are maintained.

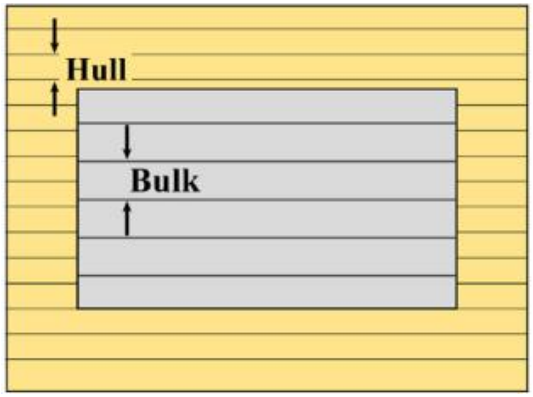

Figure 8: Hull-Bulk strategy

A widely recognized solution to address the accuracy-productivity trade-off is that hull-core method developed by de Formanoir et al.[66] As shown in Figure 8, In this technique, different parameter settings were applied to different regions of the part: settings that would ensure maximum accuracy were applied to the external skin to achieve excellent surface finish and

resolution, while settings that would deliver high productivity were applied to the internal core to maximize their speed of fabrication. This enables a score of the component that satisfy the needs for both quality and efficiency.

The foregoing results all support the finding that layer thickness is a prime parameter in L-PBF. Larger layer thicknesses favor productivity; however, they can also become detrimental to surface quality and mechanical properties if poorly managed. Whereas thinner layers maintain high resolution and high surface finish, they suffer from longer build times and higher production costs. Hence, understanding these trade-offs and changing layer thicknesses for various applications are very important to optimize the L-PBF process and thereby strike a balance between quality and efficiency.

2.4.6. Combined Process Parameters

Since the process parameters of L-PBF which are shown in Figure 9 are strongly interdependent and mutually interactive, they influence one another. [3]These parameters, laser power (P), scan speed (v_s), hatch distance (h), and layer thickness (l), together define the energy density given to the melt pool, of which the quality and efficiency are dependent. [67]Therefore, one needs to optimize the parameters with caution; changing one will disrupt this balance, thus affecting the results negatively.

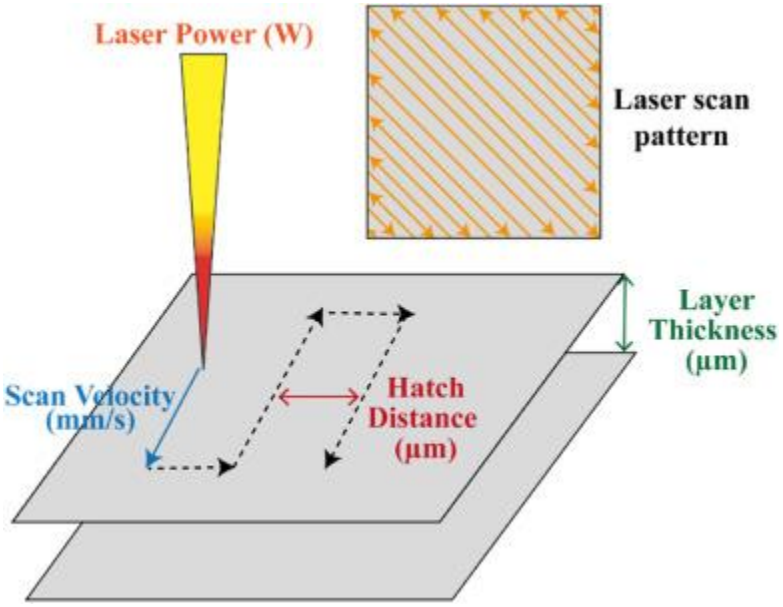

Figure 9: Dominant process parameters in the L-PBF process

To characterize the energy input for L-PBF and develop its optimization, certain quantitative measures have been defined. Of these, Linear Energy Density (LED) happens to be one of the simplest and the most widely used. Defined by following equation (Eq. 2):

$$LED = \frac{P}{v_s} \quad \left[\frac{j}{mm}\right] \tag{2}$$

where P and v_s are laser power and scanning speed, respectively. This metric captures the energy imparted to the material per unit length of the scan path, thereby determining the dwell time of the laser on the melt surface. Change in LED helps researchers and engineers get different geometric accuracies and surface roughness.[56] Process window diagrams are often used to map combinations of parameters to achieve components with maximum density and minimum porosity. [3]

Area Energy Density (AED) gives a more qualitative measure of energy distribution over the cross-sectional area of the part. This is defined as (Eq. 3):

$$AED = \frac{P}{h \,.\, v_s} \quad \left[\frac{j}{mm^2}\right] \tag{3}$$

It should be noted that this indicates the energy received by the cross-section of the material in laser fusion. AED is an important means of parameterizing input factors with their processing conditions, especially in studies of single-layer fabrications. Recognizing AED gives researchers the ability to analyze and overcome some specific problems, including inter-track pore formation being one of the common defects in L-PBF processes. [68]

The most detailed descriptor, Volumetric Energy Density (VED), expands this concept to include the volume of material affected by the laser. It is given by Eq. 4

$$VED = \frac{P}{l \,.\, h \,.\, v_s} \quad \left[\frac{j}{mm^3}\right] \tag{4}$$

Most widely adopted is VED as an essential parameter linking process settings with mechanical, geometric, and density characteristics of the final part. The VED parameter describes the energy absorbed by the unit volume of the material and is a parameter indication for selecting the optimal parameter window.[56] This is especially effective when there are many objectives such as high densification, good mechanical properties, and production rates. [69]

Working with optimal energy densities can assuring good-quality parts while preventing defects like porosity or under-fusion or over-melting. VED values are reported in the range of 30-210

J/mm³, depending on variations arising from materials' chemical composition and specific requirements of the process. Even parts with the same VED may have quite different properties, as energy interacts differently with varied materials, thus proving how complicated the process can be and necessitating more studies into the interaction of parameters.[70]

Besides these conventional metrics, modernity also dictates that advanced experimental methods such as high-speed beam oscillation provide additional means to achieve enhanced energy distribution. By adjusting the spatial and temporal characteristics of the melt pool, one could influence the subsequent microstructure and increase productivity. This method was first proposed by Wu et al. for applications in which L-PBF processes could be tweaked once more to affect better part quality and efficiency.

In general, combined process parameters in L-PBF represent a delicate balance of interdependent effects. Optimization of these process parameters is mandatory for achieving the desired result since any parameter set incorrectly can result in defects, low efficiency, or detraction of part properties.

2.5. Productivity

Like other conventional manufacturing technologies, L-PBF still has a well-recognized limitation in productivity, whereby the production rate often challenges it. While L-PBF can manufacture complex geometrical shapes with very high precision, efficiency is usually constrained by the extended processing time required for these intricate designs. Research efforts have been directed toward improving the efficiency of the method, but these usually come at the cost of increased precision or technological optimization and result in higher production time. This trade-off greatly affects L-PBF's viability for large-scale manufacturing applications.[71]

The most well-known consequence, due to low production rate, is the elevated cost per part, which may be an important obstacle to large diffusion in metal additive manufacturing industry fields. Apart from the expensive machinery costs, the costs included are raw materials, energy and gas consumption, and building times.[33] In such a process-specifically slow, L-PBF manufacturing can, most of the times, only have very limited contributions to high volume production.

In order to better understand and quantify the productivity of L-PBF, several cost models have been developed by researchers for evaluation of the process's efficiency. Among these, a structured cost model inclusive of AM-specific parameters-part orientation and support structures-was developed by Alexander et al. [72]A cost model on SLS was addressed by Hopkinson and Dickson,[73] which focused on the issue of consistent processing times for identical components. This approach was further refined by Ruffo et al.[74] by including direct and indirect costs to provide an in-depth economic analysis. Precisely, Rickenbacher et al.[75] developed a cost model specifically for L-PBF, encompassing all process characteristics, including pre- and post-

processing operations, which turns out to be more adaptable to the estimation of the costs involved with AM.

It can be quantified by the L-PBF productivity, understood as the volume of the produced part Vp with respect to the overall processing time Tp [19], given by Eq. 5:

$$PR = \frac{Vp}{Tp}\left[\frac{cm3}{h}\right] \tag{5}$$

Productivity can be improved by either manufacturing more material at the same time or achieving the same output in less processing time. However, as discussed earlier, the productivity indices for L-PBF processes are generally low, and that is the reason why L-PBF applications in high-volume production are not feasible. The trade-off between the production speed and quality of the part, has remained one of the most important challenges during the optimization of L-PBF.

2.5.1. Processing Time

Processing time is a critical factor in determining the efficiency and feasibility of Laser Powder Bed Fusion (L-PBF) as a manufacturing technology. It directly influences the productivity, cost-effectiveness, and scalability of the process. The total processing time is composed of three distinct phases: pre-processing (T_{pre}), build time (T_{bld}), and post-processing (T_{post}).[69] These three components together define the total time to manufacture a part and, therefore, have been the key contributors to the optimization of L-PBF for industrial applications. The total processing time is defined by Eq. 6:

$$T_P = T_{pre} + T_{bld} + T_{post} \tag{6}$$

The pre-processing stage involves all the preliminary steps before actual printing. It includes machine setup, laser calibration, and powder bed leveling, along with loading the STL file carrying the 3D model in it. The precision of this step is highly essential since any misconfiguration can result in defective parts, higher material waste, and failed builds, which means longer production periods and growing costs.

T is the actual build time and forms the crux of the process, when the laser selectively fuses the metal powder, layer by layer, according to the CAD model. Several factors have their influences on this phase, including laser power, scanning speed, hatch spacing, layer thickness, and part complexity. The relationship between these variables must be carefully optimized in order to achieve a balance between speed and part quality.

For instance, increasing the thickness of layers can reduce build time by minimizing the number of layers required to complete the part. However, using thicker layers can compromise surface finish and mechanical properties, making a trade-off between speed and quality. Higher scanning speeds increase throughput but may result in porosity, incomplete melting, or poor inter-layer bonding if not properly calibrated with laser power.

The post-processing encompasses several steps that are required to realize the final specification of the part. The additional processes include removal of the support structure, heat treatment, machining, polishing, surface finishing, improvement of mechanical properties, and dimensional accuracy. In industries needing high levels of precision at higher values, such as in the manufacture of aerospace, medical, or automotive parts, post-processing may need much more time and add to the general production cycle.

Several optimization strategies have been tried by researchers to reduce the total processing time and improve productivity. Among them, the main approaches are the fine-tuning of process parameters-laser power, scanning speed, and hatch spacing-to maximum efficiency without loss of part quality. Besides process optimization, machine design has also been improved, with multi-laser systems and optimized recoating mechanisms showing great potential for increasing throughput.[74], [76]

Other developments include high-speed beam oscillation, which performs uniform energy distribution on the melt pool for the faster melting and solidification of powder layers. Parallel processing, where several lasers working simultaneously, each on different parts of the build plate, also showed significant build time reductions, and therefore have made L-PBF quite competitive with other traditional manufacturing processes.[77]

While these improvements have been achieved, increasing this rate without compromising the quality is still a challenge. Further efficiency and precision are being advanced in ways that include the use of AI and ML, since these technologies can be integrated into real-time process monitoring and adjustment of the parameters in the process.

Processing time provides the main barrier to the industrial adoption of L-PBF technology. Continuous refinement of process optimization techniques, investigations into new machine architectures, and integration with intelligent automation continue to increase the potential for L-PBF as a viable and scalable solution toward high-volume production.

2.5.2. Build time model

The build time is one of the most important factors in Laser Powder Bed Fusion, which influences the overall efficiency and productivity of the process. It is a measure of the total time needed by the laser to selectively fuse the metal powder, layer by layer, until the entire part is completed.

Since L-PBF operates in a successive, layer-based approach, build time depends on several variables that are interrelated: scanning speed, recoating time, and total number of layers.[3]

The total build time can be represented mathematically as follows (Eq. 7):

$$T_{bld} = T_d + T_r + T_s \tag{7}$$

Where T_d is the delay time, which considers the time taken by the machine's build platform to move down to position after depositing each layer. This must be appropriately aligned to provide a constant thickness of the layers to avoid structural anomalies. T_r recoating time, the time a recoater needs to spread a new layer of powder evenly on the build platform. Since this step should be done appropriately, it might have a big consequence on general build rate. An uneven layer of powder might lead to the defects and hence re-machining. T_s represents material scanning time; that is, the time that should elapse to enable the laser to scan and selectively fuse each layer as a result of the CAD.

All these factors greatly affect the total build time. When the recoating process is either slow or inconsistent, the laser must wait before it can continue with the next layer, and thus that increases the overall cycle time. If the scanning speed is too fast for the power of the laser, incomplete melting may occur, leading to porosity and weak inter-layer bonding. On the other hand, overly slow scanning unnecessarily prolongs the time taken to build a component, which in effect reduces efficiency in the process.

These parameters need to be balanced in a very judicious manner to optimize build time. Increasing the thickness of layers decreases the total number of layers that need to be built to complete the part, thus reducing the overall build time. However, this needs to be controlled so as not to introduce defects such as reduced surface quality and incomplete fusion. Hatch spacing is another parameter affecting build time; it refers to the distance between adjacent laser passes. The wider the hatch spacing, the fewer the number of passes needed per layer, hence faster; it must be kept in an optimal range to allow proper bonding between the tracks.

Efficiency in the recoating mechanism is another important influencing factor on the build time. High-performance recoating systems, such as multi-roller recoater, enhance powder distribution speed and uniformity, reducing waiting time before the laser starts scanning the next layer. Besides, multi-laser systems increase efficiency in scanning by processing more than one region of the build platform at the same time, hence reducing the total time it takes to make the part.

In turn, these parameters must be cautiously adjusted to achieve an optimal balance between the build time and the quality of parts in L-PBF. Maintaining a balance between scanning speed, hatch spacing, recoating efficiency, and laser power becomes crucial in enhancing productivity with no compromise in structural integrity at the final component level.

2.5.3. Build rate

The build rate is one of the major factors in the L-PBF process, defining the amount of material melted in one unit of time. The overall cycle time in L-PBF consists of two main components, namely main process time and auxiliary process time[32]. The time of the main process includes just the time taken by the laser to melt the layers, in other words, the scanning time; auxiliary time is another operation that may be required to complete the fabrication process. Since the build rate is a factor directly affecting productivity, this parameter needs to be optimized for improving manufacturing efficiency and reducing the cost per part.

Mathematically, that is (Eq. 8):

$$BR = v_s \cdot h \cdot l \left[\frac{mm^3}{s}\right] \tag{8}$$

where v_s represents the scanning speed, h denotes the hatch distance, and l corresponds to the layer thickness. All three parameters together define the speed at which the material is processed in printing. Increasing the build rate is one of the effective ways to enhance manufacturing throughput; however, it must be watched so as not to have adverse effects on the quality of the final component.

The most direct ways to increase build rate are the use of thicker powder layers, higher scanning speeds, and wider hatch distances. A thicker layer reduces the number of layers needed to complete a part, while a higher scanning speed enables faster movement of the laser across the powder bed. The use of larger hatch spacing minimizes the number of laser passes that must be executed per layer. However, these modifications can greatly minimize the build time but may cause some potential drawbacks. For instance, the higher layer thickness causes a lower quality surface with greater roughness. Similarly, higher scanning speeds or hatch distances result in inadequate melting, poor fusion between tracks, and geometrical inaccuracies that may influence the mechanical integrity of the component.

A trade-off must be made in order to balance productivity and part quality optimally. For that, simply increasing the build rate will not be able to sustain tight control over energy input and, consequently, fusion behavior, and defects like porosity, lack of fusion, and dimensional inaccuracies will appear. Consequently, manufacturers apply various optimization techniques in order to improve build rates without sacrificing part accuracy and mechanical performance.

One of the possible ways of advancing build efficiency without sacrificing the quality of building could be achieved by using machinery with an extended volume of build. Such systems can hold more parts in one build, thus allowing higher capacities of production per build cycle. Besides, in

most modern concepts, integration of multi-laser systems, like twin or even quad laser systems, allows the simultaneous scanning in different areas of the build platform, considerably improving the throughput. By optimizing scanning strategies, laser configurations, and machine architecture, L-PBF technology continues to evolve as a more cost-effective and scalable manufacturing solution.

2.5.4. Cost model

The cost model of L-PBF is a significant mode of analysis in the light of economic viability regarding additive manufacturing. Most of the usage of L-PBF has been for small batches of highly complex parts due to long build times. The technology creates lightweight, complex functional parts with a minimal amount of waste, which is particularly useful for aerospace and medical applications since the designs of components are their customization. However, for less complex productions with high throughput, traditional manufacturing processes are favored since they offer cheaper methods with higher throughputs.[78]

The cost of manufacturing a product by AM may be partitioned into the direct cost and indirect cost as described by Eq. 9:

$$C_{job} = C_{direct} + C_{indirect} \tag{9}$$

where the direct costs are largely driven by the amount of material used in printing, and indirect costs are proportional to the operating time of the machine, energy consumption and overheads included.[79]

The most basic form of cost model will consider only the material cost as the direct cost, whereas other costs like amortization, electricity, and gas consumption attribute to the indirect costs. The total cost equation is given by Eq. 10:

$$C_{job} = C_{material} + C_{operating} = m_{material} \cdot P_{powder} + \dot{C}_{operating} \cdot T_{bld} \tag{10}$$

Where $C_{material}$ accounts for the cost of the metal powder used during the build process, calculated based on the volume of the part (V_{part}), its material density ($\rho_{material}$), and the price per kilogram of powder (P_{powder}) as expressed in Eq. 11[3]. In order to refine this cost estimate, two factors

(K_s and K_r), will be introduced that consider the consumption of support material (1-1.5) and recyclability of powder (1-7), respectively.

This gives us the refined formula for the cost of material as follows:

$$C_{material} = K_s \cdot K_r \cdot V_{part} \cdot \rho_{material} \cdot P_{powder} \tag{11}$$

Besides material costs, the operating cost of the machines is a major contributor to the overall cost. The operating cost of an AM machine per hour includes several factors such as equipment amortization, electricity, and gas. The equation for the hourly operating cost is (Eq. 12):

$$\dot{C}_{operating} = \frac{P}{hy \cdot ay} + P_{el} \cdot C_{el} + P_{gas} \cdot C_{gas} \tag{12}$$

where:

- P represents the machine's purchase price (€),
- hy denotes annual production hours (h/y),
- ay corresponds to amortization time ($years$),
- P_{el} and P_{gas} indicate the electricity and gas prices respectively,
- C_{el} and C_{gas} denote electricity and gas consumption rates.

The machine operation rate per hour is calculated considering the equipment operates 5000 hours per year for an amortization period of five years.[80] The values of electricity and gas consumption are usually taken from technical datasheets, estimating the cost of electricity at $0.16\ €/kWh$ and the price of gas at $3\ €/m^3$ when argon is used as the chamber gas.

One of the major cost drivers of machine working time is due to build time, T_{bld}. Working time includes total part volume, build rate, and recoating time per layer, given by the Eq. 13 and 14:

$$T_{bld}(s) = \frac{V_{part}[mm^3]}{BR\left[\frac{mm^3}{s}\right]} + \frac{Part\ height(mm)}{Layer\ thickness(mm)} \cdot T_{rc}(s) \tag{13}$$

or expressed in hours:

$$T_{bld}(h) = \frac{\frac{V_{part}[mm^3]}{BR\left[\frac{mm^3}{s}\right]} + \frac{Part\ height(mm)}{Layer\ thickness(mm)} \cdot T_{rc}(s)}{3600} \tag{14}$$

where T_{rc} is the recoating time per layer; for example, 12 seconds per cycle for the Prima Print sharp 250. This model simplifies costing but does not take into consideration costs related to material preparation, machine setup, and post-processing, among others, which might be vital in the estimation of total costs. In fact, studies say post-processing and auxiliary operations can be as high as 19% of the overall cost of production.[81]

Another key factor driving the cost is energy consumption, which is generally considered a direct cost in determining the lifecycle impact of AM-manufactured parts. Energy consumption during fabrication is usually measured in megajoules per kilogram (MJ/kg), which is commonly referred to as specific energy consumption (SEC). The SEC for L-PBF processes ranges from 80 to 600 MJ/kg, depending on the material, process efficiency, and machine configuration.[82] Previous works from several authors have calculated an average of 96.82 MJ/kg for SEC related to the use of L-PBF systems.

Cost optimization in L-PBF manufacturing requires a balance of material consumption, machine efficiency, and energy usage. Though L-PBF enjoys certain advantages in the manufacture of customized components with high precision, there is still a need for refinement of cost models, improvement in machine performance, and development of advanced process strategies if the technology is to be more viable economically for large-scale production.

2.6. Quality

Surface roughness, microstructure, porosity, and mechanical properties are some of the main factors that generally identify the quality of a final part in L-PBF processes.[83] All these factors have a tradeoff that needs to be balanced; each influences the general performance and reliability, yet each represents a specific characteristic. Nevertheless, the optimal settings for all these usual conflict with one another in some ways.[84]

In this context, optimized process parameters can only be identified for satisfying some goals that involve producing completely dense parts, reduced defects, improved surface finish, superior mechanical properties, and a high build rate.[27] To obtain all or some of the properties, all such objectives must be optimized. For controlling the quality of the final part, different critical factors, which involve laser power, scan speed, layer thickness, and hatch distance, may become influential.

The following process parameters were previously investigated for stainless steels, aluminum, Inconel, and titanium alloys in order to understand how they might influence the properties of the final product. This way, its influence can be used to better control the manufacturing process and to improve the quality of the parts.

Admittedly, surface finish, internal structure, and mechanical strength checks will, finally, must be made in the quality checking of the as-built parts. The challenge, however, has been how the sometimes-conflicting requirements for high-value components can be brought into balance with needs for efficient production. Figure 10 demonstrate how different quality parameters are considered.

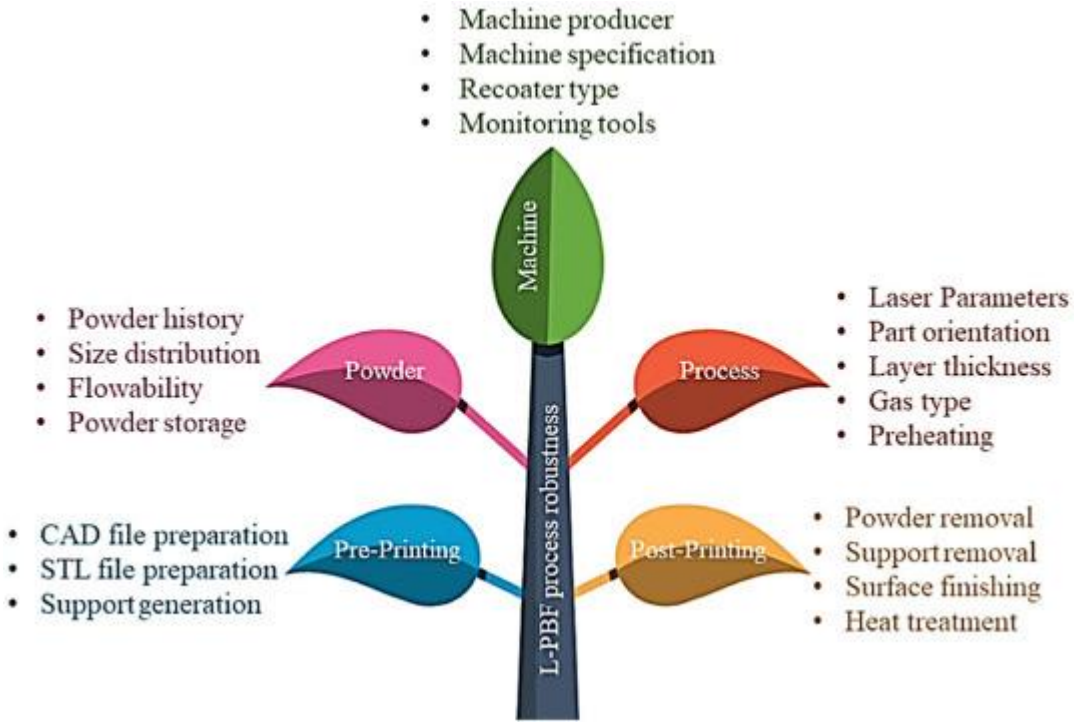

Figure 10: Product Quality parameters

2.6.1. Surface roughness

Surface roughness is major quality parameter controlled by many process parameters in the L-PBF process, including laser power, hatch spacing, layer thickness, and scan speed. Among them, hatch spacing optimization is very significant in improving surface finish of the parts manufactured from AISI 316L and Inconel alloys.[85] An optimal decrease in hatch spacing helps reduce surface roughness; however, an extreme decrease in hatch spacing would lead to various disadvantages.

Laser power has a tremendous effect on surface roughness and dimensional accuracy. When the power is insufficient for complete melting of the powder layer, particularly when thick layers are generated, this impedes surface finish by allowing powder particles to stay bound within the metal-liquid matrix. Increasing laser power reduces surface roughness and improves geometrical

precision. Conversely, an increased laser power deteriorates improvement at a high rate due to high scanning speed.[85]

Scan speed also affects surface quality. Too-high scanning speeds halt the complete melting of the powder bed surface, which degrades roughness. While Badrossamay et al. found scan speed and roughness did not show a clear correlation, they mention that an increase in scan speed greatly improves the surface finish of AISI 316L samples. In a like manner, Guo et al. stated that the surface quality of Inconel specimens was poor with both very high and very low scan speeds.[85]

Thickness of the layer affects roughness as well; melt pools enlarging with an increase in the thickness of layers, resulting in rougher surfaces. Numerous investigations substantiated the improvement of surface smoothness through layer thickness reduction.[86]

Ultimately, optimization of process parameters is required to achieve the target surface roughness for products fabricated by L-PBF. Maintaining a trade-off between laser power, hatch spacing, scan speed, and layer thickness becomes very crucial to obtain a high surface finish without affecting productivity.

2.6.2. Microstructure

The microstructure of components in the L-PBF process, is complex in nature and incorporates a large quantity of elongated grains across numerous melt pool boundaries.[33], [87] This makes it very intricate and develops in such a fashion due to steep heating and cooling cycles in processing that influence growth, phase development, and altogether material properties. With its great sensitivity to processing parameters, microstructure optimization will be key in the future in minimizing defects like pores and cracks, apart from enhancing fineness in grain structure. This is important because a refined microstructure ensures that the mechanical properties of strength, toughness, and resistance to failure in the final component are superior.[88], [89]

Various researchers have studied the microstructural characteristics of parts made by L-PBF and identified crucial defects that can create a potential pathway for material degradation. The issues include microsegregation, coarse columnar grains, undesirable textures, and meta-stable phases such as martensite. Oliveira et al. [27]reported that microsegregation caused by an inhomogeneous distribution of alloying elements during solidification can be eliminated either by greatly increasing or strongly lowering the laser velocity. This adjustment encourages homogeneity in the distribution of elements, hence improving material consistency.

Besides microsegregation, the mechanical properties are further deteriorated by coarse columnar grains and unwanted texture. These features result from the directional solidification patterns

developing in the process of L-PBF. For instance, according to the work of Oliveira et al., a lower laser speed or reduced laser power may be decisive in breaking columnar grain structures up into more equiaxed and refined microstructure. Such modification enables better isotropic properties, making the material more uniform in all directions, and reduces the susceptibility of anisotropic mechanical behavior.

Other challenges in L-PBF microstructures are metastable phases like martensite, which could be formed because of high cooling rates. Though martensitic phases may provide an increase in hardness, the material becomes brittle and prone to cracking. This issue can be overcome by Oliveira et al. and other researchers who recommend that the remelting should take place under reduced laser power and that controlled reheating with gradual transformation into more stable phases occurs. These treatments improve the ductility and toughness of materials without sacrificing adequate strength.

These microstructural defects are linked to mechanical properties and performance of components produced by L-PBF. If not well controlled, they can lead to reduced fatigue resistance, increased brittleness, and possible failure under mechanical loads. Therefore, as emphasized by Oliveira et al. and other researchers, laser power, scan speed, hatch spacing, and remelting strategies need to be in tune in order to achieve a refined and homogeneous microstructure. These parameters are being carefully adjusted by manufacturers to improve strength, durability, and reliability in general for parts produced through L-PBF, meeting the demands of aerospace, biomedical, and industrial high-performance applications.

2.6.3. Porosity

Porosity is the most frequently documented flaw in AM manufacturing of metals that considerably affects its mechanical properties. Porosity mainly occurs in L-PBF due to the manufacturing process; it can be of two distinctive types, which are lack of fusion porosity and keyhole porosity. These are the defects obtained from the variations of process parameters that may reduce the material density, thus compromising the strength and toughness of the ultimate part.[90]

A lack of fusion porosity seems to be due to the shortage of input energy in which the melting of the powder is not fully complete. Lack of fusion porosity is controlled by various parameters such as scan strategy, laser power, scan velocity, hatch distance, and layer thickness.[27] non-spherical thin, crescent-shaped pores characterize porosity for lack of fusion porosity due to incomplete bonding among successive layers.[91] According to Eliasu [92], studies have indicated the possibility of improving this factor through energy input optimization to ensure proper melting and better fusion between layers.

Keyhole porosity forms as a result of unstable dynamics in the melt pool, where the gas gets trapped within the solidified material. This primarily happens due to excessive laser power, which

causes metal vaporization and increases recoil pressure, thus creating gas bubbles that get trapped within the material. Unlike a lack of fusion porosity, keyhole porosity consists of round voids that are more dependent on laser power and scan velocity and less dependent on variations in layer thickness and hatch distance. Changes in scan strategy can help to manage keyhole porosity, and an increase in laser power or a decrease in scan speed is generally recommended to avoid its occurrence.

Another variable that influences porosity is the VED. It has been observed that, with increased VED, porosity in a manufactured part also increases. A low value for VED tends to increase the porosity owing to partial melting, which retains unfused powder within the layer. In turn, with higher VED values, improved melting and flowability of the melt reduce the tendency for pores. However, porosity increases again when energy density is too high because of the keyhole effect due to excessive vaporization that leads to gas entrapment. It was clearly indicated by the work of Eliasu on the AISI 316L microstructure that there was a good correspondence between porosity and VED, and trends have also been found for other metallic alloys.[92]

Controlling porosity in L-PBF parts therefore requires optimization of process parameters. Reducing laser power, scan speed, and energy density could minimize most porosity defects, thus improving material density, mechanical properties, and performance. Tuning such parameters allows a manufacturer to minimize defects in order to make quality components with improved structural integrity.

2.6.4. Densification Behavior

It is important to put into consideration the cruciality of high-density structure for the manufacture of good quality L-PBF components because with the right processing parameters, densities above 99% are achievable.[93] It is the selection and adjustment of these parameters which is an important factor in low porosity and mechanical integrity of the final part; however, some process variables have a negative impact on densification, hence the need to balance all the process variables.[31]

It is found from research that increasing hatch distance and vector scan size yields a decrease in part density, as both these parameters affect the effect of overlapping of laser tracks and the uniformity through such melting with which both parameters induce melting. The increase of laser power, on the other hand, contributes positively to densification, as it makes the melt pool depth and width with each layer fusion treatment. However, either extremely high or low scan speeds would negatively influence density, especially at high hatch spacing. Very high scan speed feeds quite insufficient energy to powder resulting in lower melting and high porosity, whereas very low

makes overheating, excessive evaporation of material, and keyhole porosity that also can compromise density.

Control of densification largely depends on Volumetric Energy Density (VED), which reflects the energy applied per unit volume of material. Studies indicate that there exists a steady region within which a certain range of VED produces full densification. Throughout that range of VED, different combinations of process parameters would be adjusted to ensure achievement of high-density levels while still satisfying the desired mechanical properties (Figure 11). This steady region includes a variety of selections of process conditions which suit different materials and applications, ensuring structural integrity as well as production efficiency.

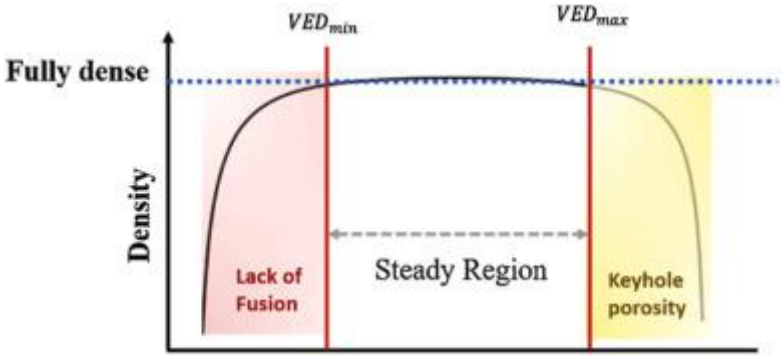

Figure 11: Density as a function of VED

The continent route is also covered as far as optimization of laser power, scan speed, hatch spacing, and vector scan length is concerned within the above steady state by manufacturers to best control the densification behavior thus decreasing defects and increasing reliability of L-PBF manufactured components. While research is continually advanced to provide more refined process maps and experimental databases, understanding of optimized parameter settings will be continuously improved, thus bringing further advances in the quality and performance of additive manufacturing.

2.6.5. Mechanical Properties

The mechanical properties of L-PBF-manufactured components have pointed out the possibility of the process to produce high-strength alloys, usually superior to conventionally manufactured parts. Indeed, the better mechanical behavior has been mainly attributed to the fine microstructure and supersaturated solid solution, thanks to the inherent rapid solidification effect of the L-PBF process. These rates of cooling lead to the limitations in grain growth and result in a refined structure, cellular microstructure, nano-sized precipitates, and overall enhancement in terms of strength, hardness, and wear resistance. This makes the technique of L-PBF ideal for high performance in aerospace and industrial applications besides biomedical applications for those sectors whose products require intact mechanical integrity.[94]

The porosity level directly acts on the density of the fabricated parts, which is one of the most critical parameters affecting the mechanical properties. Different studies have indeed proven that a significant increase in mechanical performance takes place when porosity decreases below 1%, as it suppresses the formation of voids that act as crack initiators under stress.[95] Guo et al. reported that excessive high or low scan speeds caused an increase in porosity for samples built from IN738LC, which was associated with decreased mechanical strength. [85]Therefore, mechanical performance is only achieved by keeping the process parameters under tight control to maintain the high density without defects.

Several significant mechanical properties like tensile strength, Young's modulus, elongation at break, tensile yield strength, and ultimate tensile strength were significantly affected by layer thickness.[28] As the thickness increases, these characteristics deteriorate with the presence of coarser grains and larger-sized melt pools that could decrease the overall material strength. Further hardness value and improvement in the mechanical properties are gained through finer grains, cellular microstructure, and uniformly distributed nano-precipitates.[96] However, Shi et al. showed that layer thickness indeed affects surface roughness but has little effect on tensile strength in the case of the L-PBF process, which also points out that probably laser power and scan speed have greater effects on mechanical properties in this process.[97]

Laser power also plays a crucial role in determining mechanical behavior. Studies have shown that an increase in laser power improves both microhardness and tensile properties by promoting better fusion between powder particles, thereby reducing porosity and enhancing part density.[63] However, excessive laser power can introduce keyhole porosity, leading to localized weaknesses. Thus, finding the optimal balance between laser power, scan speed, and hatch spacing is essential for achieving maximum strength and minimizing structural defects.

The temperature history of the part being printed will also be seen to affect mechanical performance by influencing residual stresses and phase transformations. Rapid cooling rates in L-PBF lead to the formation of metastable phases that alter hardness and toughness. Often, post-processing involves heat treatment or HIP further to refine microstructure and relieve residual stresses with enhanced mechanical properties.

Ultimately, the mechanical performance of L-PBF-manufactured parts is determined by a combination of microstructural refinement, density optimization, and precise process control. The proper adjustment of parameters, such as layer thickness, scanning speed, and laser power, enables the manufacture of high-strength materials with exceptional mechanical reliability. Further improvement in additive manufacturing research will lead to improved scanning strategies, in-situ monitoring systems, and enhanced post-processing techniques, further optimizing the mechanical performance that extends the use of L-PBF into very demanding industries.[98], [99]

2.7. Process Optimization Methods

L-PBF process optimization is very important in enhancing the aspects of productivity and quality of the product. This involves the selection of optimal parameters that balance speed, efficiency, and the integrity of the final part.[100] Several methods can be applied to achieve this, including experimental and computationally intensive models. Traditional methods, such as Design of Experiments (DOE) and Response Surface Methodology (RSM), systematically study interactions of parameters and predict optimum conditions. Mapping the process helps visualize parameter space for the best setting of quality and efficiency. On the other hand, state-of-the-art methods, such as Artificial Intelligence (AI) and Machine Learning (ML), applying historical production data, provide predictions about optimal combinations of parameters. In such a way, manufacturers can considerably enhance L-PBF process efficiency, which guarantees high-quality production with high productivity, having minimal defects. The following sections discuss specific optimization methods in greater detail.

2.7.1. Layer Thickness Optimization

The use of a greater powder layer thickness is probably among the simplest and most effectual means of improving L-PBF productivity. Thicker layers reduce build time owing to fewer recoating cycles and increased deposition rate. According to studies, increasing layer thickness within an optimal range can result in a 20–25% increase in productivity. Besides, fewer recoater passes mean less wear on the recoater mechanism and lower overall production costs. However, despite all advantages, increasing layer thickness beyond the limit causes problems. One of the key issues is incomplete fusion because thicker layers require more energy for complete melting. If the energy input is insufficient, porosity and lack of fusion defects may appear, which in turn reduce material density.

Moreover, thicker layers can lead to higher surface roughness, for which additional post-processing might be required. Defects related to incomplete fusion introduce stress concentration points, which can significantly affect mechanical performance, particularly under dynamic loading conditions.[38]

2.7.2. Volumetric Energy Density (VED) Method

Basically, VED method has been generally adopted when an attempt is made in the L-PBF process optimization of the process parameters that ensure adequate energy input availability towards

complete melting at higher build speed.[32], [33] VED has been defined as the ratio between laser power to build rate, with the latter varying based on scan speed and hatch spacing or layer thickness. Manufacturers can optimize maximum build speed by using the minimum VED that guarantees full material fusion. Such a method boasts several advantages; it increases the production speed with the identification of the fastest laser power, scan speed, and hatch spacing.[3] It also guards against overheating since excessive input of energy into the material is not allowed to cause distortions or unnecessary evaporation. It also does away with wastage of material by infusing only that quantum of energy necessary to achieve desired mechanical properties. In proof of this, experimentally, Eliasu et al. [92]investigated the VED-porosity/density relationship in AISI 316L samples. Results of their investigation revealed that high build rates correspond with least quantity of necessary VED. Hence, through higher productivity with uncompromising material integrity, productivity increases.[32]

2.7.3. Statistical Optimization: Taguchi and ANOVA Analysis

The Taguchi method represents one of the general statistical approaches which can be used in optimizing L-PBF parameters by systematically varying input factors and analyzing their consequences on the final product. This approach selects key process parameters like laser power, scan speed, hatch spacing, and layer thickness, followed by experimental design using orthogonal arrays that reduce the number of experiments to be carried out but still covers the whole area of parameter variation. Results obtained are plotted against signal-to-noise ratio graphs to highlight the best condition that gives optimal quality of the part. Using the Taguchi method in concert with ANOVA, one can find the most important parameter among all those considered in this study. In addition, such a method shows which parameters affect quality metrics, such as density, surface roughness, and mechanical strength, most. Reducing process variability allows ANOVA to provide a stable and repeatable manufacturing process. Several research works have successfully applied these statistical methods. Dzukey et al.[101] optimized the L-PBF process parameters for AISI 316L stainless steel with highly improved part density. Similarly, other researchers applied Taguchi and ANOVA techniques to DMLS of aluminum; the result was reduced surface roughness and improved overall quality of the part.[67] Despite all these advantages, the above techniques are heavily dependent on the selection of appropriate process parameters. If incorrect assumptions or experimental constraints are made in these methods, then suboptimal results may be obtained. Further refinement by machine learning and numerical modeling is required.

2.7.4. Advanced Optimization: AI, Neural Networks, and Numerical Modeling

In recent times, AI-driven techniques, especially ANNs, have gained much attention for the optimization of the L-PBF process. ANNs analyze huge amounts of historical production data to establish the correlation of process parameters with the final part properties.[28] It thus allows for automatic parameter optimization with substantial reduction in extensive experimental testing. ANNs will learn from past data and be able to predict optimal parameter combinations with changing material and design requirements, thus simplifying manufacturing. Numerical modeling is another advanced optimization approach whereby process outcomes are predicted and optimization strategies refined. As an example, thermal field modeling simulates a moving heat source on a solid material in order to predict melt pool dimensions and optimize laser parameters. Letenneur et al.[102] developed a density prediction model tailored for powder feedstock and L-PBF systems, validating their findings across multiple alloys. However, these AI-based models and numerical simulations require substantial computational resources and good-quality data for correct predictions. Poor or incomplete datasets give misleading outcomes, and hence data integrity is very important. The implementation of such models also demands specialized expertise due to the need for advanced knowledge in AI and computational modeling for precise optimization.

2.7.5. Integrating Multiple Optimization Techniques

Each method of optimization has its merits and demerits. Optimization of layer thickness is a simple way of improving productivity, but beyond threshold limits, it may result in defects. VED gives a systematic method for determining the minimum energy that is required for the proper fusion of the material to be processed and thus ensures the best compromise between speed and quality. Statistical methods like the Taguchi method and ANOVA provide data-based optimization of the parameters, ensuring better consistency and repeatability. Meanwhile, model-based and numerical simulations using artificial intelligence provide enhanced predictive capabilities and reduce the burden of trial-and-error experimentation costs. While either technique can alone be very powerful, the optimum results will surely arise from integrating experimental methods together with AI and computational modeling in a combined manner. Take full advantage of numerous optimization strategies and get superior performance from L-PBF manufacturers through good quality, faster build time, and better efficiency. Central to driving such new generations in L-PBF process optimization within an advancing field is the integral embedding of classical statistical approaches and the latest advancements in AI technology.

Chapter 3: Materials and Methods

3.1. Material

The material utilized in this study was gas atomized AlSi10Mg aluminum alloy powder, supplied by LPW Technology Ltd. Stored in sealed containers as it shown in Figure 12, the powder required careful handling due to its fine particle size and potential dust explosiveness, as indicated on the manufacturer's label. Safety measures were strictly followed, including avoiding dust inhalation, preventing contact with eyes and skin, and using protective gloves, eye protection, and respiratory equipment.

Figure 12: AlSi10Mg Powder Container supplied by LPW Technology Ltd

Throughout the process, operators managed all powder-related tasks. Initially, they loaded the AlSi10Mg powder into the machine, ensuring an even distribution in the powder bed. After printing was completed, they removed excess powder and recovered any unused material for future use. Subsequently, they carefully extracted the printed parts, cleaned the build platform, and prepared the setup for the next print job. Table 1 presents some of the as-built physical and mechanical properties of AlSi10Mg.

Table 1: some as built physical and mechanical properties of AlSi10Mg

Property	Value
Density	2.68 g/cm³
Melting Point	570–610°C
Yield Strength	200–250 MPa
Ultimate Tensile Strength	350–400 MPa
Hardness	110–120 HV
Young's Modulus	70–75 GPa
Fatigue Strength	110–150 MPa

3.1.1. Particle Size Distribution (PSD) Analysis

The particle size distribution (PSD) analysis of the AlSi10Mg powder was carried out using the "Litesizer DIA 500 by Anton Paar", a dynamic image analysis (DIA) system. This high-precision instrument as we can see in Figure 13, provides valuable insights into particle size and morphology, both of which are crucial for additive manufacturing (AM) applications.

To ensure accurate dispersion without agglomeration, the machine operates with a dry Jet module. As the powder particles pass through the detection zone, high-resolution images are captured, allowing for a detailed analysis of size distribution. This ensures optimal flowability and powder bed performance, which are essential for L-PBF processes.

Figure 13: Litesizer DIA 500 by Anton Paar used for particle size distribution analysis

The particle size distribution of the AlSi10Mg powder, according to the manufacturer, was 15-45 µm. For confirmation of its accuracy and suitability for application in AM, however, an independent analysis was conducted through the dry Jet method. The results provided slightly variant values from those of the manufacturer, which provided a d10 (10% of particles are smaller than this size) of 24.9 µm, d50 (median particle size) of 35.1 µm, a d90 (10% of particles are smaller than this size) of 45.6 µm, and mean particle size of 35.2 µm. The result indicates a marginally higher mean particle size from the stated range, highlighting the importance of independent verification before powder use in L-PBF processes.

Besides particle size distribution, the study also investigated the aspect ratio of powder particles to establish their shape properties. The aspect ratio, as a measure of the ratio of the shortest to the longest particle dimension, is an indicator of powder flowability and packing density. The study revealed that most particles have a nearly spherical morphology, a best property for additive manufacturing. A more rounded form ensures even powder spreading, minimizes porosity, and

maximizes laser absorption, all of which contribute to improved printing quality. Figure 14 illustrates particle size distribution and aspect ratio charts obtained from analysis.

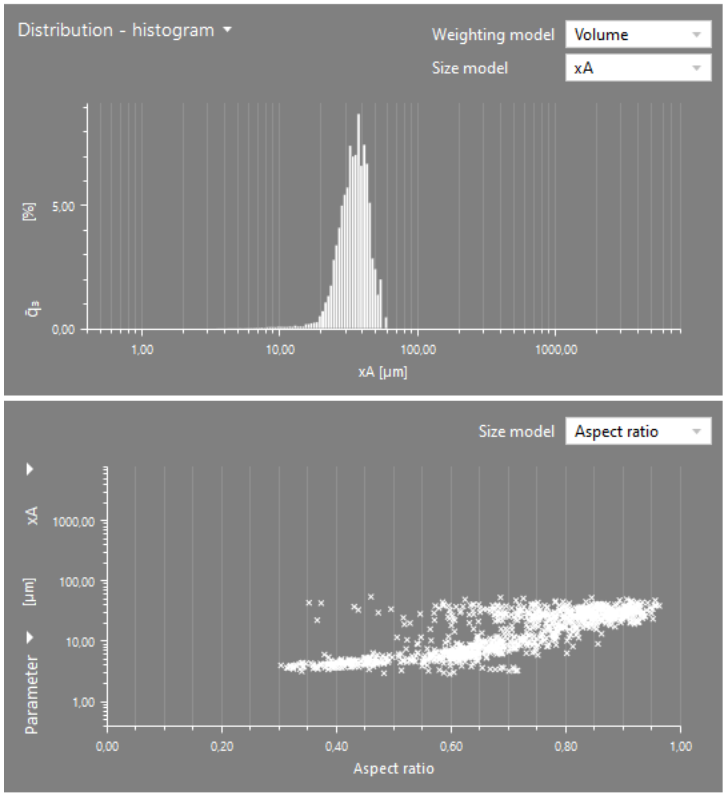

Figure 14: particle size distribution and aspect ratio charts

According to the "ASTM F3319" standard, the chemical composition of the AlSi10Mg alloy is specified in Table 2.

Table 2:chemical composition of the AlSi10Mg alloy

Elements	**Al**	**Si**	**Mg**	**Fe**	**Mn**	**Zn**	**Ti**	**Cu**	**Ni**	**Sn**	**Pb**
Composition (%)	Balanced	9.0-11.0	0.20-0.45	≤ 0.55	≤ 0.45	≤ 0.10	≤ 0.15	≤ 0.05	≤ 0.05	≤ 0.05	≤ 0.03

3.2. Sample Modeling

The first step in sample modeling involved creating CAD files using "Materialise Magics" software, where a total of 54 cubes were designed for the modeling process. Figure 15 illustrates the exact dimensions of the samples.

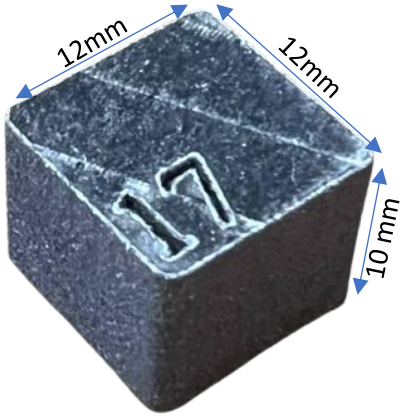

Figure 15: Nominal dimension of the cubic samples

Then, the software was utilized to define the pre-determined layer thickness for each component based on design of experiment. Figure 16 presents the "Materialise Magics" software environment, where geometry is established, slicing is executed, and layer thickness is assigned. Additionally, this environment allows for nesting, as demonstrated in Figure 16 for one group of samples. Moreover, the samples were engraved with numerical identifiers during production (as referenced in the sample ID in Table 3) to differentiate them based on their specific process parameters.

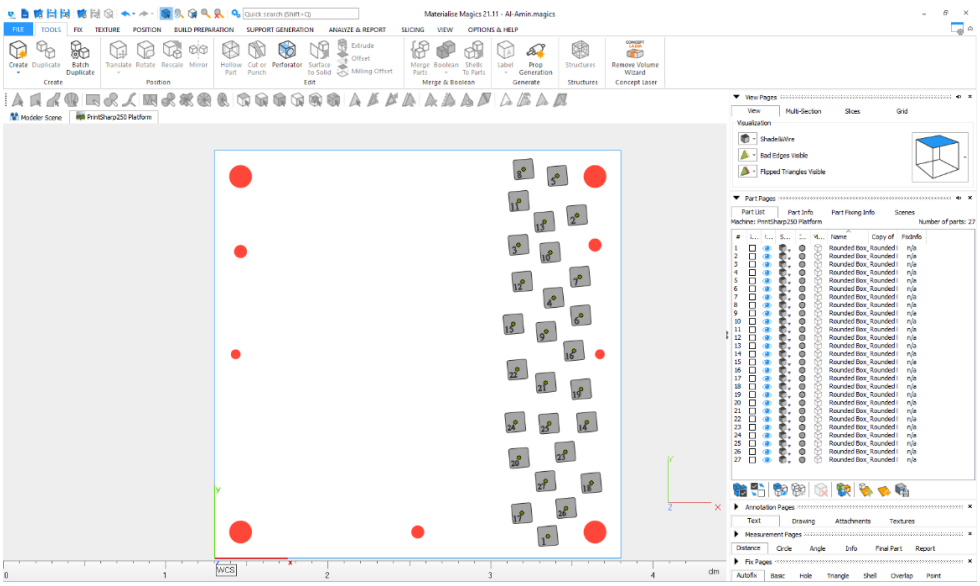

Figure 16: Illustration of the CAM model which depicts the positioning of the 27 samples on the platform

3.2.1. Design of experiment

The selection of appropriate process parameters is extremely significant for product quality improvement. How these parameters interrelate should be noted, as changing one parameter might have the same outcome as changing another at times. Overall, the balance between all the criteria is to be retained. In order to maximize the production rate and enhance the quality of the production, which are the key aims of this thesis research, one must choose the most favorable process parameters.

While all the process parameters influence the efficiency of the process, Only the most important individuals were considered to meet the target. After cautious consideration, 54 experimental data points were selected for a wide variety of four process parameters, including layer thickness (L), laser power (P), laser scan speed (v), and laser hatch distance (h) as presented in Table 3.

This selection was based on prior experience with the machine and a preliminary analysis, which is not reported here. The "EP Hatch Prima" software was then used to set these parameters, generating a total of 54 different EPI files, divided into two groups of 27 samples each. The only difference between these two groups was the layer thickness which was set to 40 and 60 microns for the two groups in "Materialise Magics" software.

As shown in Table 3 the laser power ranged between 310 and 390 W, and the scan speed and hatch distance varied between 1200 and 1600 mm/s and 0.12 and 0.13 mm, respectively. This wide parameter range resulted in significant variations in volumetric energy density (VED), which quantifies the amount of input energy per unit volume of the powder bed. VED was introduced to enable a meaningful comparison between different parameter sets.

Table 3: Process parameters for each sample used in this thesis.

S ID.	Layer thickness [mm]	Laser Power [W]	Scan speed [mm/s]	Hatch distance [mm]	VED $[j/mm^3]$	Build Rate $[mm^3/s]$	Layer thickness [mm]	Laser Power [W]	Scan speed [mm/s]	Hatch distance [mm]	VED $[j/mm^3]$	Build Rate $[mm^3/s]$
1	0.04	310	1200	0.11	58.7	5.28	0.06	310	1200	0.11	39.1	7.92
2	0.04	310	1200	0.12	53.8	5.76	0.06	310	1200	0.12	35.9	8.64
3	0.04	310	1200	0.13	49.7	6.24	0.06	310	1200	0.13	33.1	9.36
4	0.04	310	1400	0.11	50.3	6.16	0.06	310	1400	0.11	33.5	9.24
5	0.04	310	1400	0.12	46.1	6.72	0.06	310	1400	0.12	30.8	10.08
6	0.04	310	1400	0.13	42.6	7.28	0.06	310	1400	0.13	28.4	10.92
7	0.04	310	1600	0.11	44.0	7.04	0.06	310	1600	0.11	29.4	10.56
8	0.04	310	1600	0.12	40.4	7.68	0.06	310	1600	0.12	26.9	11.52
9	0.04	310	1600	0.13	37.3	8.32	0.06	310	1600	0.13	24.8	12.48
10	0.04	350	1200	0.11	66.3	5.28	0.06	350	1200	0.11	44.2	7.92
11	0.04	350	1200	0.12	60.8	5.76	0.06	350	1200	0.12	40.5	8.64

12	0.04	350	1200	0.13	56.1	6.24	0.06	350	1200	0.13	37.4	9.36
13	0.04	350	1400	0.11	56.8	6.16	0.06	350	1400	0.11	37.9	9.24
14	0.04	350	1400	0.12	52.1	6.72	0.06	350	1400	0.12	34.7	10.08
15	0.04	350	1400	0.13	48.1	7.28	0.06	350	1400	0.13	32.1	10.92
16	0.04	350	1600	0.11	49.7	7.04	0.06	350	1600	0.11	33.1	10.56
17	0.04	350	1600	0.12	45.6	7.68	0.06	350	1600	0.12	30.4	11.52
18	0.04	350	1600	0.13	42.1	8.32	0.06	350	1600	0.13	28.0	12.48
19	0.04	390	1200	0.11	73.9	5.28	0.06	390	1200	0.11	49.2	7.92
20	0.04	390	1200	0.12	67.7	5.76	0.06	390	1200	0.12	45.1	8.64
21	0.04	390	1200	0.13	62.5	6.24	0.06	390	1200	0.13	41.7	9.36
22	0.04	390	1400	0.11	63.3	6.16	0.06	390	1400	0.11	42.2	9.24
23	0.04	390	1400	0.12	58.0	6.72	0.06	390	1400	0.12	38.7	10.08
24	0.04	390	1400	0.13	53.6	7.28	0.06	390	1400	0.13	35.7	10.92
25	0.04	390	1600	0.11	55.4	7.04	0.06	390	1600	0.11	36.9	10.56
26	0.04	390	1600	0.12	50.8	7.68	0.06	390	1600	0.12	33.9	11.52
27	0.04	390	1600	0.13	46.9	8.32	0.06	390	1600	0.13	31.3	12.48

The resulting combinations for each sample in terms of VED and build rate (BR), obtained by varying the process parameters, are shown in Figure 17 and Figure 18.

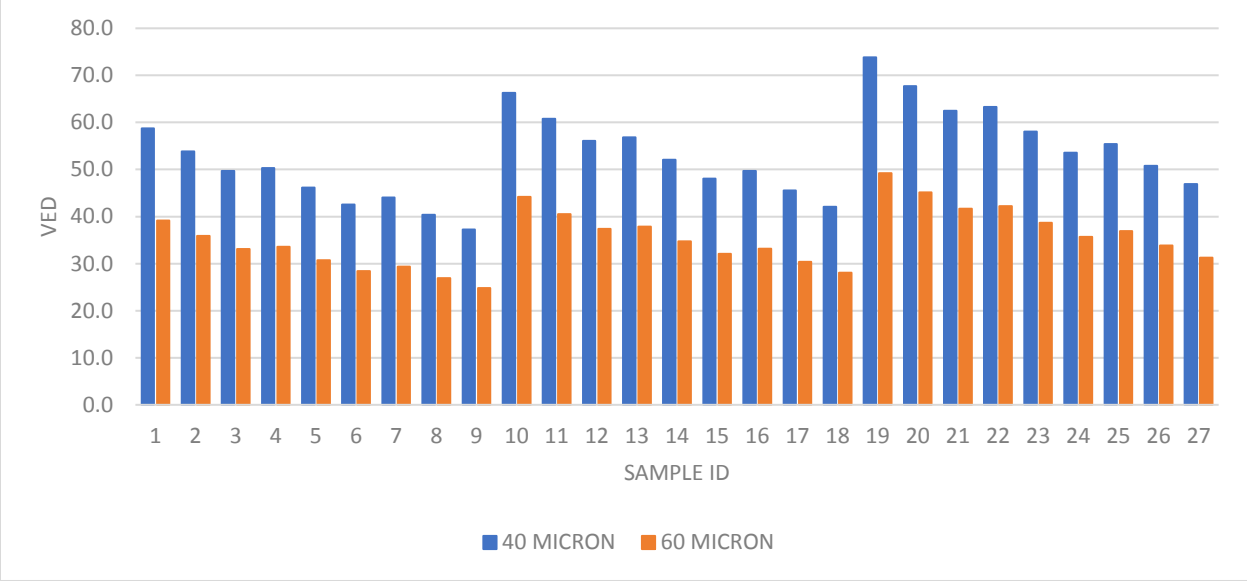

Figure 17: Volumetric energy density based on sample ID

Subsequently, the predefined files served as the input for the PrintSharp 250 machine.

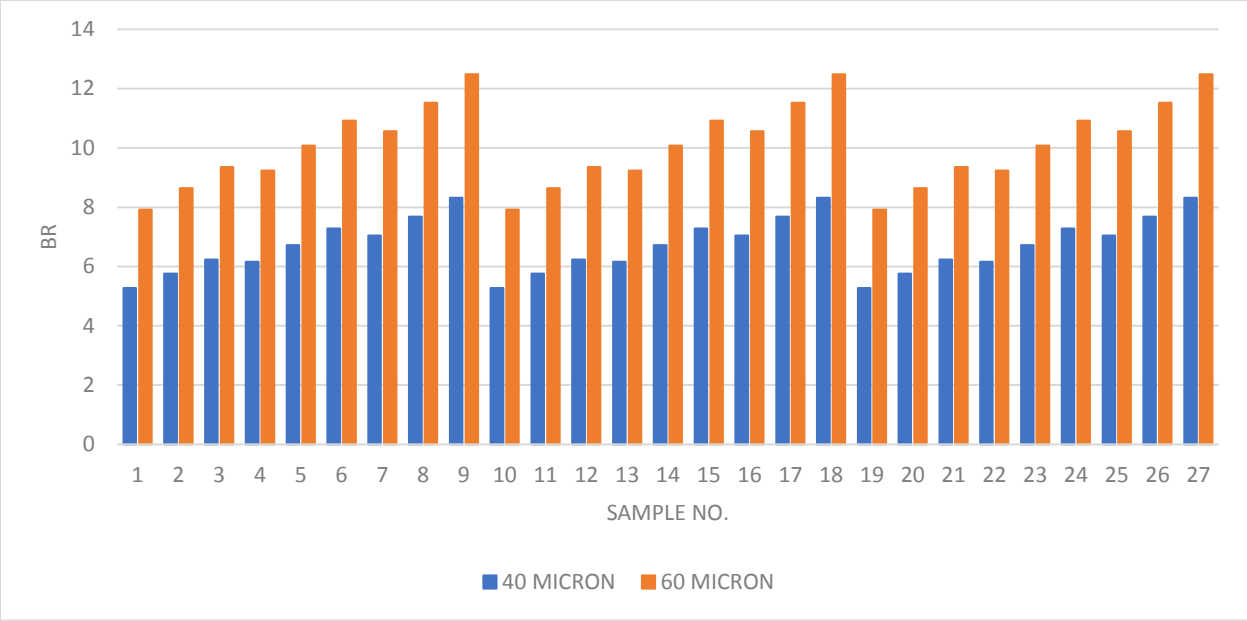

Figure 18: Build rate based on sample ID

3.3. Samples Manufacturing

The samples were fabricated using the "PrintSharp 250 (Figure 19) by Prima Additive", a PBF machine designed for medium volume applications and specifically serves the industrial production of complex components while offering great flexibility for parts management. The technical features of the machine are documented in Table 4.

Figure 19: Prima Additive Print Sharp 250

Table 4: The technical parameters of the PrintSharp 250

Category	Specification
Dimensions (L.W.H)	3500 (L)- 1100 (W)- 2450 (H) mm
Weight	2000 kg
Power Supply	380 V/50 Hz/8kW
Type of laser	Yb (Ytterbium) Fiber Glass
Laser Power	200 W/ 500 W (Optional)
Laser Focus Diameter	70 – 100 µm
Beam Wavelength	1060 – 1080 nm
Building Volume	250 x 250 x 300 mm
Beam Deflection Speed	8 m/s
Positioning Speed	10 m/s
Build rate	12 – 30 cm^3/h
Layer Thickness	0.02 – 0.1 mm
Layer Width	0.1 mm (single line width)
Recoater Specs	Travel: 650 mm
Building Platform z-axis	Travel: 300 mm/Speed max: 6 mm/s/Res: 0.01 mm
Heating Platform	Up to 200°C
Monitoring of O_2 Level	Below 100 ppm
Permissible Room Temperature	15 – 30°C
Gas (Consumption – running/filling)	7 l/min (running)
System Fill Consumption	20 l/min (up to filling)
Cam Software	Materialise Magics
Control & Other Software	Eplus control software (EPC)
Industrial Interfaces	Ethernet

Before starting the production process, the build chamber was thoroughly emptied to a residual oxygen level of less than 0.1%. High-purity Argon was used to preserve an inert atmosphere within the construction chamber and minimize the likelihood of oxidation.

A scanning approach was employed using a bidirectional stripe scanning pattern with a 67° rotation between each succeeding layer. This rotation helps reduce residual stresses, minimize anisotropy, and improve mechanical properties.

Finally, it takes 3 hours and 22 minutes for first job for printing samples with 40-micron layer thickness to finish and 2 hours and 15 minutes for second job for printing samples with 60-micron layer thickness to finish.

On Figure 20, the highlighted section is imaging the laser being used as it is doing the L-PBF process by heating to melt a thin layer of metal powder to achieve the desired form. It also shows the manufactured samples joint to the building platform after the build process is complete. Once production was finished, all the parts that are connected to the platform were taken out of the build chamber with care and thoroughly cleaned.

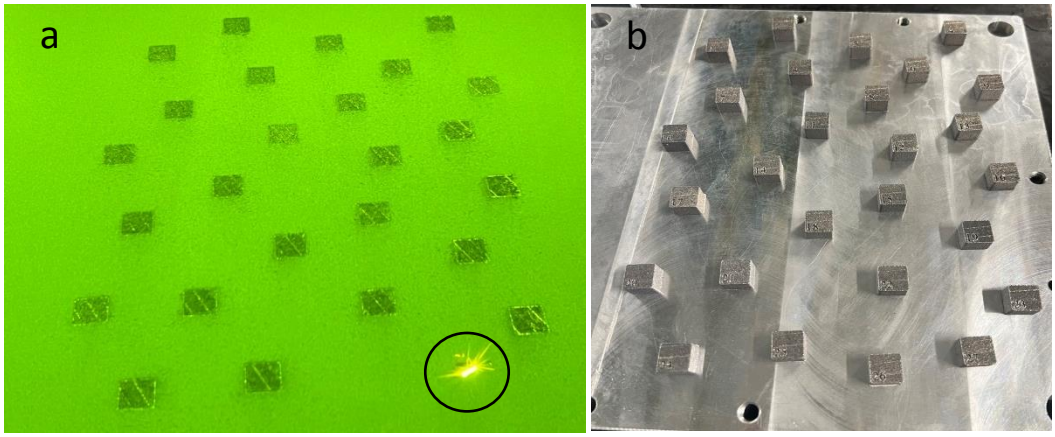

Figure 20: (a) the platform during job running, (b) the result after completion of production:

3.4. Sample characterization

First, wire electrical discharge machining (W-EDM) was utilized to carefully cut the built samples from the build platform with minimum material loss and without any degradation in parts' integrity. Afterwards, a stereo microscope was utilized to capture high-magnification surface images, allowing the initial investigation of the surface morphology and defects.

Following this, the part density was determined using the Archimedes method. After obtaining and examining the density findings, certain samples were selected for further characterization using X-ray computed tomography (XCT) and metallography.

Optical microscopy was then used, providing details on porosity distribution. At the same time, XCT data were analyzed and processed using VGStudio software to assess internal features such as porosity, defects, and overall structural integrity in a non-destructive manner.

Finally, compression tests were conducted to evaluate the mechanical behavior of the samples. Through this comprehensive suite of analysis, the material properties, and mechanical performance of the printed components were well understood.

3.4.1. Detaching Samples

The "G.cut W-EDM" cutting machine was utilized to cut the samples at this precise stage, as illustrated in Figure 21.

Section A represents the computer of the cutting machine, which is used for software applications, including regulating wire movements, the automated process, and start/stop cutting options. Section B indicates the X, Y, and Z coordinate directions, ensuring that the cutting is performed accurately in the intended direction. Section C is the area where the workpiece is secured, and the cutting operation takes place.

The operation starts by clamping the platform to the W-EDM. (Figure 22(a)) Then, with the specific software on the computer connected to the machine, a surface touch was established between the wire and the platform to establish the point of reference for X and Y coordinates. After proportionately adjusting the exact position for the start of the wire, the corresponding dimensions and the correct orientation were inputted into the machine to start cutting. Finally, the printed parts were cut and prepared for future procedures.[103]

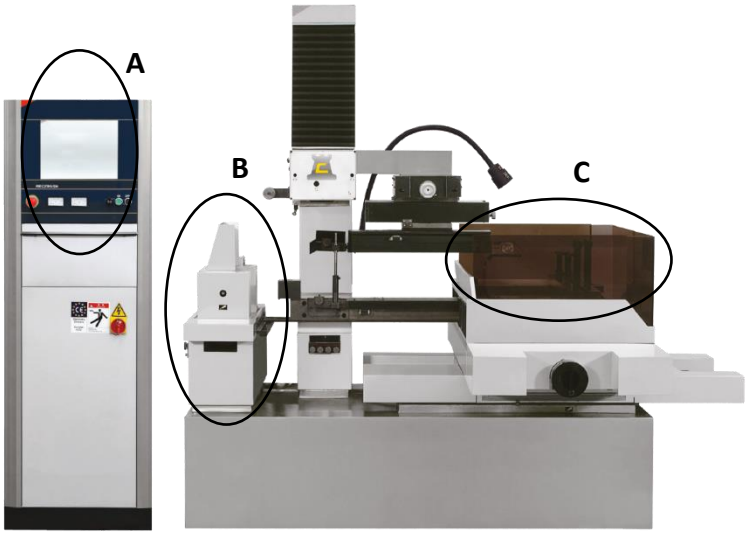

Figure 21: Key components of the WEDM machine: Section 1 (software controls), Section 2 (coordinate display), and Section 3 (cutting area)

The wire-cutting machine uses an electrically charged thin wire to trim the samples with utmost accuracy. It operates by creating electrical discharges between the workpiece and the wire that remove material along the direction of the cut stepwise. The sparks are produced effectively and rapidly, resulting in the removal of tiny volumes of metal and the desired form of the workpiece. Throughout the cutting procedure, as shown in Figure 22(a), a constant flow of deionized water is used for cooling the workpiece and wire and to prevent excessive heat and wash away the eroded particles. Water is also used as a dielectric during this procedure, which is required for the phenomenon of the electrical discharge process.

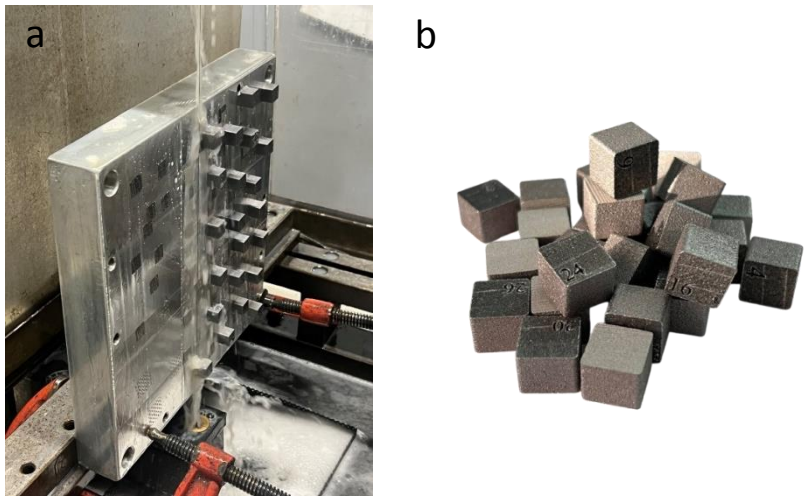

Figure 22: (a) Build platform clamped to Wire-EDM machine, (b) Samples after cutting

3.4.2. Surface Imaging

Surface examination was conducted using a "Leica stereo microscope" as in Figure 23 to examine the topography and morphological features of the manufactured components. Imaging was done at 1x and 5x magnifications to view both a general observation and a detailed surface. The multi-scale analysis verified extensive examination of the surface quality, thus resulting in better comprehension of the impact of the manufacturing process on the finished product.

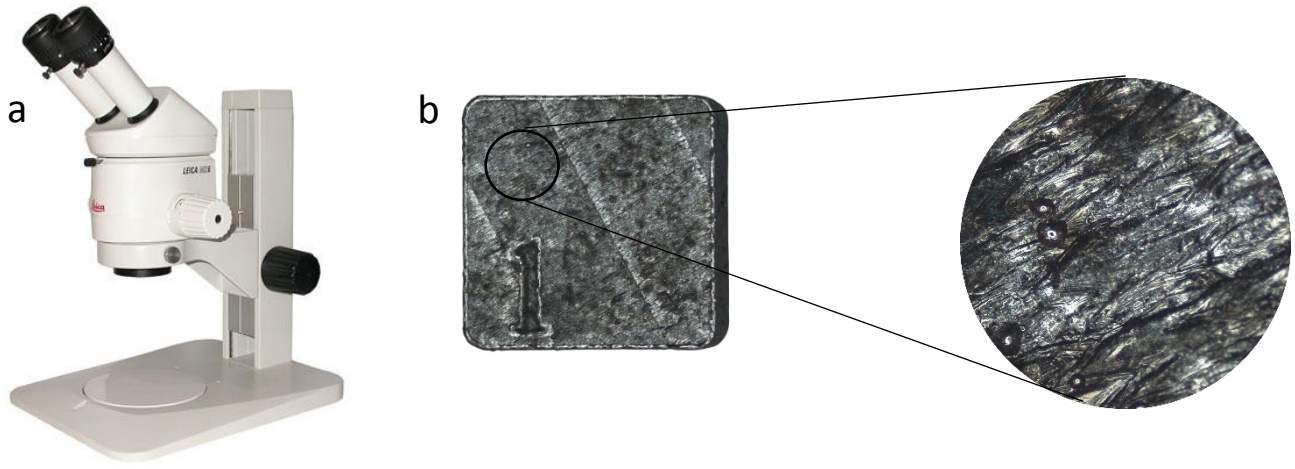

Figure 23: (a) Leica stereo microscope, (b) images taken with 1X and 5X resolution

3.4.3. Surface Roughness Test

Surface roughness was measured using a profilometer (RTP80-TL90, Someco SM SRL, Italy) as in Figure 24 to characterize the surface texture of the parts produced. The equipment functions by tracing a high-precision stylus over the surface, detecting height differences and producing a full profile of surface topography. This method enables the measurement of vital roughness parameters, like Ra (arithmetical mean roughness), Rz (profile height, max) and Rt (total height variation), that provide a measure of the quality of manufacture and surface integrity of the sample.

To ensure reliability and accuracy, three separate measurements were conducted at different locations on each sample. The obtained values were averaged to determine the representative roughness parameter for each surface, minimizing localized variations and measurement uncertainties. The profilometer was configured with appropriate cut-off lengths and stylus speed settings based on standard surface metrology guidelines.

By merging the measurements of surface roughness with mechanical examinations, one can achieve a complete picture of material performance to achieve optimization of process parameters for supplying better surface quality.

Figure 24: Profilometer and measuring setup

3.4.4. Archimedes Density measurement

The Archimedes method is used to determine the relative densities of components made by SLM. It involves measuring one sample in two different fluids. As a rule, the reference fluid is air. The second fluid can be distilled water, acetone, or ethanol. Although the utilization of distilled water is more general, it should not always be used since air bubble formation on the surface of the

sample is a risk. The phenomenon is largely observed in lattice structure components when air bubbles prevent the complete penetration of water into the mesh interior due to the high surface tension of the water.

According to the ASTM F3637-23, Archimedes measurement technique was carried out for each sample to calculate its geometrical and Archimedes density using "Kern density balance" as in Figure 25.

At first, the measuring chamber is set up and the beaker is filled with distilled water, with a weight of 0.997 g/cm^3. The instrument is then accurately calibrated in order to measure the dry weight (w_{dry}) of the sample, as indicated in Figure 25 (point 1).

Once the dry weight of the sample is determined, it is shown on the digital display, once this has been done, the device is reset to zero and the sample is placed on a fine-mesh filter, as in Figure 25 (point 2), to be fully immersed in distilled water. All the bubbles that had formed were wiped off, and the sample was completely immersed in the water. The weight at this point was taken as immersion weight ($w_{\text{immersion}}$).

The sample was then taken out of the water, moved to the wet wipes, and weighed immediately, in order to measure how much water was absorbed when immersed. This phase resulted in the acquisition of wet weight (w_{wet}).

To ensure measurement accuracy and repeatability**,** each sample was tested three times, and the recorded values were averaged to obtain a reliable density measurement.

Having relative theoretical powder density equal to 2.68 g/cm^3 , The final porosity percentage and relative Archimedes density percentage of all the samples were then computed according to the formulas provided:

$$Archimides\ density\ (apparent\ density) = \rho_{Archimides} = \rho_{Liquid} * \frac{w_{dry}}{w_{dry} - w_{\text{immersion}}} [\frac{g}{cm^3}] \quad (15)$$

$$\text{Geometrical density (bulk density)} = \rho_{Geometrical} = \rho_{Liquid} * \frac{w_{dry}}{w_{wet} - w_{\text{immersion}}} [\frac{g}{cm^3}] \quad (16)$$

$$Total\ porosity\ percentage = \frac{\rho_{Theoretical} - \rho_{Bulk}}{\rho_{Theoretical}} * 100\% \quad (17)$$

$$Relative\ Archimides\ density\ percentage = \frac{\rho_{Archimides}}{\rho_{Theoretical}} * 100\% \quad (18)$$

Figure 25:(a) Kern density balance setup, (b) sample on the filter in the water

3.4.5. X-ray Computed Tomography

X-ray Computed Tomography was performed using the "Phoenix v|tome|x S system" as in Figure 26, which employs Cone Beam for high-resolution, non-destructive imaging. This system captures 3D representations by compiling multiple X-ray projections taken around a rotational axis over a full 360° scan. The X-ray source emits a 3D cone-shaped beam, which is detected by a 2D flat-panel detector, enabling entire sample imaging in a single exposure.

Figure 26: Phoenix v|tome|x S XCT system

Ten samples were chosen for XCT analysis based on the Archimedes density measurement method data. These samples were analyzed by tomographic method to measure their porosity percentage and density, which would be compared with alternative methodologies. The samples were initially positioned on the holder in this procedure, as depicted in Figure 27(a).

In Figure 27(b), a 0.1 and a 0.5 copper filters were positioned in front of the X-ray gun to reduce beam-hardening effects and improve contrast. The sample position was verified and corrected using the software in the computer connected to the machine, to guarantee that the sample stayed within the X-ray imaging frame. Once the correct placement is confirmed, the tomography process begins.

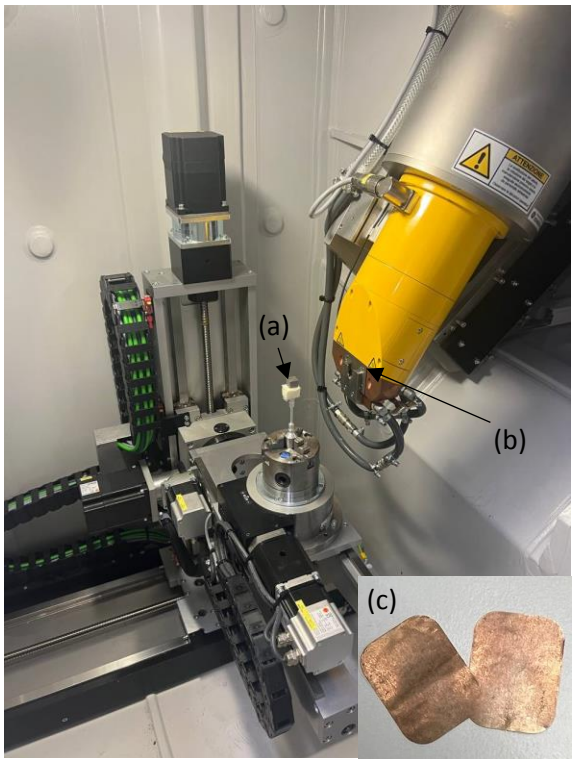

Figure 27: interior XCT setup: (a) sample holder for tomography, (b) X-ray beam gun, (c) copper filters

After completing the scan, first, we used "Phoenix datos|x" for 3D reconstruction of the XCT data and to apply beam hardening correction to reduce artifacts caused by uneven X-ray absorption and make material appears more homogenous as in Figure 28.

Subsequently, using "VGStudio MAX software" over-segmentation errors were adjusted to distinguish solid regions from porosities accurately and acquire final data (Figure 29).

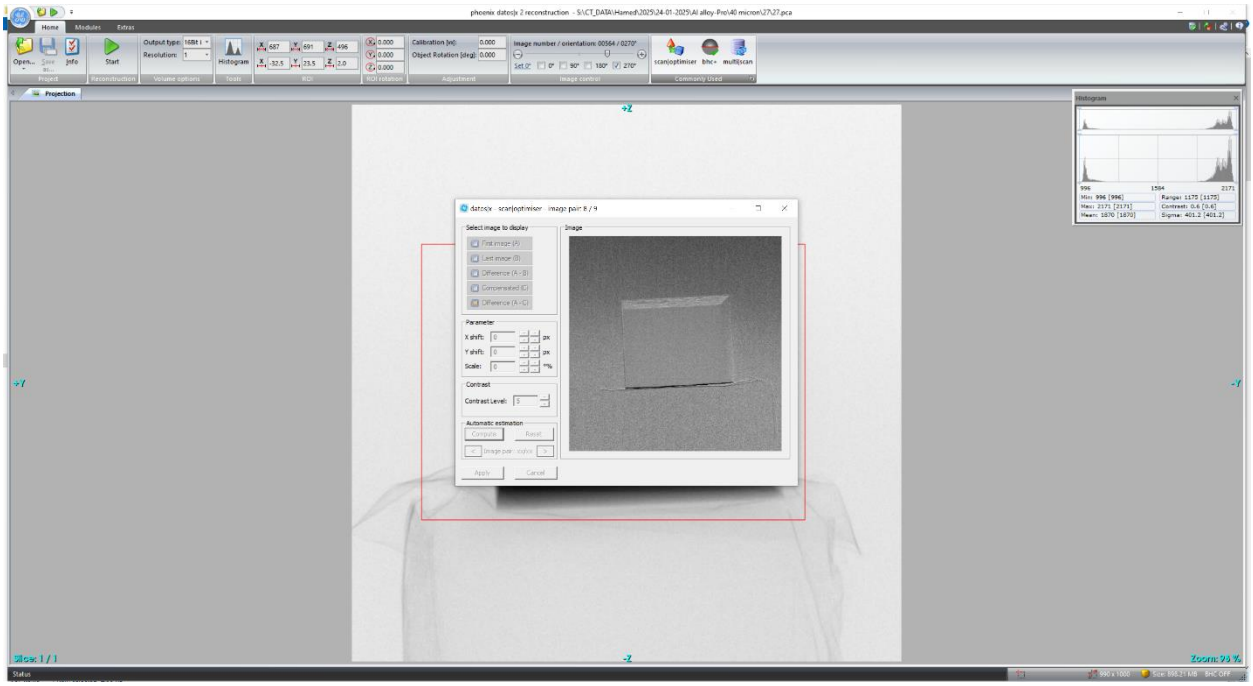

Figure 28: "Phoenix datos|x" software for 3D reconstruction of the XCT data

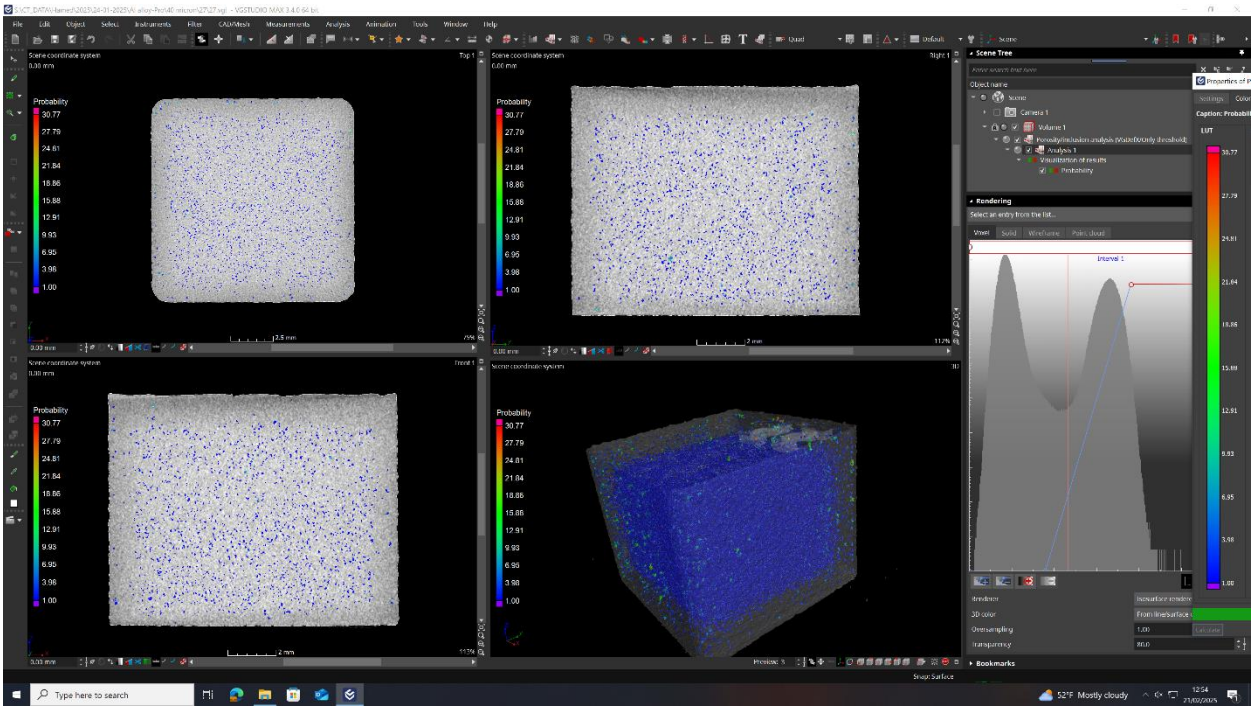

Figure 29: "VGStudio MAX software" for adjusting over-segmentation errors

3.4.6. Metallography

After the completion of tomography analysis of the ten samples, metallographic analysis was carried out. Grinding and polishing were performed with the help of a "Presi - minitech 250 SP1" machine, as illustrated in Figure 30 (a). Initially, abrasive papers of grit sizes P600, P800, P1200, and P2400 were utilized (Figure 30 (b)). Grinding was initiated using the coarsest abrasive paper, which was initially wetted and then applied to the machine. The samples were then ground at 150 rpm rotational speed.

To prevent scratching due to remnant particles, water was run continuously on the abrasive surface during the procedure. The samples were examined microscopically following each cycle of grinding in order to assess the visibility of the grinding lines (Figure 31). When the visibility of the lines was distinct, the sample was turned 90 degrees and finer grit abrasive paper was used in order to scrape off the prevailing lines and leave new ones. This was repeated repeatedly until the final grinding stage using P2400 paper was accomplished.

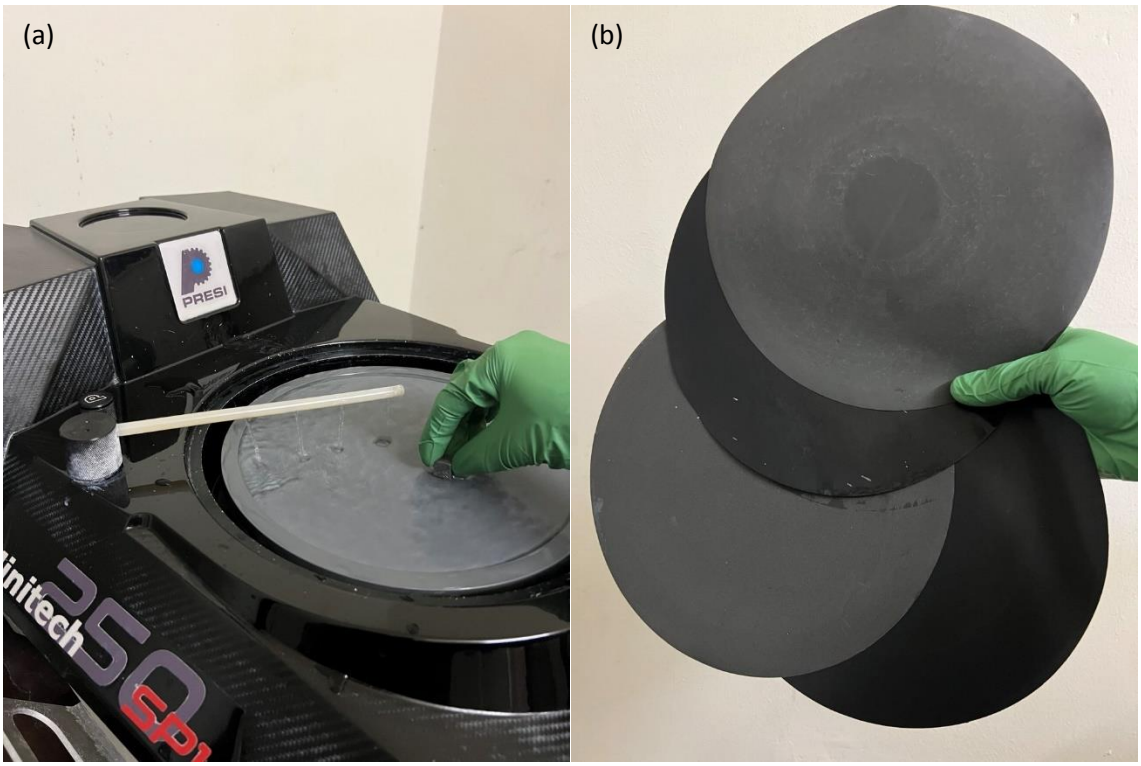

Figure 30: The Presi machine was used for the grinding and polishing of the samples. (b) The selection of abrasive papers (P600, P800, P1200, and P2400) used for grinding the samples.

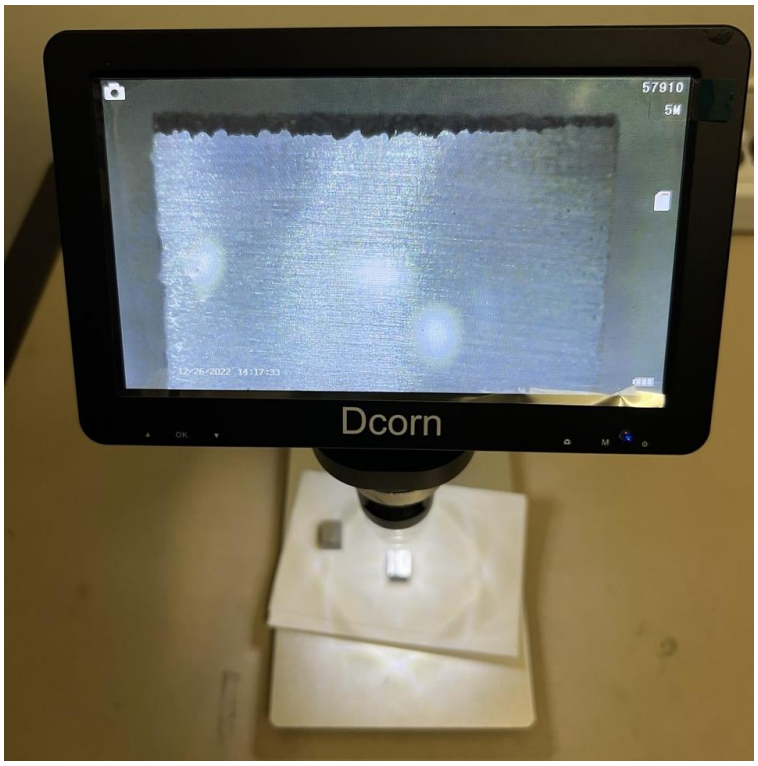

Figure 31: using microscope for assessing the visibility of the grinding lines

After the grinding stage, the samples were polished to eliminate the scratches caused by the previous procedures first with blue polishing pad with grit size of $3\mu m$ (Figure 32). The pad was positioned on the device, and diamond paste of 3μ, together with a lubricant, was utilized to attain a polished surface (Figure 33). The samples were then polished at 80 rpm rotational speed and water was run continuously on the polishing surface during the procedure.

Subsequently, the surface was further refined using the $1\mu m$ red polishing pad and a 1.4μ diamond paste with lubricant.

Figure 32: 1.4µ and 3µ diamond paste

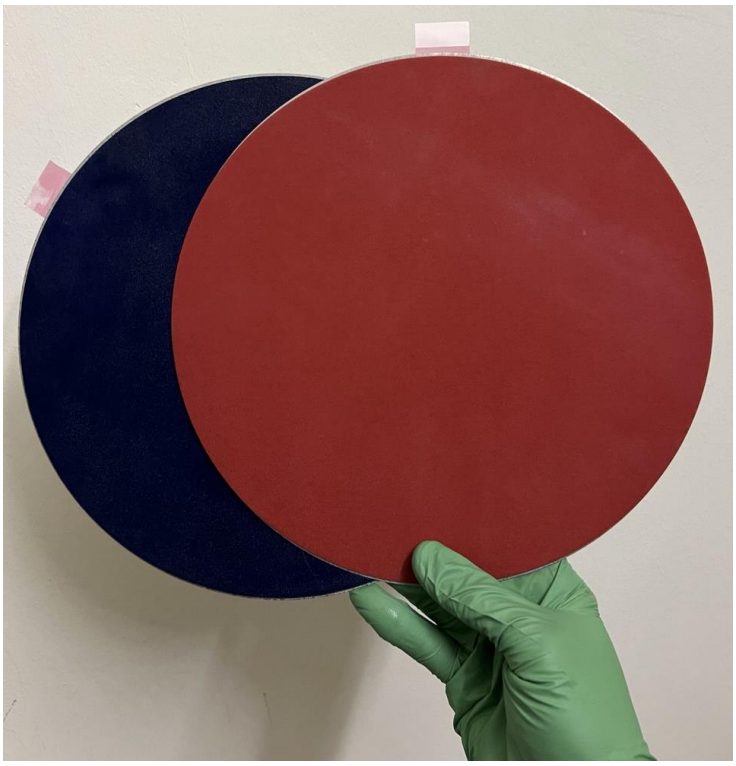

Figure 33: Polishing pads with 3-micron(blue) and 1-micron(pink) grit sizes were used for polishing the samples

After this phase, the surfaces of the sample were supposed to be very smooth and reflective, such as a mirror. The samples were now prepared for the subsequent phase, in which the microstructure was analyzed using an optical microscope at 50X magnification for defect determination.

3.4.7. Optical Microscope

The surface of the samples was inspected using an optical microscope after polishing. In this research, a "LEICA DM6 M" optical microscope (Figure 34(a)) was utilized that had magnification options ranging from 5x to 100x. The microscope is equipped with software "LAS X" that includes advanced image processing capabilities. (Figure 35)

The samples were placed on a special plane (Figure 34 (b)). The surface inspection was carried out at a magnification of 50x. Each surface was divided into nine separate areas, a matrix. Nine photos were taken for each sample. The average percentage porosity of all nine photos was calculated to find out the percentage porosity of a sample. The microscope focus was precisely adjusted for each photo in order to have optimum sharpness of the surface pores. The photographs exhibit black spots on the background, which are the porosities in the provided section.

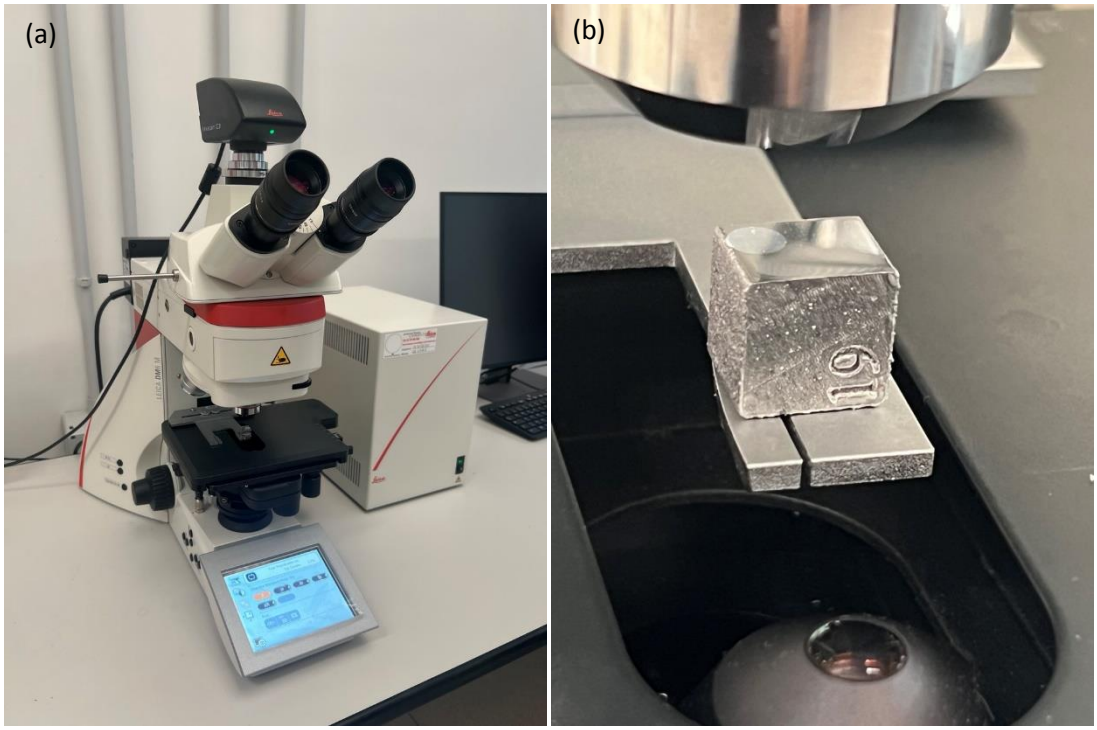

Figure 34: (a)Schematic of the optical microscope used for capturing high-resolution images, (b)The sample is placed in the position for analysis.

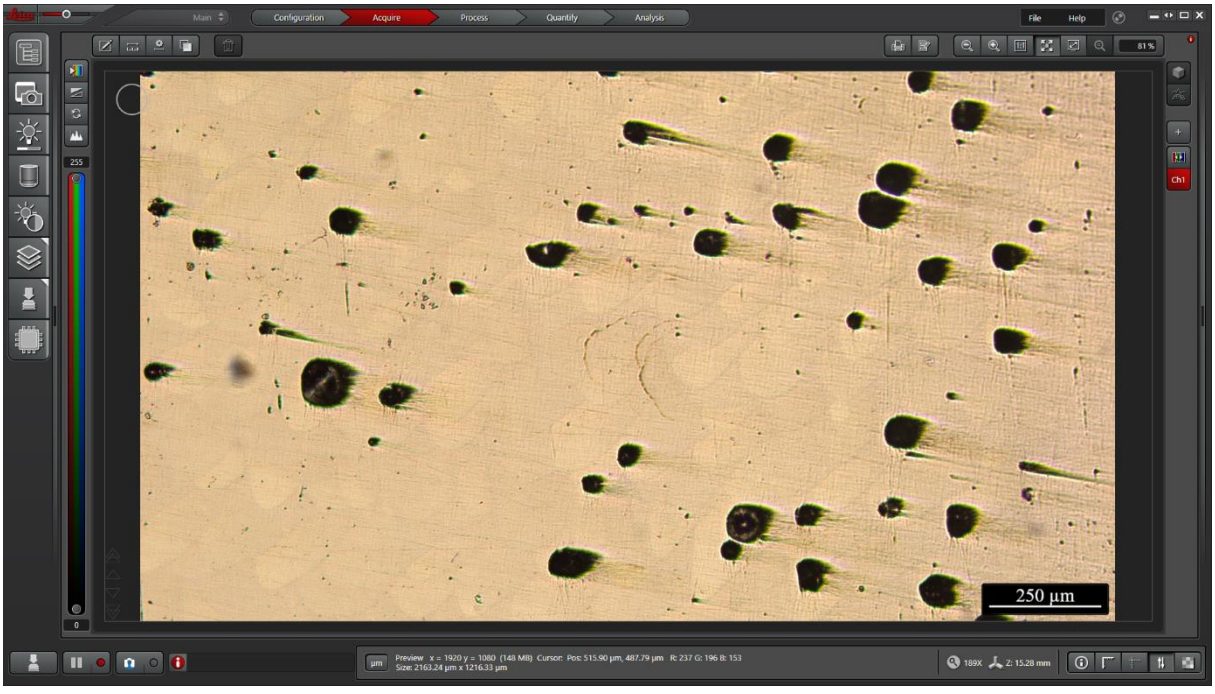

Figure 35: LAS X" software used for image processing

3.4.8. Image Analysis

Following the acquisition of images, they processed using the software ImageJ (Figure 36). ImageJ is a Java program that was initially designed by the National Institutes of Health in America for analyzing and processing images. ImageJ software was used to analyze the percentage of porosity of the samples, as shown in Figure 37 as the image of one of the samples with porosity content of 5.763%.

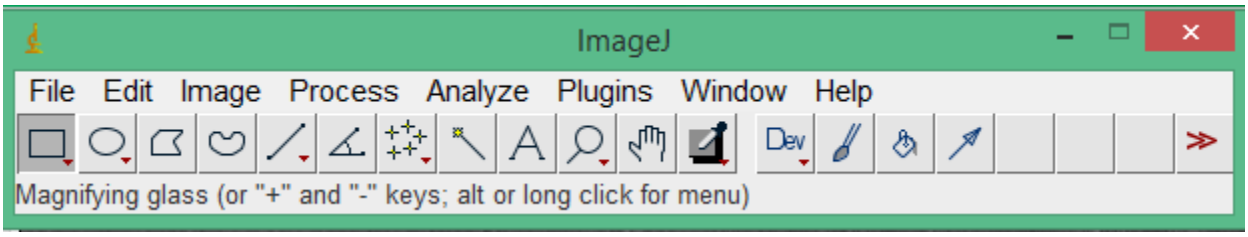

Figure 36: ImageJ software

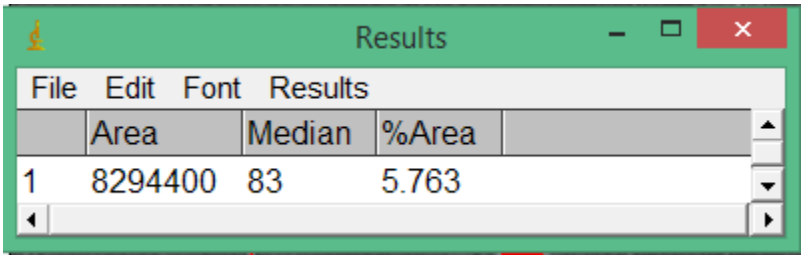

Figure 37: Analysis of sample porosity using ImageJ software, demonstrating the quantification process of porosity within the sample.

ImageJ requires an image that contains 8 bits, so the first step was converting the image to 8-bit format, which eventually led to the creation of a grayscale representation where the color of each pixel is determined according to the strength of the greyscale. The program allowed for better quantitation of the pore's density of surfaces as well as pore size. By adjusting the threshold to prevent any distortions that were caused by polishing and any scratches that were still present, it became possible to precisely measure the percentage of darkened regions that corresponded to the pores in the samples. (Figure 38)

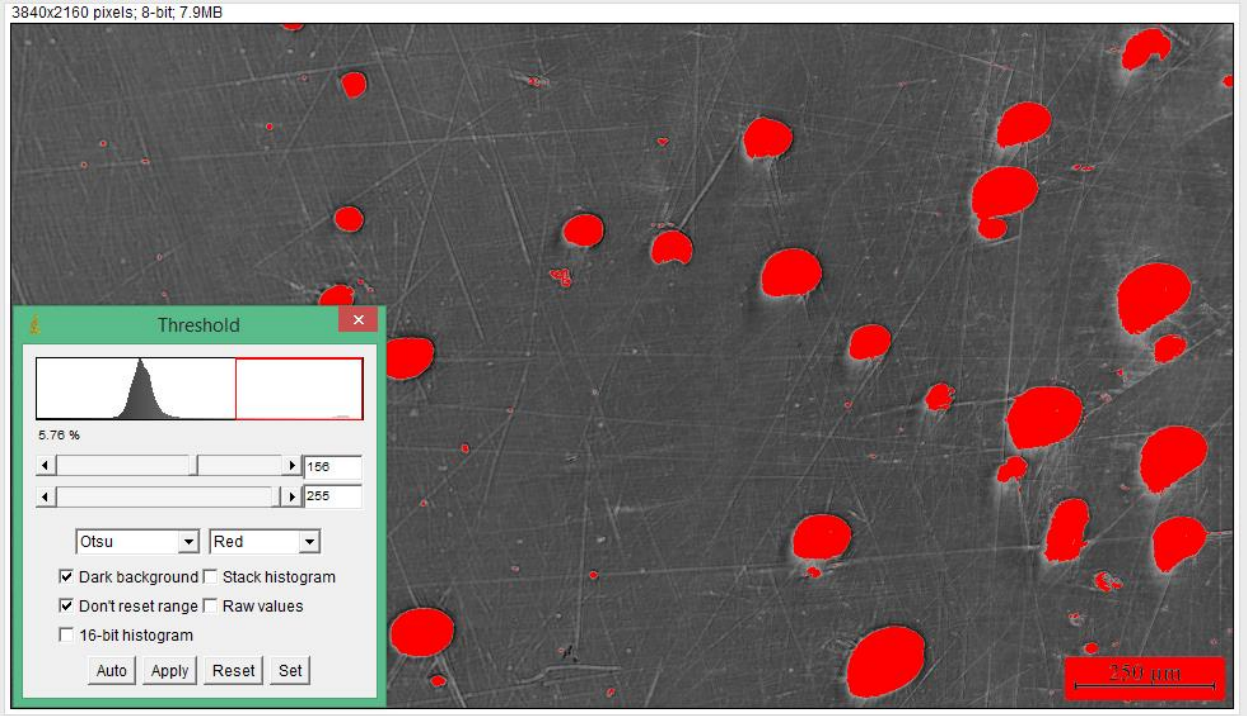

Figure 38: Representation of the grayscale image was processed in ImageJ using thresholding to measure the pores (shown in red), while excluding any polishing errors and scratches.

For each cross-section of every sample, nine images were captured using an optical microscope. Each image was analyzed individually using the software to determine its porosity content. After obtaining the porosity values for all nine images, their average was calculated to represent the total porosity of that cross-section for each sample.

3.4.9. Compression Test

The 'EASYOUR' compression testing machine was used to evaluate the compressive strength of materials. It applies a uniform compressive force through precisely positioned plates, ensuring controlled and accurate loading. A displacement sensor tracks deformation, and the control system records force and displacement data for analysis. (Figure 39)

Compression tests were conducted on samples. Minor variations in material removal during wire cutting and metallographic preparation could introduce slight inconsistencies in initial dimensions, which were minimized through careful height and area measurement before testing.

Samples were positioned with the upper surface facing upward, aligned with the print direction for consistency. Manual calibration was performed to position the compression weight near the sample surface, ensuring precise control of initial conditions.

The test began when the weight contacted the sample. The machine gradually increased the pressure at a controlled velocity of 0.3 mm/min, characteristic of quasi-static testing, until the sample exhibited deformation or failure. The equipment continuously monitored and recorded force and displacement, which were later analyzed to determine mechanical properties such as stiffness and failure locations.

A preload of 1000 N was applied, with the machine's maximum load capacity at 100 kN. The recorded data represented engineering compression measurements, rather than true stress-strain data, because the force was measured directly from the load cell and divided by the initial cross-sectional area, without accounting for instantaneous changes in area or local material behavior.

Instantaneous changes in cross-sectional area were calculated by dividing the constant sample volume by the instantaneous height during deformation. True stress-strain data considers real-time changes in cross-sectional area due to material deformation.

Analysis of mechanical properties included compressive strength, yield strength, and failure locations. The real-time graphical representation visually identified deformation behavior, confirming the structural integrity and performance of the samples under compressive stress.

Figure 39: (a) EASYOUR compresion test machine , (b) upper and lower test plates

Chapter 4: Results and Discussion

4.1. Overview

the high number of variables interfering with the production activity in SLM requires a detailed framework to respect the highest quality while guaranteeing the lowest production time to increase productivity. This thesis aims to find a scheme covering both requirements; the State of Art suggested following a specific roadmap to achieve this objective. Indeed, the above-mentioned roadmap allowed to build small cubes, each one with a particular group of input parameters. The trial samples obtained following this procedure were analyzed to select the most promising set of process parameters that improve productivity. This chapter discusses the analysis performed during the experiments providing the results obtained by showing graphs and reporting numerical values. A large amount of data emerged from this process; thus, the main findings are directly presented in the following section.

The following paragraphs are structured as follows:

a) Analysis of Process Parameters on Density and Porosity – This section examines the effects of individual process parameters, their combined influence, and their impact on productivity.

b) Surface Quality Analysis – Discusses the effects of process parameters on surface roughness of the manufactured components.

c) Mechanical Testing – Evaluates the mechanical properties of samples obtained by compression test, balancing quality and productivity.

d) Cost Analysis – Assesses the economic feasibility of L-PBF-manufactured components, considering production costs and efficiency.

4.2. Analysis of density and porosity

This section highlights the results gained from the measurement methods outlined in the previous chapter. The main data that has been analyzed in this thesis includes measured relative density percentages obtained through three distinct methodologies (Archimedes density measurement, image analysis, and XCT).

All data acquired from the three density measurement methods has been compiled in this section. Table 5 presents the relative Archimedes density percentages measured for each of the 54 samples.

Table 5: Relative Archimedes density percentages measured for all 54 samples

Sample ID 40 Micron	Relative Archimedes Density [%]	Sample ID 60 Micron	Relative Archimedes Density [%]
1	99.1258	**1**	99.1093
2	99.0234	**2**	99.1346
3	99.1466	**3**	99.1308
4	98.9777	**4**	99.1284
5	99.2309	**5**	98.8125
6	99.1332	**6**	99.1304
7	98.7657	**7**	99.0713
8	99.0758	**8**	99.0895
9	99.0580	**9**	98.8450
10	98.7028	**10**	99.0909
11	98.7912	**11**	99.0925
12	98.8390	**12**	99.0267
13	98.9397	**13**	99.2587
14	99.1793	**14**	99.1022
15	98.9976	**15**	99.1110
16	99.1151	**16**	99.2107
17	99.2623	**17**	99.2345
18	99.0785	**18**	99.1581
19	98.3914	**19**	99.0638
20	98.5908	**20**	98.8770
21	98.6571	**21**	98.8468
22	99.1385	**22**	99.1128
23	99.2746	**23**	99.2707
24	99.0839	**24**	99.1685
25	99.2046	**25**	99.3184
26	99.2702	**26**	99.2676
27	99.1668	**27**	99.2779

Figure 40 also illustrate the results graphically.

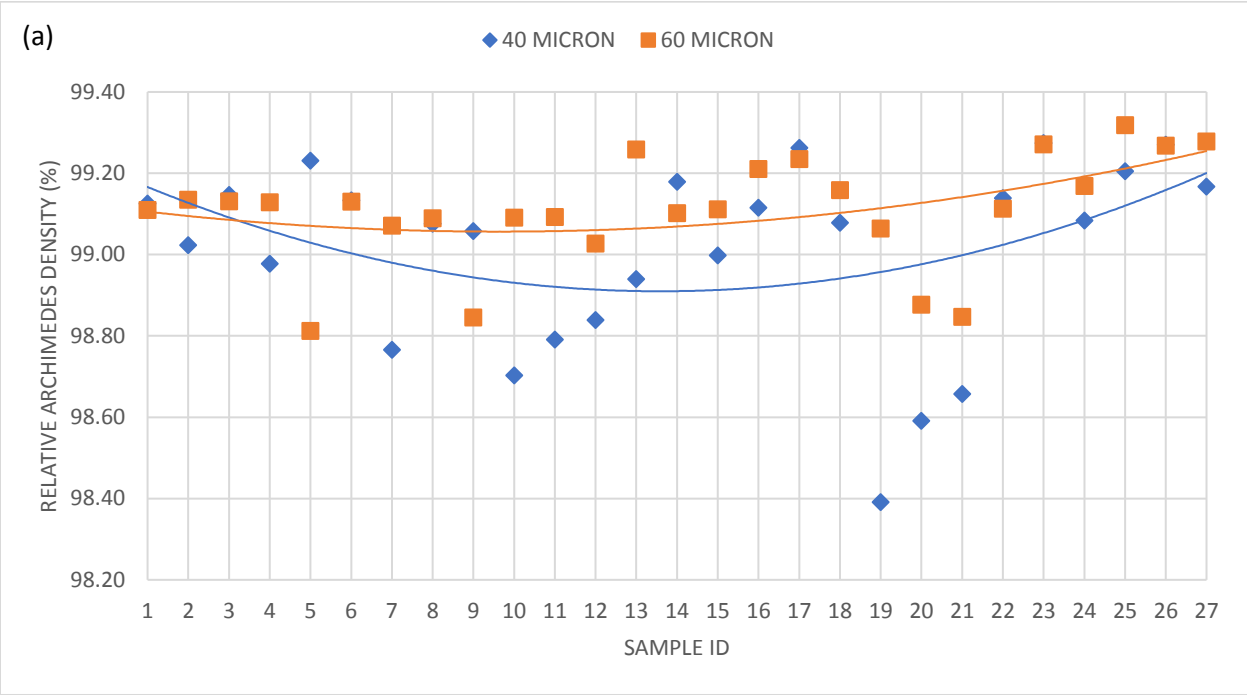

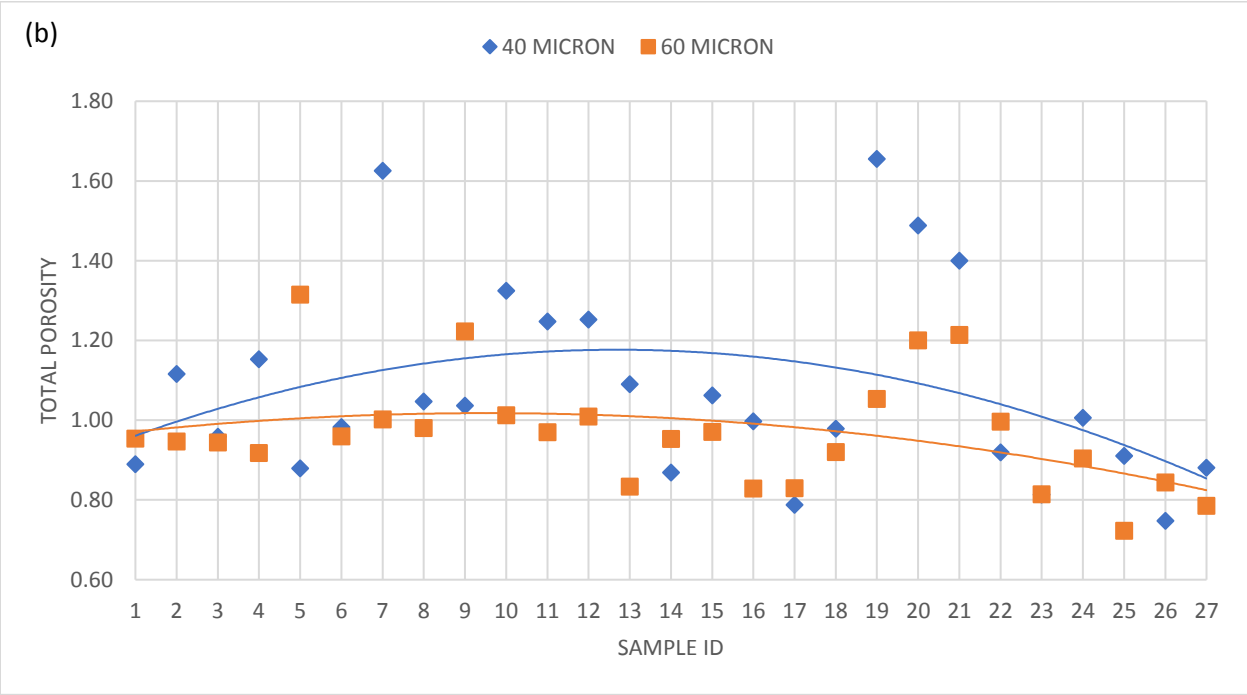

Figure 40: (a) Relative Archimedes density based on sample ID, (b) Total porosity based on sample ID

Most of the samples exhibit a relative Archimedes density above 98%, indicating a generally high level of densification. On average, samples with a 60-micron layer thickness achieve a higher relative Archimedes density compared to those with a 40-micron layer thickness, resulting in lower porosity. Among all samples, sample 19 with a 40-micron layer thickness has the lowest relative Archimedes density, while sample 25 with a 60-micron layer thickness has the highest.

To assess the influence of the predefined process parameters (Layer Thickness, Scan Speed, Laser Power, and Hatch Distance) on relative Archimedes density, an ANOVA statistical analysis was conducted using the data obtained from the tests. The results are presented in main effects plot (Figure 41) and Table 6.

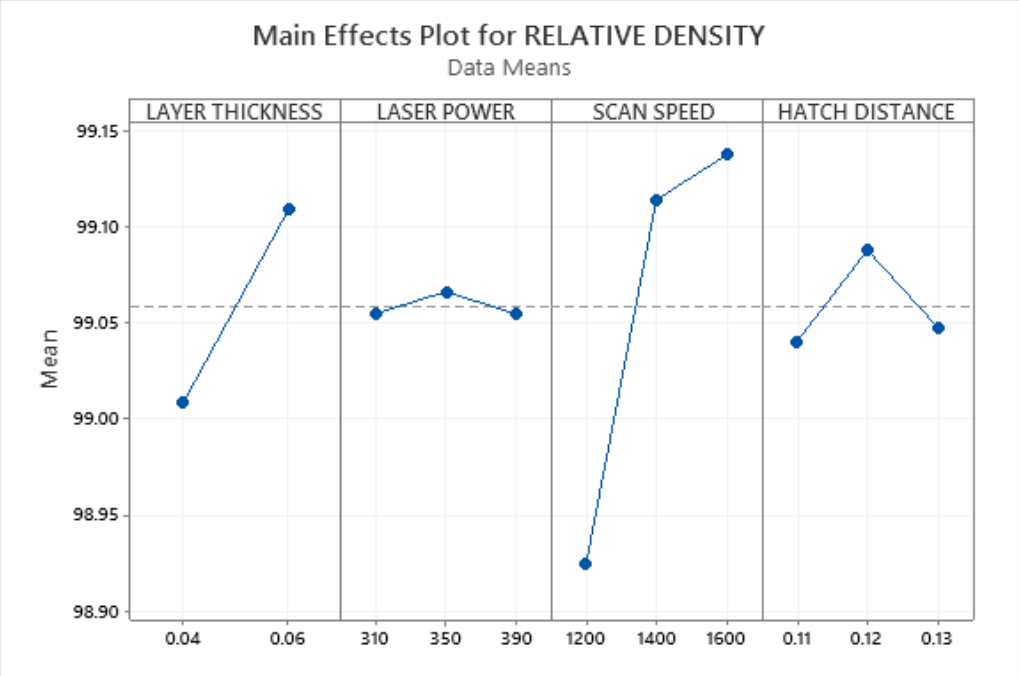

Figure 41: ANOVA statistical Analysis for relative density

The ANOVA results indicate the significance of factors influencing Relative Density. the p-value is a statistical measure that helps determine whether the differences between group means are statistically significant.

If $p \leq 0.05$, means process parameters significantly impact density while If $p > 0.05$, means no significant effect of parameters on density.

Table 6: significance of each parameter change on density change

Factor	P-value	Significance
Layer thickness	0.033	Significant
Laser power	0.973	Not Significant
Scan speed	0.001	Highly Significant
Hatch distance	0.664	Not Significant

Scan Speed is the most significant factor (p = 0.001), meaning it has the strongest impact. Layer Thickness is also significant (p = 0.033), so optimizing it improves Relative Density while Laser Power and Hatch Distance are not significant, meaning adjustments in these factors do not significantly impact Relative Density.

Furthermore, by analyzing the interaction plot obtained from the ANOVA analysis, we can observe the combined impact of all process parameters on relative density briefly. (Figure 42)

Figure 42: Interaction Plot of Process Parameters on Relative Density

The interaction plot reveals valuable information regarding the effect of process parameters on relative density. Layer thickness has a profound effect on density, with 0.06 mm yielding consistently higher values compared to 0.04 mm, particularly at high scan speeds. The highest improvement is realized by raising scan speed from 1200 to 1400 mm/s, and improvements diminish after 1600 mm/s. Laser power (310 W, 350 W, 390 W) shows insignificant interaction effects, which corroborates ANOVA findings that convey its insignificance. Hatch distance levels (0.11, 0.12, 0.13 mm) do not show a clear trend, but a shallow peak at 0.12 mm suggests it as an

optimum setting. These findings identify scan speed and layer thickness as the dominant influences on relative density.

In addition, densities in a chosen subset of samples were assessed through two other methods, as illustrated in the Table 7. Tomography and metallography results were derived through tomographic analysis and optical microscopy, with the latter being processed with "VG studio MAX" and "ImageJ" software. Porosity percentages internally were calculated from image analysis of tomographic information, providing thorough analysis of both surface and volumetric properties. The use of improved imaging resolution methods and computerized programs enabled more precise porosity assessment, enhancing the quality and reliability of the data.

Table 7: Porosity percentages for selected samples using two additional methods (XCT and metallography).

Sample ID	Porosity content by XCT [%]	Porosity content by image analysis [%]	Porosity content by Archimedes Density analysis [%]
40 Micron -No.7	0.27	1.35	1.63
40 Micron -No.9	0.2	0.80	1.04
40 Micron -No.19	1.56	1.19	1.66
40 Micron -No.23	0.38	1.20	0.81
40 Micron -No.27	0.43	0.99	0.88
60 Micron -No.7	0.7	0.45	1.0
60 Micron -No.9	1.64	1.22	1.22
60 Micron -No.19	0.63	1.08	1.05
60 Micron -No.23	0.3	0.68	0.81
60 Micron -No.27	0.53	0.51	0.79

Based on the Figure 43 results are almost same for different measurement techniques. in some samples the difference between tomography and metallography results can be attributed to the fact that metallography mainly investigates the surface. One sample may exhibit significant porosity at the surface, whereas the bulk displays reduced porosity. This highlights the differences between these measurement techniques.

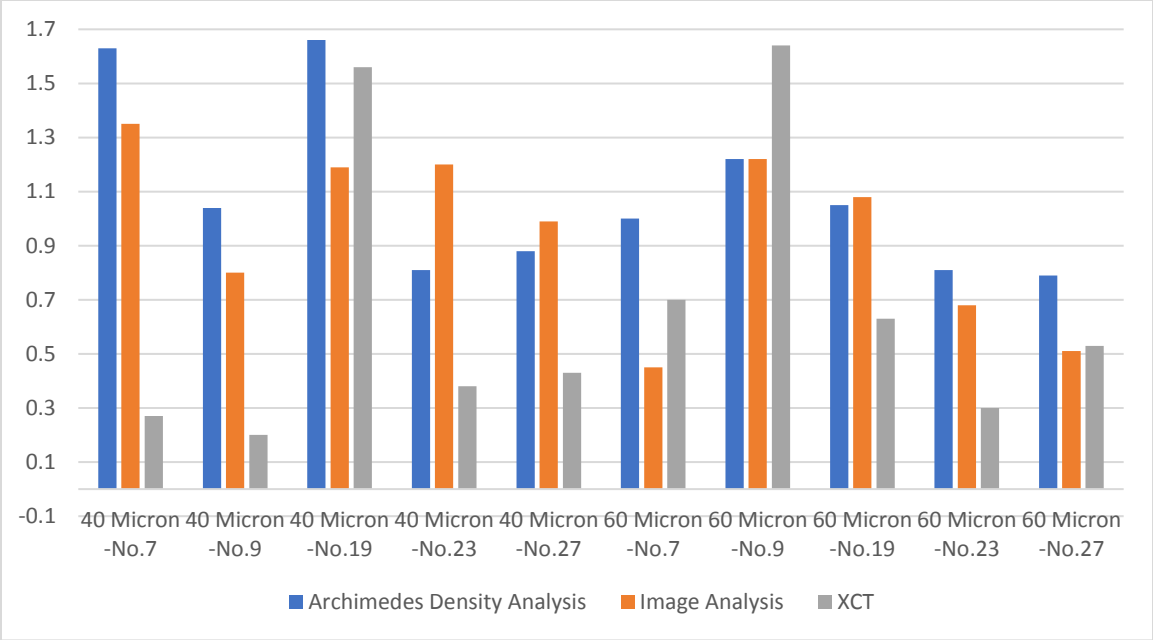

Figure 43: Porosity percentage chart displaying values obtained from different techniques

The analysis concentrated exclusively on the Archimedes method applied to all 54 samples. The purpose of this analysis was to determine the closeness of the data using the Archimedes method to achieve a precise comprehension of its accuracy.

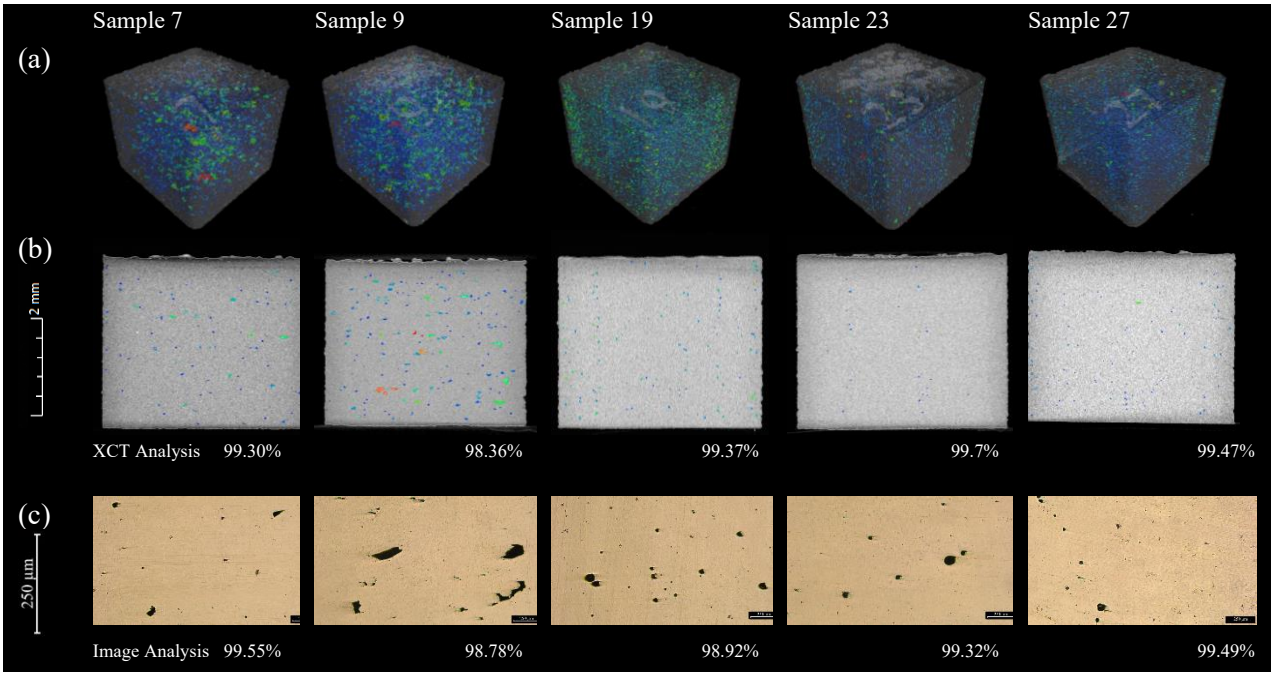

Figure 44: Representation of a thorough analysis of the samples employing various density measurement techniques. (a) presents the 3D tomography, providing a comprehensive visualization of the sample structure, with each sample measuring 12 × 12 × 10 mm. (b) emphasizes the frontal perspective of the samples, displaying internal characteristics via tomography imaging. (c) presents metallographic images acquired through OM, comprehensively analyzing the sample's structure. Furthermore, the density values of the samples, obtained through XCT and image analysis techniques, are presented for comparison.

From the Figure 45, we can infer insights regarding the porosity characteristics of AlSi10Mg samples. The correlation coefficient between Porosity Percentage and Maximum Pore Diameter is 0.041, which is very close to zero.

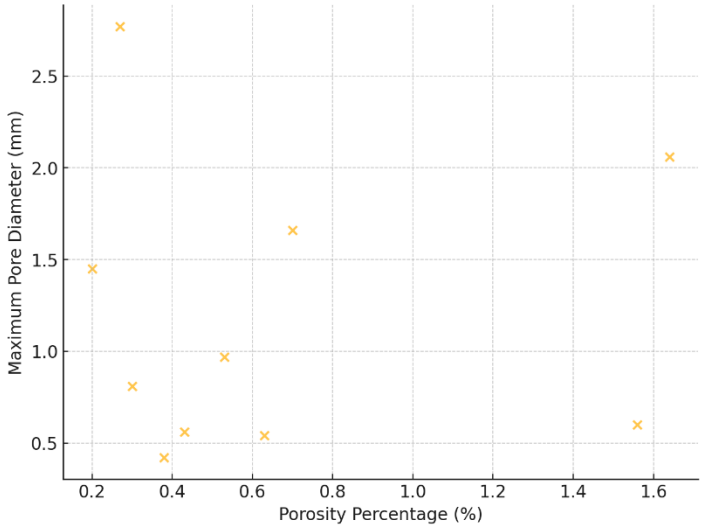

Figure 45: Scatter Plot Of Porosity Percentage Vs. Maximum Pore Diameter

This suggests that there is no significant linear correlation between the porosity percentage and the maximum pore diameter in the dataset. In other words, an increase in porosity percentage does not necessarily correspond to a predictable increase or decrease in the maximum pore diameter.

Based on Figure 46, the correlation analysis of process parameters on maximum pore diameter in samples revealed that laser power and scan speed are the most influential factors. A strong negative correlation (-0.88) was found between laser power and maximum pore diameter, indicating that higher laser power significantly reduces pore size by improving material fusion and minimizing defect formation. Conversely, scan speed showed a moderate positive correlation (+0.61) with maximum pore diameter, meaning that higher scan speeds lead to larger pores, likely due to insufficient energy input causing incomplete melting and lack-of-fusion defects.

Other process parameters had minimal impact on maximum pore diameter. Hatch distance (-0.08 correlation) and layer thickness (+0.03 correlation) showed no significant influence, suggesting that their effect on porosity might be more related to pore distribution rather than individual pore size.

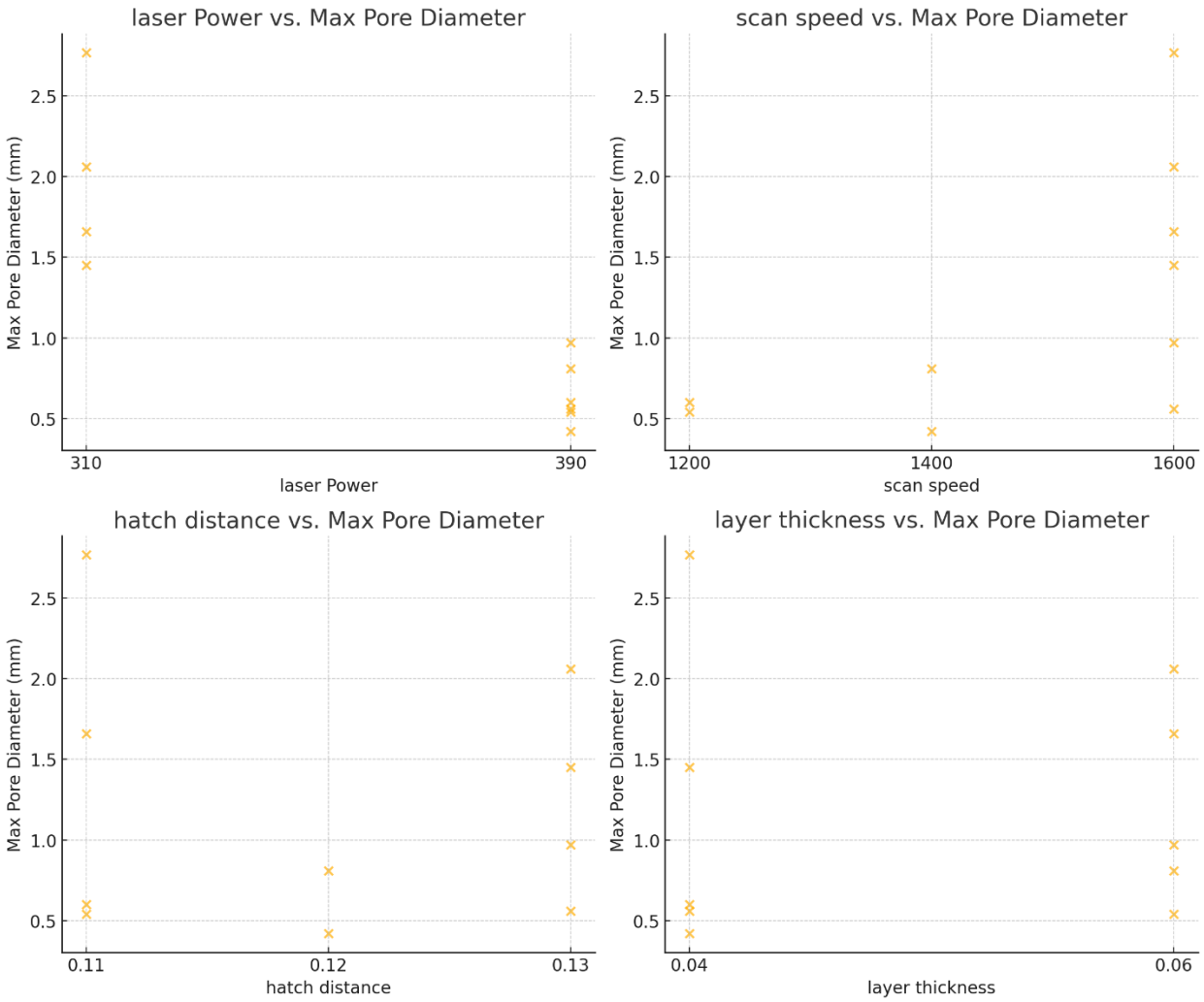

Figure 46: Scatter plots of the relationships between Maximum Pore Diameter and key process parameters

In conclusion, laser power and scan speed should be the primary focus for reducing maximum pore diameter, with higher power and moderate scan speed yielding the best results. Other parameters, such as hatch distance, layer thickness, have negligible direct effects on maximum pore size.

To assess the influence of the predefined process parameters (Layer Thickness, Scan Speed, Laser Power, and Hatch Distance) on maximum pore diameter, an ANOVA statistical analysis was conducted using the data obtained from the tests. The results are presented in main effects plot (Figure 47) that confirm previous analysis.

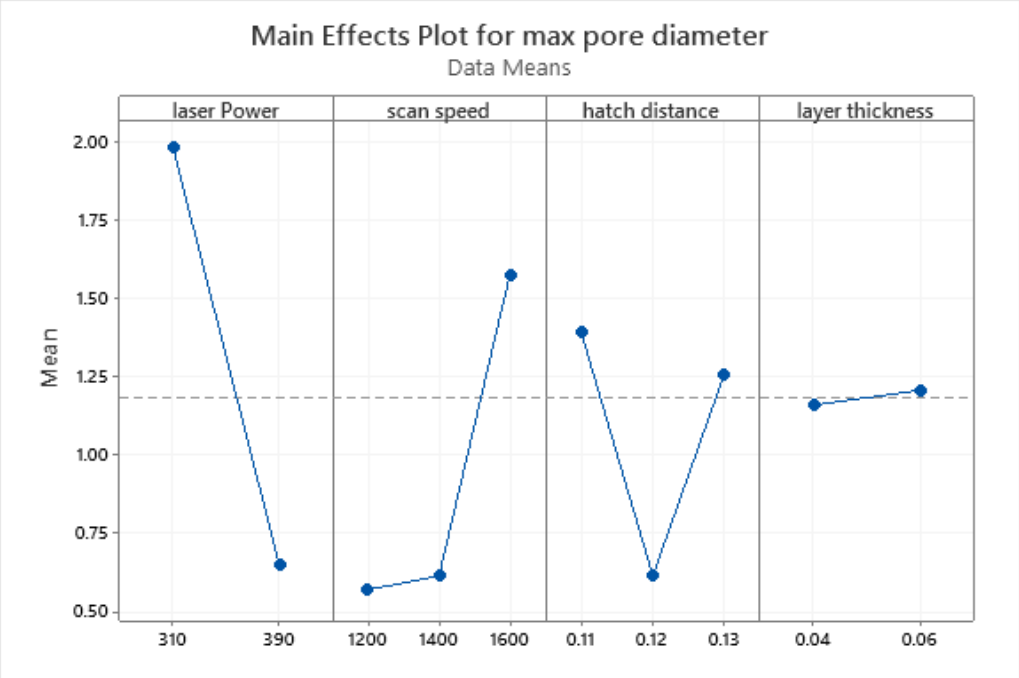

Figure 47: ANOVA statistical analysis for maximum pore diameter

4.2.1 The relationship between volumetric energy density and relative density

This part of the study analyzes the density results by the combined effect of the process parameters that alter, which is referred to as volumetric energy density. It is known from literature that a sufficiently high value of VED enhances the correct densification of the produced parts. High VED process more material in every unit volume, and therefore the correct consolidation leads to compacted products while more energy input leads to excessive vaporization, forming deep keyholes that collapse and trap pores leads to low densities.

Therefore, both extremely low and extremely high values of VED are inappropriate generally for creating a totally dense component. So, As the VED changes, different types of porosities can be observed. Figure 44 illustrates the achieved densities with the increasing values of VED.

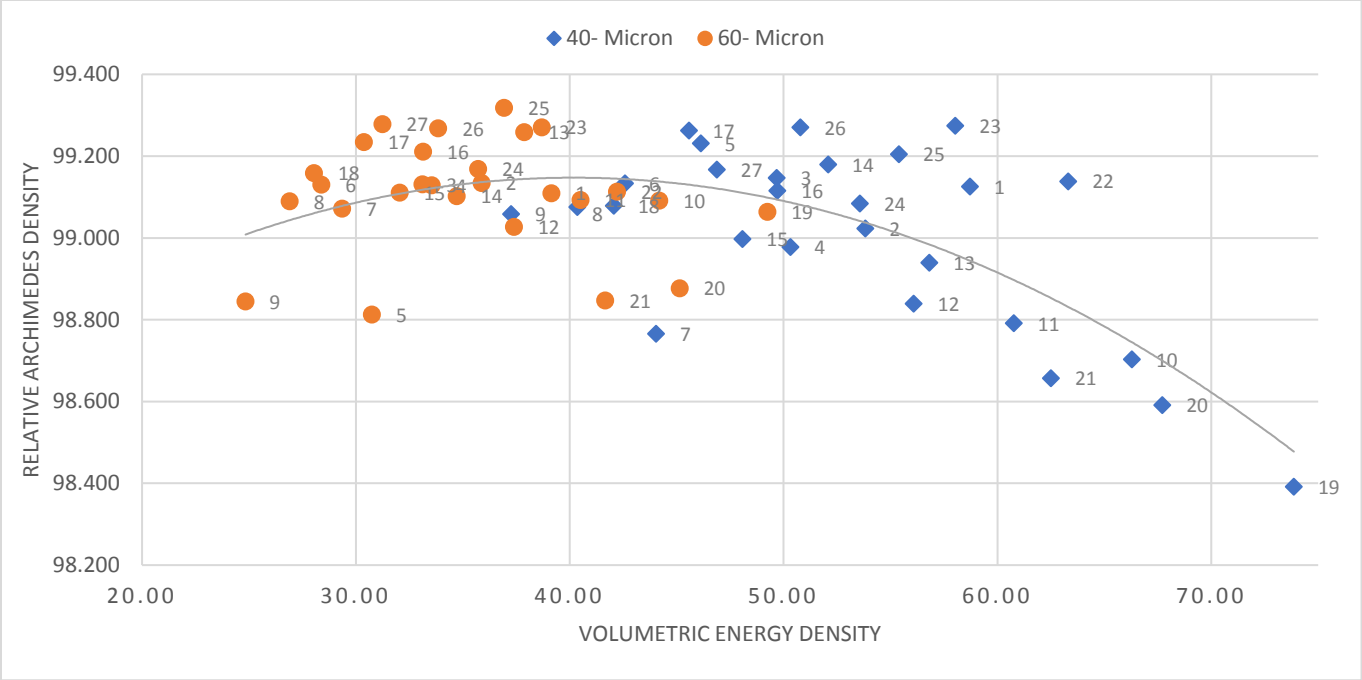

Figure 48: The relationship between volumetric energy density and relative archimedes density

The relative density values increase with increasing VED until reaching an almost steady region where density remains constant as VED increases and then starts to decrease. The relative density as a function of VED has been approximated with a second order polynomial. In this study, the printed material had its maximum density at a VED of 36.93 J/mm; and its lowest density at a VED of 73.86 J/mm.

Samples with 60-micron layer thickness achieve a higher peak density in the optimal range (35-45 J/mm³), suggesting that they allow better densification under optimized conditions. The trendline peaks in this range, reinforcing that this is the optimal VED range for achieving the highest material density. Beyond around 40 J/mm³, the density drops, and this suggests keyhole porosity and excessive vaporization effects impacting material integrity.

The decline is more noticeable at higher VED values beyond 50 J/mm³, where samples suffer from defects. Samples with 40 µm layer thickness seem to scatter more widely and show greater variability and may be more sensitive to process deviations.

Furthermore, samples produced with similar VEDs in some cases have similar relative densities. For example, sample 6 with 40 µm layer thickness has almost same relative density as sample 22 with 60 µm layer thickness equal to 99.13% and 99.11% respectively. These results indicate that the same density can be achieved by combining different process parameters, given that the VED obtained is similar. Figures 45 display the surface features for samples printed with similar VEDs in 1x and 5x.

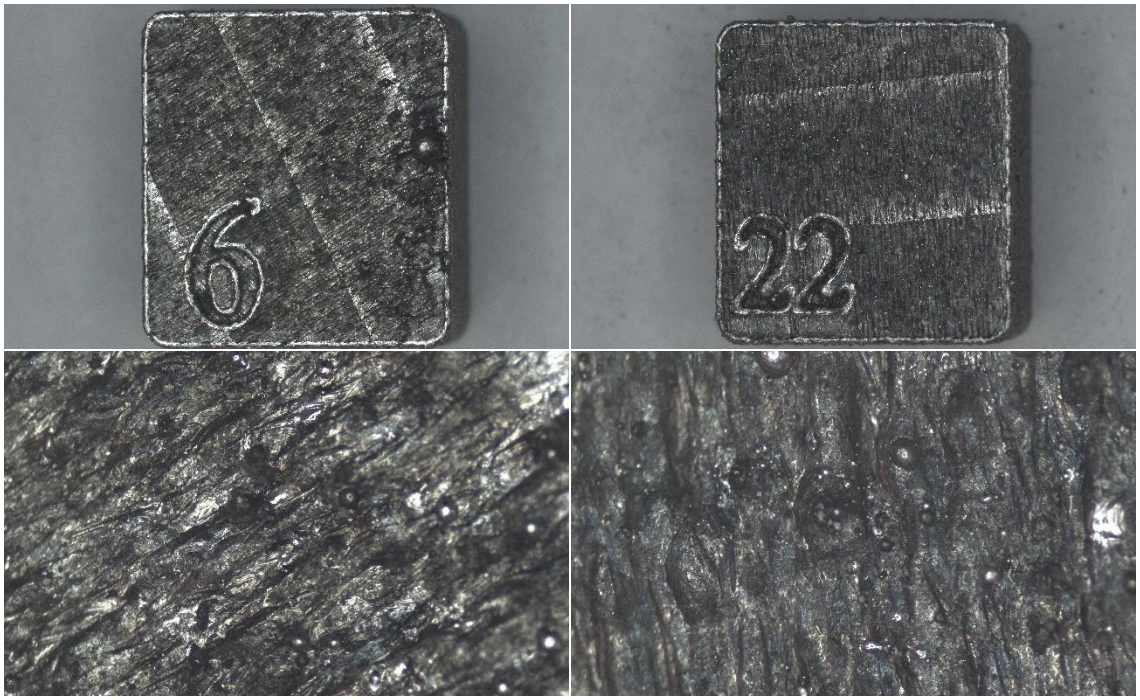

Figure 49: Different magnifications of surface features of samples 6 (40-micron) and 22 (60-micron)

Scan speed as a process parameter with high influence on relative density here again analyzed in figure considering the VED. Also, the same graph with laser power as a process parameter not having significant effect on relative density is depicted in Figure 46. where the bubble size is in proportion to the scan speed and laser power respectively.

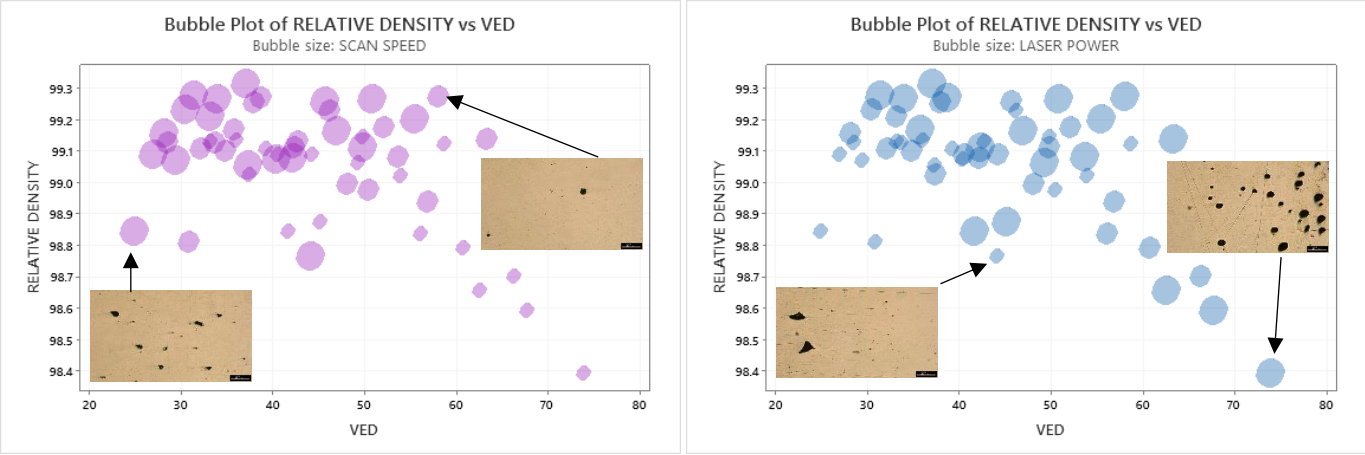

Figure 50: Illustration of the relationship between the calculated Volumetric Energy Density (VED) and the relative Archimedes density. The size of the points represents (a) scan speed, and (b) laser power.

that are lower, particularly for larger values of VED, and what this indicates is that excessive energy input at reduced scan speeds induces keyhole porosity. When compared to this, in second

plot, there seems to be no trend, indicating that laser power does not have a significant influence on relative density. The spreading of bubbles on this plot proves that alterations in laser power individually do not contribute to changes in densities. These results highlight the importance of scan speed in determining relative density, with laser power apparently irrelevant to relative density trends. Therefore, achieving optimal densification involves an accurate compromise between scan speed and VED to prevent porosity and stable processing conditions.

4.2.2 The relationship between volumetric energy density and porosity

Part density is predominantly governed by pore formation, which is usually in two modes: insufficient volumetric energy density (VED) leads to lack of fusion defects and excessive VED leads to keyhole-induced porosity. The Figure 47 illustrates the pore percent evolution as a function of increasing supplied energy to the powder.

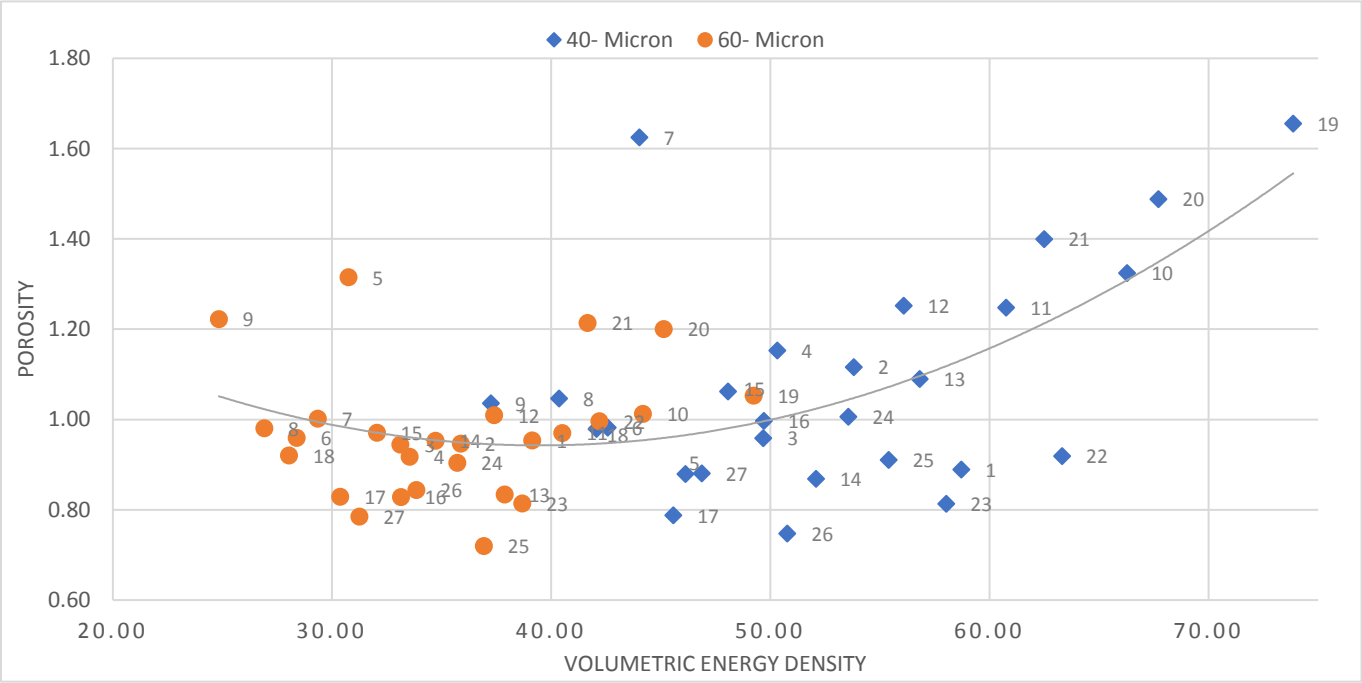

Figure 51: The relationship between volumetric energy density and porosity

Porosity goes on decreasing with increasing VED until, beyond a point, it begins to rise again. Pore fraction has been approximated with a second order polynomial. Samples with 40-micron layer thickness containing a higher average volumetric energy density show a greater percentage of porosity compared to samples with 60-micron layer thickness.

4.2.3 The relationship between productivity and relative density/porosity

The high cost per part is an intrinsic problem associated with L-PBF, and this is contributed to a great extent by the plentiful build time involved. Figure 48 shows plot depicting the influence of build rate on density. Productivity has been computed, considering only the scanning time, for the process parameters used in this study.

In each series of samples, nine groups of three samples share the same build rate. The plotted trend line represents the average of the three volumetric energy density values corresponding to a specific build rate. Blue dots are representative of samples with 40-micron layer thickness and orange dots of 60-micron. From the point distribution, Samples with 40-micron layer thickness appear to have a wider distribution of density values, with lower density values at lower build rate. Samples with 60-micron layer thickness appear to have higher average density at higher build rates. The trend is that the density increases with build rate, peaks, and then drops slightly.

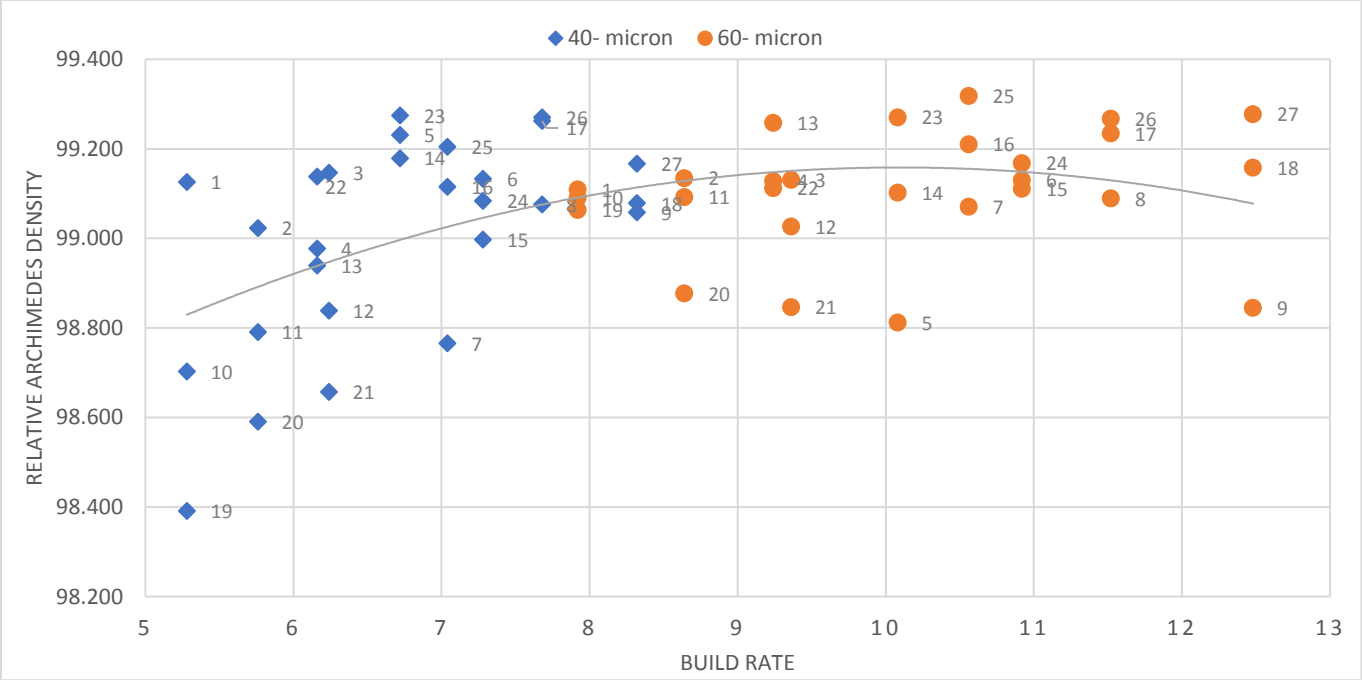

Figure 52: The relationship between build rate and realtive density

Focusing more on the graph we can gain some important information. for example, considering sample number 5 and 23 with 60-micron layer thickness knowing that they are also have same scan speed of 1400 mm/s and hatch distance of 0.11 mm, the reason of the difference between their relative Archimedes density while having same build rate is the laser power difference which is 310 W for sample 5 and 390 W for sample 23. Increasing laser power in this case increased the density.

However, considering for example samples 6, 15 and 24 sharing same layer thickness of 60-micron when they also have same scan speed of 1400 mm/s and hatch distance of 0.12 mm, increasing laser power in this case did not lead to increase in relative density too much. So having higher hatch distance in this set of samples, laser power did not play an important role in changing relative Archimedes density of samples.

For sample 23 with a 40-micron layer thickness and sample 27 with a 60-micron layer thickness, the build rate increased from 6.72 mm^3/s to 12.48 mm^3/s while maintaining nearly the same Archimedes relative density. This demonstrates that by selecting appropriate process parameters, it is possible to achieve higher build rates without compromising quality. The Table 8 presents the process parameters used for these two samples.

Table 8: Process parameters for two samples with same relative denisty

SAMPLE ID	LASER POWER [W]	SCAN SPEED [mm/s]	HATCH DISTANCE [mm]	LAYER THICKNESS [mm]	VED [j/mm³]	BUILD RATE [mm³/s]	RELATIVE DENSITY [%]
23	390	1400	0.12	0.04	58.0	6.72	99.275
27	390	1600	0.13	0.06	31.3	12.48	99.278

Figure 49 show plot depicting the influence of build rate on porosity. like before the plotted trend line represents the average of the three volumetric energy density values corresponding to a specific build rate.

The results highlight the necessity for adjusting the process window so that fabrication speed is sped up and therefore cut costs. Nevertheless, this specification must be negotiated in accordance with the final part quality was needed. In fact, the ideal build rate selection is subject to the requirement for avoiding the generation of lack of fusion porosity in the finished piece. Such various constraints required productivity and required quality set up the acceptable limit of process parameters functional to drive the process.

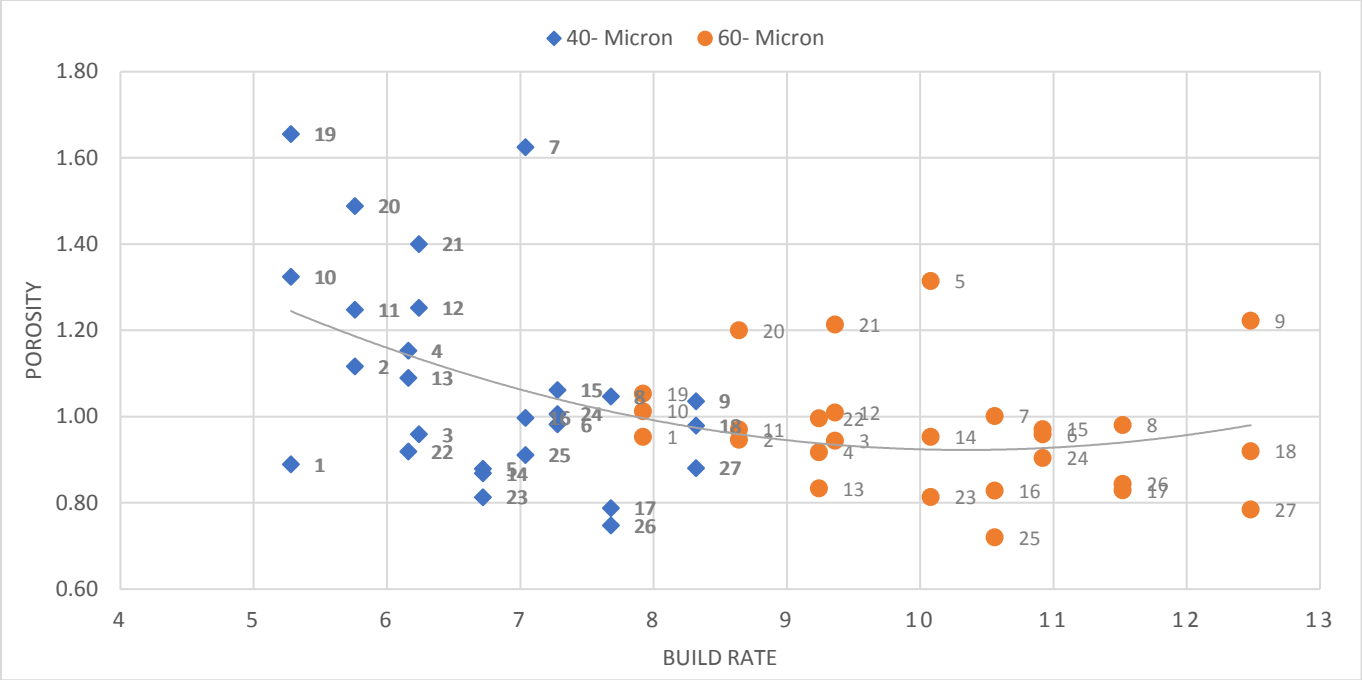

Figure 53: The relationship between build rate and porosity

4.3. Analysis of the surface quality

This part of the work is dedicated to grading the quality status of the test samples based on surface roughness analysis. It contains the main results obtained during the test, and it provides discussion on the impact of a more productive set of parameters on the surface quality.

4.3.1. Surface roughness

The surface roughness of the samples was measured with a profilometer. The instrument utilized took R_a and R_z measurements in units of µm by drawing its probe in a straight line along the surface of a sample. Roughness readings were taken in three portions of top face of cubes then an average value computed and reported.

R_a (Arithmetic Mean Roughness) represents the average roughness of a surface and is calculated as the arithmetic mean of the absolute deviations of the surface profile from the mean line over a given length.

R_z (Ten-Point Average Roughness) measures the average height difference between the five highest peaks and five deepest valleys within a sample length.

In other words, R_a is a general average of surface roughness and is less sensitive to extreme peaks and valleys while, R_z highlights peak-to-valley variations, making it more useful for applications where surface peaks or valleys significantly impact performance.

Figure 50 represents the arithmetic mean roughness for each sample. The measured data indicate that a minimum value of top surface roughness (R_a = 3.04 µm) characterizes sample 20 with 40-micron layer thickness and the maximum value of top surface roughness (R_a = 17.65 µm) was seen in cube number 9 with 60-micron layer thickness.

The corresponding values of process parameters represented in Table 9. The roughness profiles for the top faces of these samples are presented in Figure 51.

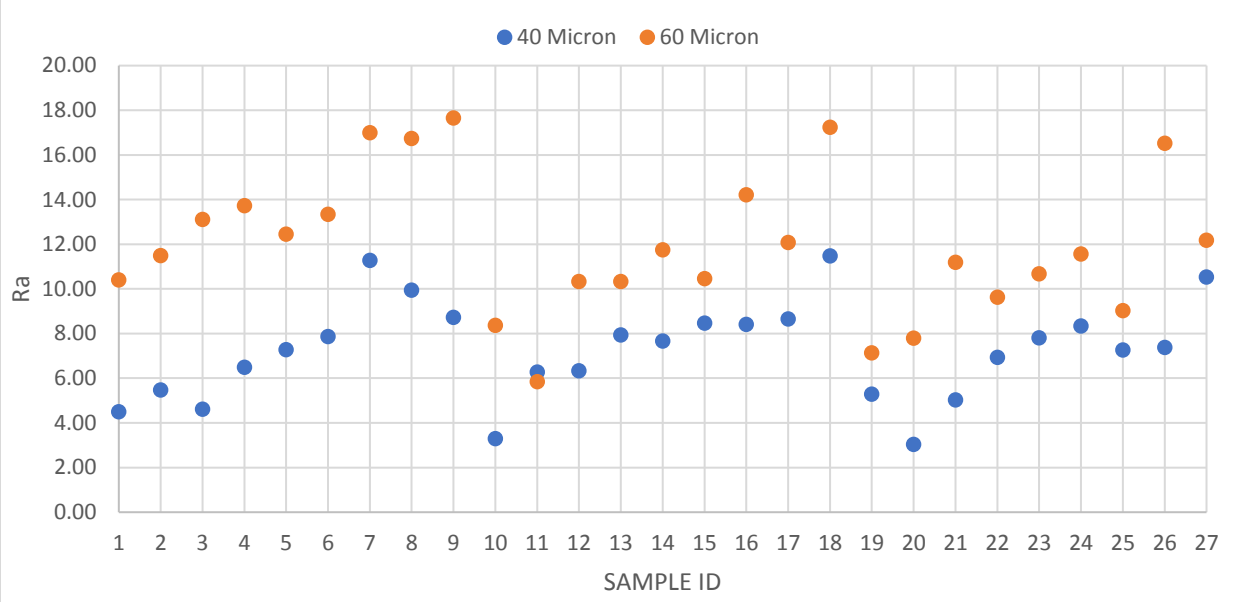

Figure 54: Arithmetic Mean Roughness

Table 9: Process parameters for samples 20 and 9

SAMPLE ID	LASER POWER [W]	SCAN SPEED [mm/s]	HATCH DISTANCE [mm]	LAYER THICKNESS [mm]	VED [j/mm³]	BUILD RATE [mm³/s]	MEAN ROUGHNESS [µm]
20	390	1200	0.11	0.04	67.7	5.76	3,04
9	310	1600	0.13	0.06	24.8	12.48	17,65

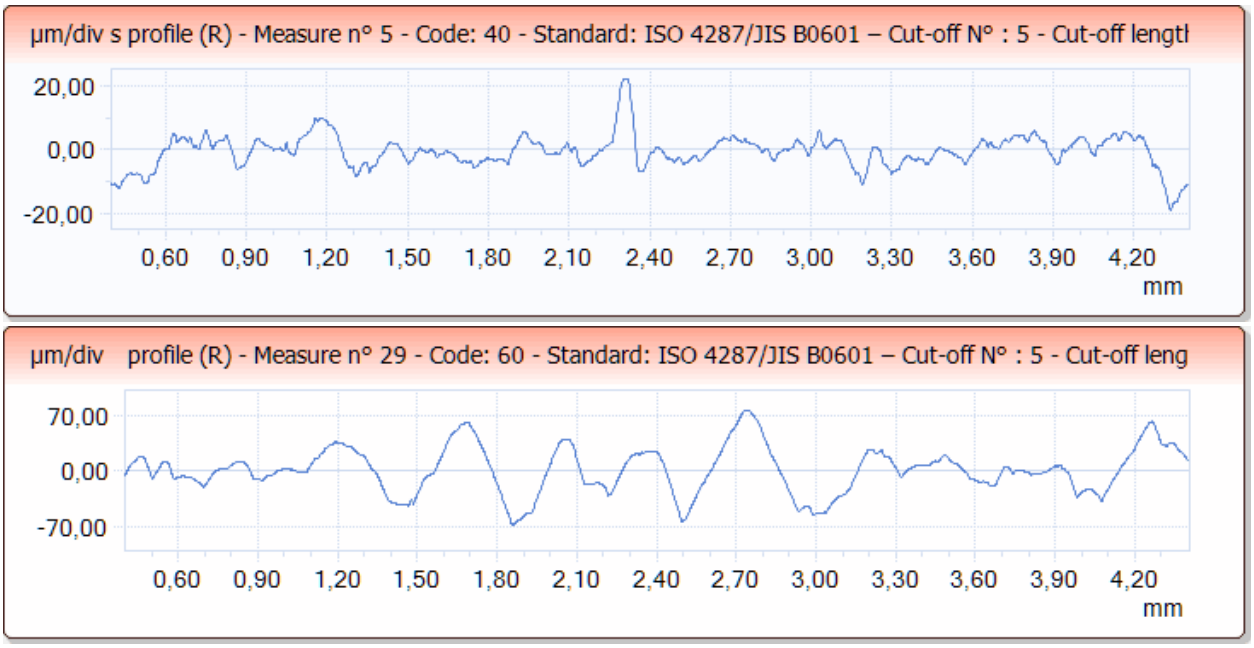

Figure 55: The roughness profiles for the top faces of samples 20 (up) and 9 (down)

Based on roughness profiles, sample 9 exhibits a more pronounced peak-to-valley variation compared to Sample 20, indicating a rougher surface. The fluctuations in Sample 9's profile appear more intense and irregular, which aligns with its higher measured mean roughness. Sample 20 has a smoother, more consistent profile, with fewer extreme peaks and valleys, correlating with its much lower mean roughness.

This is also obvious in images taken from the surface of the samples with stereo microscope with 5x magnification as represented in Figure 52.

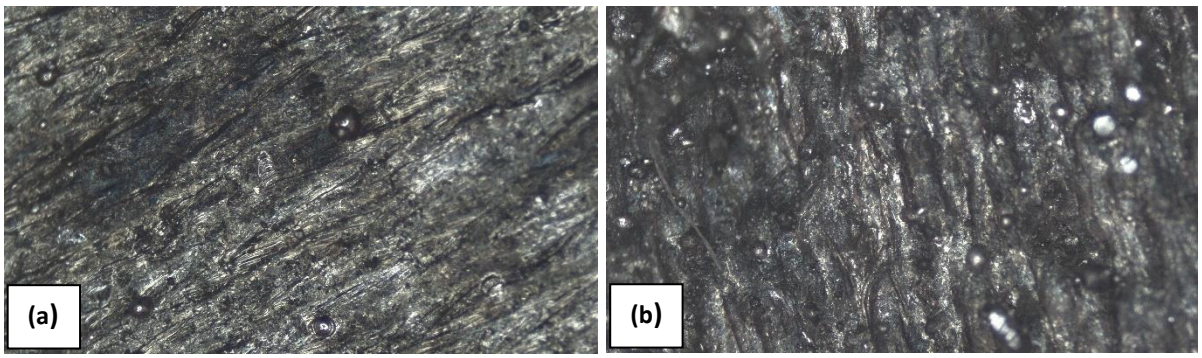

Figure 56: stereo microscope images from the surfaces of (a) sample 20, (b) sample 9

To assess the influence of the predefined process parameters (Layer Thickness, Scan Speed, Laser Power, and Hatch Distance) on surface roughness, an ANOVA statistical analysis was conducted using the data obtained from the tests. The results are presented in Figure 53 and Table 10.

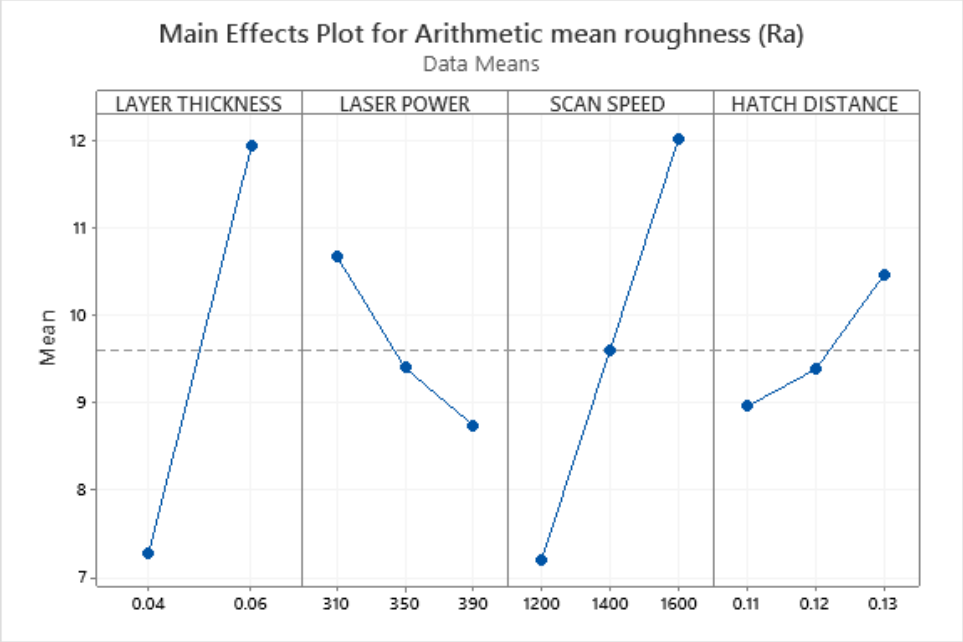

Figure 57: ANOVA statistical analysis

The ANOVA results indicate the significance of factors influencing Relative Density. the p-value is a statistical measure that helps determine whether the differences between group means are statistically significant.

If $p \leq 0.05$, means process parameters significantly impact density while If $p > 0.05$, means no significant effect of parameters on density.

Table 10: significance of each parameter change on density change

Factor	P-value	Significance
Layer thickness	0.000	Highly Significant
Laser power	0.002	Significant
Scan speed	0.000	Highly Significant
Hatch distance	0.019	Significant

Layer thickness and scan speed are the most significant factors ($p = 0.000$), meaning they have the strongest impact. Laser power is also significant ($p = 0.002$), so optimizing it improves surface roughness while hatch distance is the least significant factor ($p = 0.019$).

Furthermore, by analyzing the interaction plot obtained from the ANOVA analysis, we can observe the combined impact of all process parameters on relative density briefly. (Figure 54)

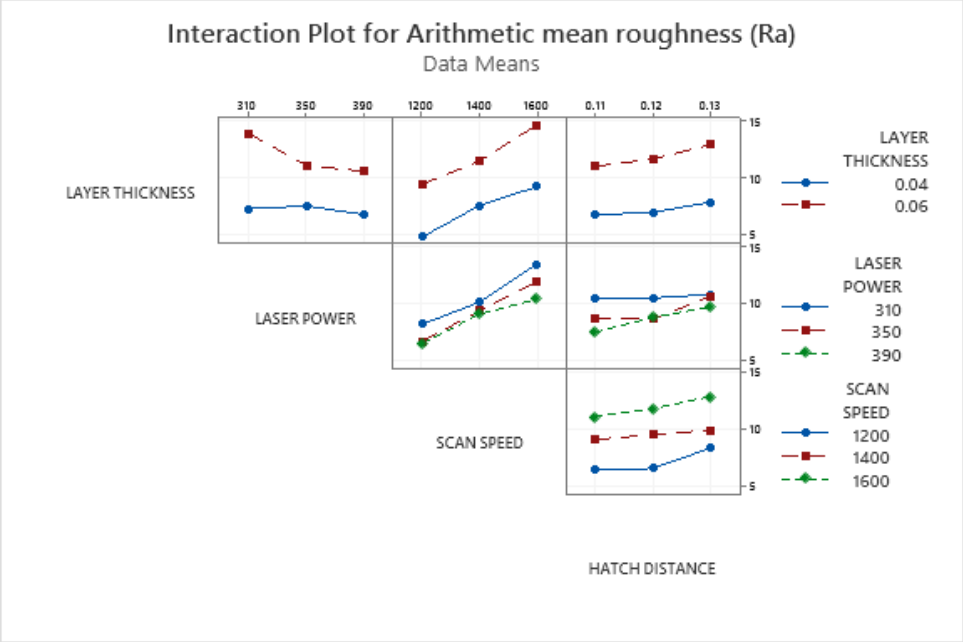

Figure 58: Interaction Plot of Process Parameters on surface roughness

The plot of interaction indicates that surface roughness (Ra) increases with greater layer thickness, lower laser power, higher scan speed, and higher hatch distance. Higher layers (0.06 mm) produce a rougher surface than thin layers (0.04 mm) due to instability of the melt pool. Lower laser power (310 W) increases roughness, while higher power (390 W) increases the smoothness of the surface by attaining better layer fusion. Higher scan speed (1600 mm/s) results in higher roughness as a result of lower energy input per unit area, leading to incomplete melting. Higher hatch distances (0.13 mm) also deteriorate roughness by reducing track overlap.

Interactions show that higher power can lower roughness at high scan speeds, while higher hatch distances with fast scanning produce the roughest surfaces. In order to create a more uniform surface, better parameters include lesser layer thickness, greater laser power, lower scanning speed, and a lessening hatch distance.

Figure 55 represents the Ten-Point Average Roughness for each sample. The measured data indicate that a minimum value of top surface roughness (R_z = 17.46 µm) characterizes sample 20 with 40-micron layer thickness and the maximum value of top surface roughness (R_z = 85.54 µm) was seen in cube number 9 with 60-micron layer thickness just like R_a.

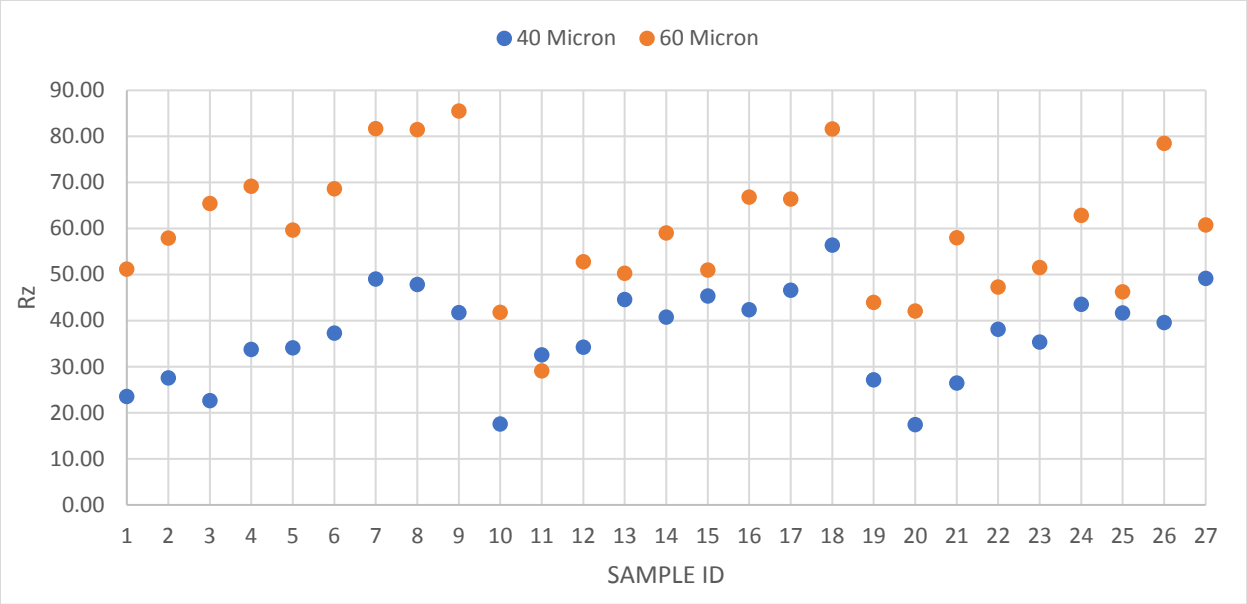

Figure 59: Ten-Point Average Roughness

4.3.2. The relationship between VED and surface roughness

In this section, the mean roughness values (R_a) are taken as a reference to investigate the influence of VED on the parts surface quality. Figure 56 shows the relationship between VED and surface roughness.

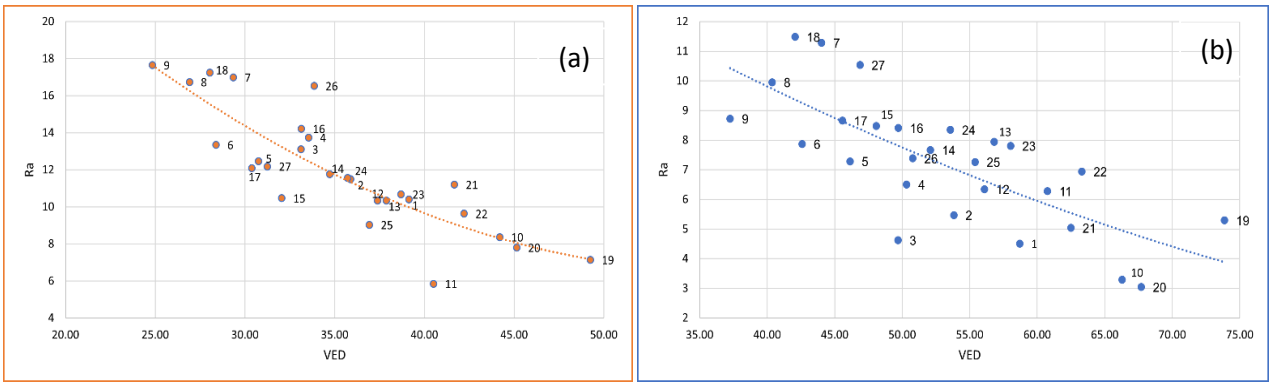

Figure 60: Influence of VED on Surface roughness of samples with (a) 60-micron, (b) 40-micron layer thickness

For both 40-micron and 60-micron layer thicknesses, surface roughness (R_a) decreases with an increase in volumetric energy density (VED). This indicates that higher energy input improves the surface quality by promoting better melt pool formation and reducing surface defects.

The 60-micron layer thickness plot (a) shows far greater Ra values than the 40-micron plot (b) for the same VED ranges. This is because thicker layers create more surface irregularities from higher melt pool instability, incomplete fusion, or balling effects (Figure 57).

The R_a reduction is more pronounced in the 60-micron case, which means that higher VED is more critical for thicker layers to reduce roughness. This could be due to higher energy required to melt and bond fully thicker layers. In both these graphs, R_a reduction slows down with increasing values of VED, showing a diminishing return effect. This shows that for energy values above some threshold VED, increasing energy further does not increase surface quality significantly and can result in defects like over-melting or keyhole formation.

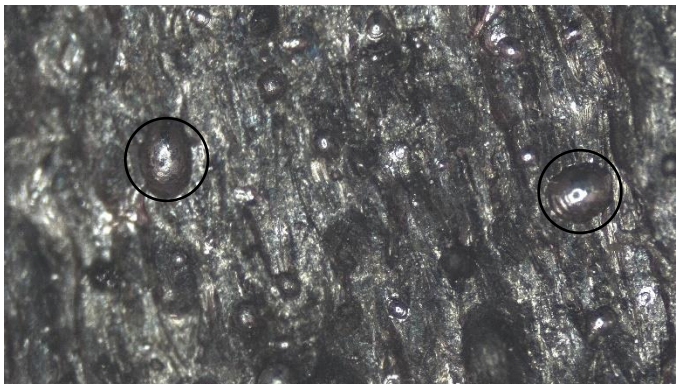

Figure 61: Balling effect on surface

4.3.3. The relationship between build rate and surface roughness

In this section, the mean roughness values (R_a) are taken as a reference to investigate the influence of build rate on the parts' surface quality. Figure 58 illustrates the effects that build rate have on the final surface quality.

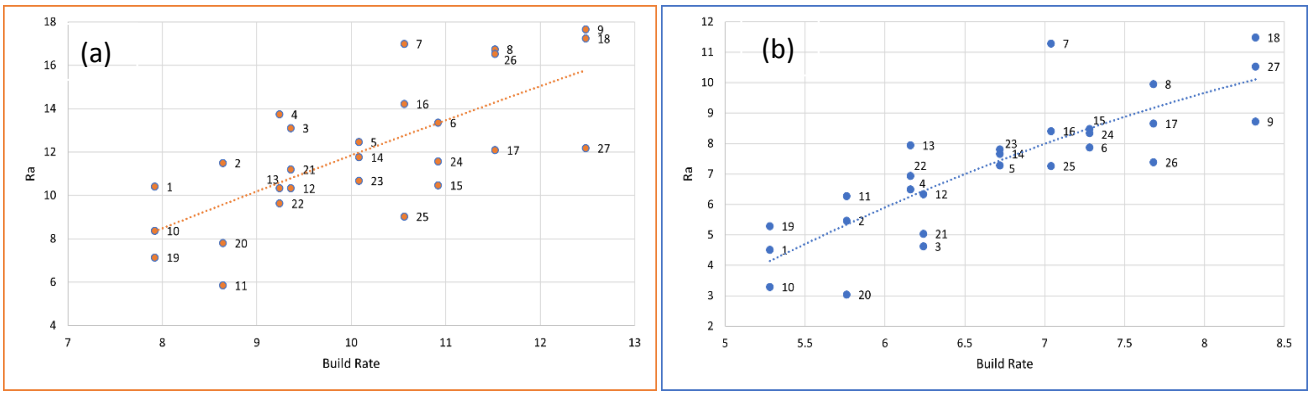

Figure 62: Influence of build rate on Surface roughness of samples with (a) 60-micron, (b) 40-micron layer thickness

Referring to the Figure 58, the build rate increases, and the surface roughness (R_a) also increases in both layer thickness cases (40 μm and 60 μm). This suggests that increased production leads to increased surface roughness, which may be due to reduced energy input per volume, partial melting, and increased surface defects.

The slope of the trend line is steeper for 60-micron layers, showing that surface roughness deteriorates more rapidly with increased build rates compared to 40-micron layers. Therefore, thicker layers are worse off with increased build rates as far as roughness is concerned.

4.4. Mechanical characteristics analysis

The final stage of testing the quality of parts produced was mechanical testing, in which compression testing of some samples was conducted. The results obtained were compared for examining mechanical properties. It is beneficial for evaluating the influence of process parameters on the structural characteristics and performance of the produced components

4.4.1 Compression test

The samples were tested for their stress-strain response by carrying out a compression test. The compression test was performed with the help of a specially designed compression testing machine, and cubic samples were subjected to uniaxial loading.

The compressive force was recorded as a function of deformation of cubes. Compressive stress-strain curves were plotted based on data collected from the machine. Compressive stress (σ) is defined as a compressive load applied divided by the cross-sectional area of the cube:

$$\sigma = \frac{F}{A_0} \ [MPa] \tag{19}$$

Strain (ε) represents the relative deformation of the cube under compression and is calculated as:

$$\varepsilon = \frac{l - l_0}{l_0} \ [mm/mm] \tag{20}$$

where l_0 is the initial cube height, and l is the height after load application.

The compression properties obtained, including yield strength (YS), ultimate compressive strength (UCS), and strain at failure (ε_f). They are compared with the literature data to ensure consistency

and reliability. Figure 63 demonstrates the true stress-strain curves and Table 11 shows related data.

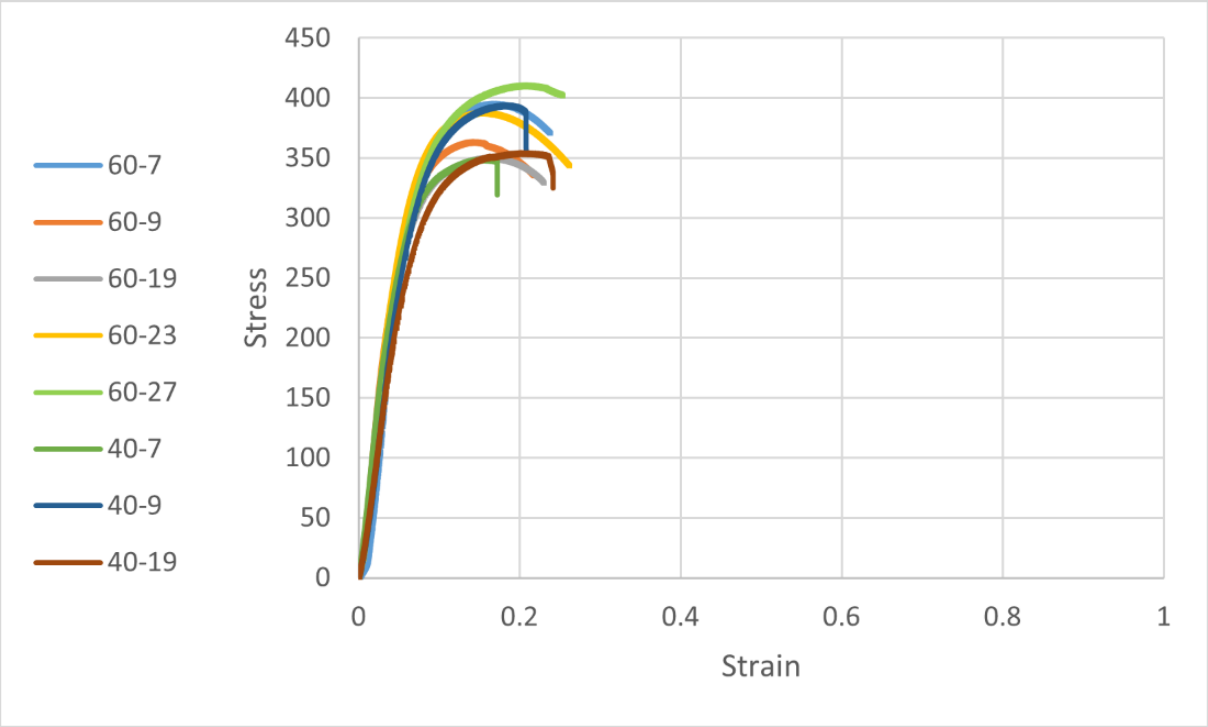

Figure 63: True Stress-strain curves for compression test

Table 11: Summary of True Compressive Properties of Samples

Sample ID	Layer Thickness (µm)	UCS (MPa)	Yield Strength (MPa)	Strain at Failure
7	40	390	330	0.23
9	40	370	320	0.21
19	40	350	310	0.22
7	60	400	330	0.22
9	60	360	310	0.19
19	60	340	300	0.18
23	60	370	310	0.21
27	60	420	340	0.25

The true stress–strain curves obtained from compression testing of AlSi10Mg samples exhibit distinct mechanical responses based on layer thickness. Samples produced with 40 µm layers

relatively consistent behavior, reaching peak true stresses between 350–390 MPa. These samples also show a pronounced and sudden stress drop immediately after the peak, indicative of localized deformation mechanisms such as shear banding or strain softening, possibly triggered by residual stresses or microstructural discontinuities introduced during the layer-by-layer build process. In contrast, the 60 µm samples display a wider range of peak stresses (340–420 MPa), with sample number 27 achieving the highest strength overall (~420 MPa). These thicker-layer samples generally exhibit more gradual post-peak behavior, suggesting delayed instability and enhanced energy absorption in some cases. This behavior suggests a more stable plastic deformation response, likely due to reduced residual stresses, fewer inter-layer defects, and more uniform strain distribution. This also indicate enhanced strain-hardening capacity and improved microstructural integrity, particularly in high-performing samples such as 27. Yield strength values for both groups fall in the range of approximately 300–340 MPa, with strain at failure between 0.18 and 0.25, both of which align closely with published values for AM AlSi10Mg under compression in literature.

While the 60 µm group shows greater variability, it demonstrates the potential for high performance when process parameters are optimized. The 40 µm group, meanwhile, offers more consistent mechanical response, making it potentially favorable in applications requiring predictable compressive strength and deformation.

4.5. Cost analysis

From an economic point of view, the biggest advantage of using Powder Bed Fusion technologies is that small production lots are comparatively inexpensive. The reason why machine operators and engineers can reduce the overall additive component costs is, first and foremost, the possibility to design and produce physical models in few hours in the same working day. Thus, it is possible to produce custom components or small series directly and without mold.

Further, this also suggests a short production chain since the time from design to marketing phase seriously decreases. L-PBF, also offers the capability of only producing what is needed, which significantly lowers the costs of material storage for the purpose of obsolescence manufactured in order to economize on production.

L-PBF is also synonymous with minimal processing waste that equates to reducing raw material purchasing cost and material disposal. This singularity, compared to traditional manufacturing processes, completely flips the view of the materials utilized: by building an object layer by layer, with no material waste, the material cost is no longer directly proportional to the quantity of material used, but it is based entirely on the quantity of material consumed.

The result is a search for complex and lightened shapes enabled by the design freedom offered by the technology. Here, topological optimization can play a crucial role. Topological optimization is

a re-design process directed towards the optimal material distribution by modifying the component geometry in order to reduce its weight while optimizing its performances, considering the specific mechanical properties of the material and the project objectives.

The result will be a lightweight, efficient, and functional component that also impacts costs favorably. For example, in industrial uses where lighter components translate into fuel efficiency, such as in the aerospace industry, the cost to be preserved decreases because of weight reduction. According to these considerations, this section will look at manufacturing cost with an estimated cost breakdown, calculated utilizing the cost model established in chapter 2.

A mechanical component that reflects variation in product size, geometry, and application is analyzed in production cost. All manufacturing costs and build time estimations were carried out considering Print sharp 250 machine. The proposed cost model allows computing the build time (T_b), the machine cost (C_{mac}), the material cost (C_{mat}), the energy cost (C_{ene}), and the gas cost (C_{gas}).
The pre/post-processing costs ($C_{p/p}$) should also be considered carefully. These costs are due to material preparation and secondary finishing operations.[104]

Pre-processing and post-processing common activities are supporting material removal, powder drying, surface texture enhancement, aesthetic, property improvements through non-thermal processes, property improvements through thermal processes. NIST learned that pre/post-processing costs represent 4% to 19% of all production costs depending on the employed AM technology and the alloy [81], therefore, for the presented calculation, such inputs were considered to account for 19% of the whole cost. Other configurations of costs emerging from building failure, machine maintenance, machine idleness, tools consumption, and inventory expenses are neglected.

4.5.1 Case Study

A mechanical components that reflects variation in product size, geometry, and application is analyzed in production cost. The chosen component is a turbine wheel, taken from a representative basket proposed by Baumers [105] . This part, particularly suitable for topological optimization, is typically employed in the aerospace field. Its complex shape and limited volume make the part ideal for production via the L-PBF process. Figure 63 shows a schematic representation of the piece. Two production scenarios are studied: the first uses parameters set number 1 ($BR = 6.72\ mm^3/s$), which are the parameters of sample 23 with 40-micron layer thickness and the second uses parameters set number 2 ($BR = 12.48\ mm^3/s$) which are the parameters of sample 27 with 60-micron layer thickness. Both sets can create parts with good mechanical properties, as seen in the previous section but set number 2 has almost double build rate.

Figure 64: Turbine wheel case study

Table 12: Turbine wheel data

Turbine wheel	
Dimensions	$54 \times 54 \times 28\ mm$
Volume	$20.618\ cm^3$

The cost model was applied considering a powder cost for AlSi10Mg equal to 90 $€/kg$ and the part volume equal to 20.618 cm^3; The recyclability and support material coefficients were both assumed equal to 1.5. Since the component shape is remarkably light, in this case, the possibility of producing a batch with 16 pieces is also considered to evaluate the advantages of accurately filling the building platform. Table 12 reports the results obtained in terms of build time and costs for the turbine wheel.

Table 13: Cost Analysis results

Set	*N. parts*	*BR* $[mm^3/s]$	T_b *[h]*	T_b *reduce*	$c_{material}$ *[€]*	$c_{operating}$ *[€]*	$c_{pre/post}$ *[€]*	c_{total} *[€]*	c_{part} *[€]*	*savings*
1	1	6.72	1.69	-	11.19	762.76	181.54	955.49	955.49	-
1	16	6.72	14.47	46.5%	179.04	6548.25	1578	8305.29	519.08	45.7%
2	1	12.48	1.01	40.2%	11.19	457.07	109.84	578.1	578.1	39.5%
2	16	12.48	7.9	70.8%	179.04	3575.07	880.59	4634.7	289.67	69.7%

Calculations for single unit production of first set is as following:

$$\boldsymbol{C_{job} = C_{material} + C_{operating} = m_{material} \cdot P_{powder} + \dot{C}_{operating} \cdot T_{bld}}$$

$$\boldsymbol{C_{material} = K_s \cdot K_r \cdot V_{part} \cdot \rho_{material} \cdot P_{powder}}$$

- $K_r = 1.5$ Support material coefficient

- $K_s = 1.5$ Recyclability coefficient
- $P_{powder} = 90\ \left[\frac{€}{Kg}\right]$ Powder price

$$C_{material} = 1.5 \cdot 1.5 \cdot 20.618\ [cm^3] \cdot 0.00268\ \left[\frac{kg}{cm^3}\right] \cdot 90\ \left[\frac{€}{kg}\right] = 11.189€$$

$$\dot{\boldsymbol{C}}_{\boldsymbol{operating}} = \frac{\boldsymbol{P}}{\boldsymbol{hy} \cdot \boldsymbol{ay}} + \boldsymbol{P_{el}} \cdot \boldsymbol{C_{el}} + \boldsymbol{P_{gas}} \cdot \boldsymbol{C_{gas}}$$

- $P = 450000$ [€] machine's purchase price
- $hy = 5000\ [\frac{h}{y}]$ machine's annual production hours
- $ay = 5\ [y]$ machine's amortization time
- $P_{el} = 0.16\ [\frac{€}{kWh}]$ and $P_{gas} = 3\ [\frac{€}{m^3}]$ electricity and gas prices
- $C_{el} = 8\ [\frac{kWh}{h}]$ and C_{gas}=0.42 $[\frac{m^3}{h}]$ electricity and gas consumption rates

$$\dot{C}_{operating} = \frac{450000\ [€]}{5000\ [\frac{h}{y}] \cdot 5\ [y]} + 0.16\ \left[\frac{€}{kWh}\right] \cdot 8\ \left[\frac{kWh}{h}\right] + 3\ \left[\frac{€}{m^3}\right] \cdot 0.42\ \left[\frac{m^3}{h}\right] = 452.54\ \left[\frac{€}{h}\right]$$

$$\boldsymbol{T_{bld}} = \frac{\dfrac{\boldsymbol{V_{part}[mm^3]}}{\boldsymbol{BR}\left[\dfrac{\boldsymbol{mm^3}}{\boldsymbol{s}}\right]} + \dfrac{\boldsymbol{Part\ height[mm]}}{\boldsymbol{Layer\ thickness[mm]}} \cdot \boldsymbol{T_{rc}}\ [\boldsymbol{s}]}{\boldsymbol{3600}\ [\frac{\boldsymbol{s}}{\boldsymbol{h}}]}$$

- $T_{rc} = 12\ [s]$ Recoating time

$$T_{bld} = \frac{\dfrac{20618\ [mm^3]}{6.72\left[\dfrac{mm^3}{s}\right]} + \dfrac{10\ [mm]}{0.04\ [mm]} \cdot 12\ [s]}{3600\ [\frac{s}{h}]} = 1.685\ [h]$$

Table 12 provides a comparative analysis of the cost and build time for manufacturing a turbine wheel using two different process parameter sets. The key observations from the table indicate that increasing the build rate and batch size significantly enhances cost efficiency.

Firstly, set 2, which operates at a higher build rate (12.48 mm³/s) compared to Set 1 (6.72 mm³/s), achieves a 40.2% reduction in build time for single-part production and a 70.8% reduction for

batch production (16 parts per build cycle). This demonstrates that higher build rates effectively reduce the total manufacturing time, making the process more efficient.

Secondly, the machine operation cost is the dominant cost factor, contributing the largest portion to the total cost per part. In single-part production, the machine cost for Set 1 is €762.76, whereas for Set 2, it is €457.07, leading to a 39.5% cost reduction. In batch production, where 16 parts are built simultaneously, the machine cost drops further to €6548.25 for Set 1 and €3575.07 for Set 2, achieving a 69.7% cost reduction. This highlights the importance of reducing build time to lower operational expenses.

Furthermore, batch production significantly reduces costs by distributing fixed machine operation and energy expenses over multiple parts. For instance, the total cost per part in a single production (Set 1) is €955.49, while in batch production, the cost per part drops to €519.08 (45.7% savings). In Set 2, batch production further reduces the cost per part to just €289.67 (69.7% savings). This confirms that maximizing the utilization of the build platform is a key strategy for cost efficiency.

Moreover, because the material cost remains constant (€11.19 per part) across both parameter sets, this suggests that cost savings are mainly driven by reduced machine time and energy consumption rather than material efficiency. Hence, optimizing build rate and machine usage is crucial for economic viability in Laser Powder Bed Fusion (L-PBF) manufacturing.

So, the best strategy for cost reduction in L-PBF manufacturing is to use higher build rates and maximize batch production. By implementing Set 2's parameters (higher build rate of 12.48 mm^3/s) and producing parts in batches, the cost per part can be minimized while maintaining high productivity and quality. This approach ensures that L-PBF remains a competitive and scalable option for industrial manufacturing.

Chapter 5: Conclusion

This study demonstrated that Laser Powder Bed Fusion (L-PBF) of AlSi10Mg can be effectively optimized by controlling key process parameters, particularly scan speed and layer thickness to achieve high part quality, mechanical performance, and productivity, while significantly reducing manufacturing cost.

Among 54 fabricated samples, scan speed and layer thickness had the most significant influence on part density. Laser power and hatch distance, by contrast, showed minimal statistical impact on relative density but played a notable role in other properties such as surface roughness and pore size.

Relative density peaked within a VED range of 35–45 J/mm³, with densification improving as VED increased up to a point. Beyond this optimal window, porosity increased again due to keyhole effects. 60 µm layer samples consistently exhibited higher densities and lower porosity compared to their 40 µm counterparts. Notably, density measurements using the Archimedes method were validated by both XCT and metallography analysis, confirming their accuracy and reinforcing the robustness of the dataset.

Porosity and Maximum Pore Size were closely linked to laser power and scan speed. Higher laser power significantly reduced pore size, while higher scan speed increased it. This confirms that adequate energy input is essential to suppress pore formation and achieve sound fusion. Hatch distance and layer thickness had negligible influence on pore size individually.

Surface roughness was strongly influenced by layer thickness, scan speed, and laser power. Smoother surfaces were obtained with thinner layers (40 µm), lower scan speeds (1200–1400 mm/s), and higher laser power (390 W). Surface roughness increased at higher build rates, especially for thicker layers, due to melt pool instability and balling effects.

Mechanical properties, assessed through compression testing, revealed that both 40 µm and 60 µm samples achieved high strength and ductility when built with optimized parameters. The best-performing sample (60 µm, Sample 27) reached 420 MPa UCS and 0.25 strain at failure. Higher density and lower porosity directly contributed to improved mechanical behavior. 60 µm samples showed more stable plastic deformation, likely due to reduced residual stresses and interlayer defects.

Cost analysis using a turbine wheel case study validated the economic feasibility of optimized L-PBF. Applying high-build-rate settings and batch production, the cost per part dropped by over 70%, from €955.49 to €289.67. Machine time was the dominant cost driver, making build rate and platform utilization critical levers for cost reduction.

To summarize:

- Scan speed and layer thickness were the most influential parameters, strongly affecting density, porosity, surface roughness, and mechanical strength. Optimal settings balanced quality and productivity.
- An optimal volumetric energy density (VED) range enabled full densification. Lower values caused lack of fusion, while higher values led to keyhole porosity.
- Laser power reduced pore size; scan speed increased it. Porosity and density measurements obtained by Archimedes method were confirmed by both X-ray Computed Tomography (XCT) and metallography, validating accuracy.
- Surface roughness improved with thin layers, moderate scan speed, and high laser power, but worsened with higher build rates, especially in thick-layer samples.
- Mechanical properties improved with higher density and lower porosity. Optimized thicker-layer samples showed stable deformation and high compressive strength.
- Cost analysis confirmed that higher build rates and batch production significantly reduced per-part cost without compromising part quality.

List of Acronyms

- **3D** Three-dimensional;
- **AED** Aria Energy Density
- **AI** Artificial Intelligence;
- **ASTM** American society for testing and materials;
- **AM** Additive Manufacturing;
- **ANN** Artificial Neutral Network;
- **ANOVA** Analysis of variance;
- **BR** Build Rate
- **CAD** Computer-Aided Design;
- **DED** Direct Energy Deposition;
- **DOE** Design Of Experiment;
- **DMLS** Direct Metal Laser Sintering;
- **EBM** Electron Beam Melting;
- **GCF** Geometric Conductance Factor
- **ML** Machine Learning;
- **NIST** National institute of standards and technology;
- **HIP** Hot Isostatic Pressing;
- **LED** Linear Energy Density
- **L-PBF** Laser-Powder Bed Fusion;
- **OM** Optical Microscope;
- **PBF** Powder Bed Fusion;
- **PSD** Particle Size Distribution;
- **RSM** Response Surface Methodology;
- **SEC** Specific Energy Consumption;
- **SLS** Selective Laser Sintering;
- **STL** Stereolithography;
- **SLM** Selective Laser Melting;
- **UCS** Ultimate Compression Strength;
- **UTS** Ultimate Tensile Strength;
- **VED** Volumetric Energy Density;
- **W-EDM** Wire Electrical Discharge Machine;
- **XCT** X-ray Computed Tomography;
- **YS** Yield Strength;

Bibliography

[1] A. Aversa, A. Saboori, G. Marchese, L. Iuliano, M. Lombardi, and P. Fino, “Recent Progress in Beam-Based Metal Additive Manufacturing from a Materials Perspective: A Review of Patents,” *J Mater Eng Perform*, vol. 30, no. 12, pp. 8689–8699, Dec. 2021, doi: 10.1007/s11665-021-06273-3.

[2] V. Matilainen, H. Piili, A. Salminen, T. Syvänen, and O. Nyrhilä, “Characterization of Process Efficiency Improvement in Laser Additive Manufacturing,” *Phys Procedia*, vol. 56, pp. 317–326, 2014, doi: 10.1016/j.phpro.2014.08.177.

[3] I. Gibson, D. W. Rosen, and B. Stucker, *Additive Manufacturing Technologies*. Boston, MA: Springer US, 2010. doi: 10.1007/978-1-4419-1120-9.

[4] “ASTM International - ASTM F3187-16 - Standard Guide for Directed Energy Deposition of Metals | GlobalSpec’. Accessed: May 05, 2024. [Online]. Available: https://standards.globalspec.com/std/3862763/astm-f3187-16.”

[5] L. Ladani and M. Sadeghilaridjani, “Review of Powder Bed Fusion Additive Manufacturing for Metals,” *Metals (Basel)*, vol. 11, no. 9, p. 1391, Sep. 2021, doi: 10.3390/met11091391.

[6] S. L. Sing, J. An, W. Y. Yeong, and F. E. Wiria, “Laser and electron-beam powder-bed additive manufacturing of metallic implants: A review on processes, materials and designs,” *Journal of Orthopaedic Research*, vol. 34, no. 3, pp. 369–385, Mar. 2016, doi: 10.1002/jor.23075.

[7] G. Demeneghi, P. Gradl, J. R. Mayeur, and K. Hazeli, “GRCop-42: Comparison between laser powder bed fusion and laser powder direct energy deposition,” *Additive Manufacturing Letters*, vol. 10, p. 100224, Jul. 2024, doi: 10.1016/j.addlet.2024.100224.

[8] M. Li, W. Du, A. Elwany, Z. Pei, and C. Ma, “Metal Binder Jetting Additive Manufacturing: A Literature Review,” *J Manuf Sci Eng*, vol. 142, no. 9, Sep. 2020, doi: 10.1115/1.4047430.

[9] A. Mazeeva, D. Masaylo, G. Konov, and A. Popovich, “Multi-Metal Additive Manufacturing by Extrusion-Based 3D Printing for Structural Applications: A Review,” *Metals (Basel)*, vol. 14, no. 11, p. 1296, Nov. 2024, doi: 10.3390/met14111296.

[10] M. H. Mosallanejad, A. Abdi, F. Karpasand, N. Nassiri, L. Iuliano, and A. Saboori, “Additive Manufacturing of Titanium Alloys: Processability, Properties, and Applications,” *Adv Eng Mater*, vol. 25, no. 24, Dec. 2023, doi: 10.1002/adem.202301122.

[11] M. M. Attallah, R. Jennings, X. Wang, and L. N. Carter, “Additive manufacturing of Ni-based superalloys: The outstanding issues,” *MRS Bull*, vol. 41, no. 10, pp. 758–764, Oct. 2016, doi: 10.1557/mrs.2016.211.

[12] R. Montanari, A. Palombi, M. Richetta, and A. Varone, “Additive Manufacturing of Aluminum Alloys for Aeronautic Applications: Advantages and Problems,” *Metals (Basel)*, vol. 13, no. 4, p. 716, Apr. 2023, doi: 10.3390/met13040716.

[13] G. Mani, D. Porter, S. Collins, T. Schatz, A. Ornberg, and R. Shulfer, “A review on manufacturing processes of cobalt-chromium alloy implants and its impact on corrosion resistance and biocompatibility,” *J Biomed Mater Res B Appl Biomater*, vol. 112, no. 6, Jun. 2024, doi: 10.1002/jbm.b.35431.

[14] J. Elambasseril, J. Rogers, C. Wallbrink, D. Munk, M. Leary, and M. Qian, “Laser powder bed fusion additive manufacturing (LPBF-AM): the influence of design features and LPBF variables on surface topography and effect on fatigue properties,” *Critical Reviews in Solid State and Materials Sciences*, vol. 48, no. 1, pp. 132–168, Jan. 2023, doi: 10.1080/10408436.2022.2041396.

[15] B. Brown, C. Lough, D. Wilson, J. Newkirk, and F. Liou, “Atmosphere Effects in Laser Powder Bed Fusion: A Review,” *Materials*, vol. 17, no. 22, p. 5549, Nov. 2024, doi: 10.3390/ma17225549.

[16] E. M. Sefene, “State-of-the-art of selective laser melting process: A comprehensive review,” Apr. 01, 2022, *Elsevier B.V.* doi: 10.1016/j.jmsy.2022.04.002.

[17] M. A. Mahmood, A. Ullah, M. Shah, A. U. Rehman, M. U. Salamci, and M. Khraisheh, “Thermal Post-Processing Techniques for Additive Manufacturing,” in *Handbook of Post-Processing in Additive Manufacturing*, New York: CRC Press, 2023, pp. 87–110. doi: 10.1201/9781003276111-5.

[18] M. J. Mirzaali, A. Azarniya, S. Sovizi, J. Zhou, and A. A. Zadpoor, “Lattice structures made by laser powder bed fusion,” in *Fundamentals of Laser Powder Bed Fusion of Metals*, Elsevier, 2021, pp. 423–465. doi: 10.1016/B978-0-12-824090-8.00020-2.

[19] A. V. Gusarov *et al.*, “On productivity of laser additive manufacturing,” *J Mater Process Technol*, vol. 261, pp. 213–232, Nov. 2018, doi: 10.1016/j.jmatprotec.2018.05.033.

[20] N. D. Dejene and H. G. Lemu, “Current Status and Challenges of Powder Bed Fusion-Based Metal Additive Manufacturing: Literature Review,” *Metals (Basel)*, vol. 13, no. 2, p. 424, Feb. 2023, doi: 10.3390/met13020424.

[21] D. Wang *et al.*, “Influence mechanism of laser delay on internal defect and surface quality in stitching region of 316L stainless steel fabricated by dual-laser selective laser melting,” *J Manuf Process*, vol. 94, pp. 35–48, May 2023, doi: 10.1016/j.jmapro.2023.03.051.

[22] R. Mertens, S. Dadbakhsh, J. Van Humbeeck, and J.-P. Kruth, “Application of base plate preheating during selective laser melting,” *Procedia CIRP*, vol. 74, pp. 5–11, 2018, doi: 10.1016/j.procir.2018.08.002.

[23] Y. Jia, C. Zeng, and J. Xue, “Scanning strategy optimization for the selective laser melting additive manufacturing of Ti6Al4V,” *Engineering Research Express*, vol. 5, no. 1, p. 015041, Mar. 2023, doi: 10.1088/2631-8695/acbd12.

[24] T. Shi, J. Sun, J. Li, G. Qian, and Y. Hong, “Machine learning based very-high-cycle fatigue life prediction of AlSi10Mg alloy fabricated by selective laser melting,” *Int J Fatigue*, vol. 171, p. 107585, Jun. 2023, doi: 10.1016/j.ijfatigue.2023.107585.

[25] D. J. S. Agron, D.-S. Kim, J.-M. Lee, and M. Almendrala, “Smart Monitoring Program for Selective Laser Melting 3D Printing Technology,” in *2023 IEEE 17th International Conference on Semantic Computing (ICSC)*, IEEE, Feb. 2023, pp. 337–340. doi: 10.1109/ICSC56153.2023.00069.

[26] A. V. Gusarov *et al.*, “On productivity of laser additive manufacturing,” *J Mater Process Technol*, vol. 261, pp. 213–232, Nov. 2018, doi: 10.1016/j.jmatprotec.2018.05.033.

[27] J. P. Oliveira, A. D. LaLonde, and J. Ma, “Processing parameters in laser powder bed fusion metal additive manufacturing,” *Mater Des*, vol. 193, p. 108762, Aug. 2020, doi: 10.1016/j.matdes.2020.108762.

[28] M. Marrey, E. Malekipour, H. El-Mounayri, and E. J. Faierson, “A Framework for Optimizing Process Parameters in Powder Bed Fusion (PBF) Process Using Artificial Neural Network (ANN),” *Procedia Manuf*, vol. 34, pp. 505–515, 2019, doi: 10.1016/j.promfg.2019.06.214.

[29] M. Roccetti Campagnoli, M. Galati, and A. Saboori, “On the processability of copper components via powder-based additive manufacturing processes: Potentials, challenges and feasible solutions,” *J Manuf Process*, vol. 72, pp. 320–337, Dec. 2021, doi: 10.1016/j.jmapro.2021.10.038.

[30] A. Behjat *et al.*, “Microstructure-electrochemical behavior relationship in post processed AISI316L stainless steel parts fabricated by laser powder bed fusion,” *Journal of Materials Research and Technology*, vol. 23, pp. 3294–3311, Mar. 2023, doi: 10.1016/j.jmrt.2023.01.229.

[31] J. P. Pragana *et al.*, “Influence of processing parameters on the density of 316L stainless steel parts manufactured through laser powder bed fusion,” *Proc Inst Mech Eng B J Eng Manuf*, vol. 234, no. 9, pp. 1246–1257, Jul. 2020, doi: 10.1177/0954405420911768.

[32] S. Cacace and Q. Semeraro, “Improvement of SLM Build Rate of A357 alloy by optimizing Fluence,” *J Manuf Process*, vol. 66, pp. 115–124, Jun. 2021, doi: 10.1016/j.jmapro.2021.03.043.

[33] A. Leicht, M. Rashidi, U. Klement, and E. Hryha, “Effect of process parameters on the microstructure, tensile strength and productivity of 316L parts produced by laser powder bed fusion,” *Mater Charact*, vol. 159, p. 110016, Jan. 2020, doi: 10.1016/j.matchar.2019.110016.

[34] C. Keller, M. Mokhtari, B. Vieille, H. Briatta, and P. Bernard, “Influence of a rescanning strategy with different laser powers on the microstructure and mechanical properties of Hastelloy X elaborated by powder bed fusion,” *Materials Science and Engineering: A*, vol. 803, p. 140474, Jan. 2021, doi: 10.1016/j.msea.2020.140474.

[35] M. L. Montero-Sistiaga, S. Pourbabak, J. Van Humbeeck, D. Schryvers, and K. Vanmeensel, “Microstructure and mechanical properties of Hastelloy X produced by HP-SLM (high power selective laser melting),” *Mater Des*, vol. 165, p. 107598, Mar. 2019, doi: 10.1016/j.matdes.2019.107598.

[36] H. Yeung, B. Lane, and J. Fox, “Part geometry and conduction-based laser power control for powder bed fusion additive manufacturing,” *Addit Manuf*, vol. 30, p. 100844, Dec. 2019, doi: 10.1016/j.addma.2019.100844.

[37] F. Yilan, R. Ekici, and L. Urtekin, “Recent advances in the AlSi10Mg materials fabrication by selective laser melting: process parameters, optimization, low-velocity and ballistic impact responses,” 2024, *Springer Science and Business Media Deutschland GmbH*. doi: 10.1007/s40964-024-00856-x.

[38] A. Leicht, M. Fischer, U. Klement, L. Nyborg, and E. Hryha, “Increasing the Productivity of Laser Powder Bed Fusion for Stainless Steel 316L through Increased Layer Thickness,” *J Mater Eng Perform*, vol. 30, no. 1, pp. 575–584, Jan. 2021, doi: 10.1007/s11665-020-05334-3.

[39] J. P. Pragana *et al.*, “Influence of processing parameters on the density of 316L stainless steel parts manufactured through laser powder bed fusion,” *Proc Inst Mech Eng B J Eng Manuf*, vol. 234, no. 9, pp. 1246–1257, Jul. 2020, doi: 10.1177/0954405420911768.

[40] N. Singh, P. Hameed, R. Ummethala, G. Manivasagam, K. G. Prashanth, and J. Eckert, “Selective laser manufacturing of Ti-based alloys and composites: impact of process parameters, application trends, and future prospects,” *Mater Today Adv*, vol. 8, p. 100097, Dec. 2020, doi: 10.1016/j.mtadv.2020.100097.

[41] H. Yeung, B. Lane, and J. Fox, “Part geometry and conduction-based laser power control for powder bed fusion additive manufacturing,” *Addit Manuf*, vol. 30, p. 100844, Dec. 2019, doi: 10.1016/j.addma.2019.100844.

[42] J. Liu *et al.*, “Effect of scanning speed on the microstructure and mechanical behavior of 316L stainless steel fabricated by selective laser melting,” *Mater Des*, vol. 186, p. 108355, Jan. 2020, doi: 10.1016/j.matdes.2019.108355.

[43] M. F. Sadali, M. Z. Hassan, F. Ahmad, H. Yahaya, and Z. A. Rasid, “Influence of selective laser melting scanning speed parameter on the surface morphology, surface roughness, and micropores for manufactured Ti6Al4V parts,” *J Mater Res*, vol. 35, no. 15, pp. 2025–2035, Aug. 2020, doi: 10.1557/jmr.2020.84.

[44] W. Yuan, H. Chen, T. Cheng, and Q. Wei, “Effects of laser scanning speeds on different states of the molten pool during selective laser melting: Simulation and experiment,” *Mater Des*, vol. 189, p. 108542, Apr. 2020, doi: 10.1016/j.matdes.2020.108542.

[45] J. Mei *et al.*, “Achieving Superior Strength and Ductility of AlSi10Mg Alloy Fabricated by Selective Laser Melting with Large Laser Power and High Scanning Speed,” Oct. 01, 2022, *Springer*. doi: 10.1007/s40195-022-01410-w.

[46] R. Gunnerek, Z. Chen, and E. Hryha, “Impact of high-productivity process parameters in powder bed fusion – laser beam on microstructure of stainless steel 316L,” *European Journal of Materials*, vol. 3, no. 1, Dec. 2023, doi: 10.1080/26889277.2023.2292987.

[47] K. Guan, Z. Wang, M. Gao, X. Li, and X. Zeng, “Effects of processing parameters on tensile properties of selective laser melted 304 stainless steel,” *Mater Des*, vol. 50, pp. 581–586, Sep. 2013, doi: 10.1016/j.matdes.2013.03.056.

[48] H. Meier and Ch. Haberland, “Experimental studies on selective laser melting of metallic parts,” *Materwiss Werksttech*, vol. 39, no. 9, pp. 665–670, Sep. 2008, doi: 10.1002/mawe.200800327.

[49] Y. H. Zhou *et al.*, “Selective laser melting of Ti–22Al–25Nb intermetallic: Significant effects of hatch distance on microstructural features and mechanical properties,” *J Mater Process Technol*, vol. 276, p. 116398, Feb. 2020, doi: 10.1016/j.jmatprotec.2019.116398.

[50] F. Calignano, D. Manfredi, E. P. Ambrosio, L. Iuliano, and P. Fino, “Influence of process parameters on surface roughness of aluminum parts produced by DMLS,” *The International Journal of Advanced Manufacturing Technology*, vol. 67, no. 9–12, pp. 2743–2751, Aug. 2013, doi: 10.1007/s00170-012-4688-9.

[51] Z. Dong, Y. Liu, W. Wen, J. Ge, and J. Liang, “Effect of Hatch Spacing on Melt Pool and As-built Quality During Selective Laser Melting of Stainless Steel: Modeling and Experimental Approaches,” *Materials*, vol. 12, no. 1, p. 50, Dec. 2018, doi: 10.3390/ma12010050.

[52] S. Ehsan Saghaian *et al.*, “Effect of hatch spacing and laser power on microstructure, texture, and thermomechanical properties of laser powder bed fusion (L-PBF) additively manufactured NiTi,” *Opt Laser Technol*, vol. 149, p. 107680, May 2022, doi: 10.1016/j.optlastec.2021.107680.

[53] B. Feng *et al.*, “Effect of laser hatch spacing on the pore defects, phase transformation and properties of selective laser melting fabricated NiTi shape memory alloys,” *Materials Science and Engineering: A*, vol. 840, p. 142965, Apr. 2022, doi: 10.1016/j.msea.2022.142965.

[54] L. Zhou *et al.*, “Effect of scanning strategies on the microstructure and mechanical properties of Ti–15Mo alloy fabricated by selective laser melting,” *Vacuum*, vol. 205, p. 111454, Nov. 2022, doi: 10.1016/j.vacuum.2022.111454.

[55] R. Mertens, S. Clijsters, K. Kempen, and J. P. Kruth, “Optimization of Scan Strategies in Selective Laser Melting of Aluminum Parts with Downfacing Areas,” *Journal of Manufacturing Science and Engineering, Transactions of the ASME*, vol. 136, no. 6, Dec. 2014, doi: 10.1115/1.4028620.

[56] E. Ramirez-Cedillo *et al.*, “Process planning of L-PBF of AISI 316L for improving surface quality and relating part integrity with microstructural characteristics,” *Surf Coat Technol*, vol. 396, p. 125956, Aug. 2020, doi: 10.1016/j.surfcoat.2020.125956.

[57] C. Vyas, G. Poologasundarampillai, J. Hoyland, and P. Bartolo, “3D printing of biocomposites for osteochondral tissue engineering,” in *Biomedical Composites*, Elsevier, 2017, pp. 261–302. doi: 10.1016/B978-0-08-100752-5.00013-5.

[58] I. V. Zhirnov, P. A. Podrabinnik, M. Tokbergenov, A. A. Okunkova, and I. Y. Smurov, “Optical Monitoring and Diagnostics of SLM Processing for Single Track Formation from Co-Cr Alloy,” *Materials Science Forum*, vol. 834, pp. 51–60, Nov. 2015, doi: 10.4028/www.scientific.net/MSF.834.51.

[59] W. Shi, Y. Liu, X. Shi, Y. Hou, P. Wang, and G. Song, “Beam Diameter Dependence of Performance in Thick-Layer and High-Power Selective Laser Melting of Ti-6Al-4V,” *Materials*, vol. 11, no. 7, p. 1237, Jul. 2018, doi: 10.3390/ma11071237.

[60] Y. Song, Q. Sun, K. Guo, X. Wang, J. Liu, and J. Sun, “Effect of scanning strategies on the microstructure and mechanical behavior of 316L stainless steel fabricated by selective laser melting,” *Materials Science and Engineering: A*, vol. 793, p. 139879, Aug. 2020, doi: 10.1016/j.msea.2020.139879.

[61] Y. Zhao, C. Ding, H. Chen, and Y. Chen, “Study on SLM Forming Process, Residual Stress and Thermal Fatigue of 24CrNiMo Alloy Steel,” *Materials*, vol. 14, no. 16, p. 4383, Aug. 2021, doi: 10.3390/ma14164383.

[62] X. D. Nong, X. L. Zhou, Y. D. Wang, L. Yu, and J. H. Li, “Effects of geometry, location, and direction on microstructure and mechanical properties of 15–5PH stainless steel fabricated by directed energy deposition,” *Materials Science and Engineering: A*, vol. 821, p. 141587, Jul. 2021, doi: 10.1016/j.msea.2021.141587.

[63] Z. Wang, Z. Xiao, Y. Tse, C. Huang, and W. Zhang, “Optimization of processing parameters and establishment of a relationship between microstructure and mechanical properties of SLM titanium alloy,” *Opt Laser Technol*, vol. 112, pp. 159–167, Apr. 2019, doi: 10.1016/j.optlastec.2018.11.014.

[64] X. Shi, C. Yan, W. Feng, Y. Zhang, and Z. Leng, “Effect of high layer thickness on surface quality and defect behavior of Ti-6Al-4V fabricated by selective laser melting,” *Opt Laser Technol*, vol. 132, p. 106471, Dec. 2020, doi: 10.1016/j.optlastec.2020.106471.

[65] A. Cutolo, B. Neirinck, K. Lietaert, C. de Formanoir, and B. Van Hooreweder, “Influence of layer thickness and post-process treatments on the fatigue properties of CoCr scaffolds produced by laser powder bed fusion,” *Addit Manuf*, vol. 23, pp. 498–504, Oct. 2018, doi: 10.1016/j.addma.2018.07.008.

[66] C. de Formanoir *et al.*, “Increasing the productivity of laser powder bed fusion: Influence of the hull-bulk strategy on part quality, microstructure and mechanical performance of Ti-6Al-4V,” *Addit Manuf*, vol. 33, p. 101129, May 2020, doi: 10.1016/j.addma.2020.101129.

[67] F. Calignano, G. Cattano, and D. Manfredi, “Manufacturing of thin wall structures in AlSi10Mg alloy by laser powder bed fusion through process parameters,” *J Mater Process Technol*, vol. 255, pp. 773–783, May 2018, doi: 10.1016/j.jmatprotec.2018.01.029.

[68] R. Goodridge and S. Ziegelmeier, “Powder bed fusion of polymers,” in *Laser Additive Manufacturing*, Elsevier, 2017, pp. 181–204. doi: 10.1016/B978-0-08-100433-3.00007-5.

[69] Z. Gorgin Karaji, R. Hedayati, B. Pouran, I. Apachitei, and A. A. Zadpoor, “Effects of plasma electrolytic oxidation process on the mechanical properties of additively manufactured porous biomaterials,” *Materials Science and Engineering: C*, vol. 76, pp. 406–416, Jul. 2017, doi: 10.1016/j.msec.2017.03.079.

[70] M. H. Mosallanejad, S. Sanaei, M. Atapour, B. Niroumand, L. Iuliano, and A. Saboori, “Microstructure and Corrosion Properties of CP-Ti Processed by Laser Powder Bed Fusion under Similar Energy Densities,” *Acta Metallurgica Sinica (English Letters)*, vol. 35, no. 9, pp. 1453–1464, Sep. 2022, doi: 10.1007/s40195-022-01376-9.

[71] S. Defanti, C. Cappelletti, A. Gatto, E. Tognoli, and F. Fabbri, “Boosting Productivity of Laser Powder Bed Fusion for AlSi10Mg,” *Journal of Manufacturing and Materials Processing*, vol. 6, no. 5, Oct. 2022, doi: 10.3390/jmmp6050112.

[72] P. Alexander, S. Allen, and D. Dutta, “Part orientation and build cost determination in layered manufacturing,” *Computer-Aided Design*, vol. 30, no. 5, pp. 343–356, Apr. 1998, doi: 10.1016/S0010-4485(97)00083-3.

[73] N. Hopkinson and P. Dicknes, “Analysis of rapid manufacturing—using layer manufacturing processes for production,” *Proc Inst Mech Eng C J Mech Eng Sci*, vol. 217, no. 1, pp. 31–39, Jan. 2003, doi: 10.1243/095440603762554596.

[74] M. Ruffo and R. Hague, “Cost estimation for rapid manufacturing ’ simultaneous production of mixed components using laser sintering,” *Proc Inst Mech Eng B J Eng Manuf*, vol. 221, no. 11, pp. 1585–1591, Nov. 2007, doi: 10.1243/09544054JEM894.

[75] L. Rickenbacher, A. Spierings, and K. Wegener, “An integrated cost-model for selective laser melting (SLM),” *Rapid Prototyp J*, vol. 19, no. 3, pp. 208–214, Apr. 2013, doi: 10.1108/13552541311312201.

[76] D. Buchbinder, H. Schleifenbaum, S. Heidrich, W. Meiners, and J. Bültmann, “High power Selective Laser Melting (HP SLM) of aluminum parts,” in *Physics Procedia*, Elsevier B.V., 2011, pp. 271–278. doi: 10.1016/j.phpro.2011.03.035.

[77] D. Buchbinder, H. Schleifenbaum, S. Heidrich, W. Meiners, and J. Bültmann, “High Power Selective Laser Melting (HP SLM) of Aluminum Parts,” *Phys Procedia*, vol. 12, pp. 271–278, 2011, doi: 10.1016/j.phpro.2011.03.035.

[78] R. Poprawe, C. Hinke, W. Meiners, J. Schrage, S. Bremen, and S. Merkt, “SLM Production Systems: Recent Developments in Process Development, Machine Concepts and Component Design,” 2015, pp. 49–65. doi: 10.1007/978-3-319-12304-2_5.

[79] R. Poprawe, C. Hinke, W. Meiners, J. Schrage, S. Bremen, and S. Merkt, “SLM Production Systems: Recent Developments in Process Development, Machine Concepts and Component Design,” 2015, pp. 49–65. doi: 10.1007/978-3-319-12304-2_5.

[80] E. Atzeni and A. Salmi, “Economics of additive manufacturing for end-usable metal parts,” *The International Journal of Advanced Manufacturing Technology*, vol. 62, no. 9–12, pp. 1147–1155, Oct. 2012, doi: 10.1007/s00170-011-3878-1.

[81] D. S. Thomas and S. W. Gilbert, “Costs and Cost Effectiveness of Additive Manufacturing,” Gaithersburg, MD, Dec. 2014. doi: 10.6028/NIST.SP.1176.

[82] Z. Y. Liu, C. Li, X. Y. Fang, and Y. B. Guo, “Energy Consumption in Additive Manufacturing of Metal Parts,” *Procedia Manuf*, vol. 26, pp. 834–845, 2018, doi: 10.1016/j.promfg.2018.07.104.

[83] N. C. Igwe, I. Akhrif, M. El Jai, and B. El Fahime, “An experimental investigation of the influence of SLM input factors on the as-built AlSi10Mg surface quality,” *International Journal of Advanced Manufacturing Technology*, Jan. 2024, doi: 10.1007/s00170-024-14657-7.

[84] M. Taghian, M. H. Mosallanejad, E. Lannunziata, G. Del Greco, L. Iuliano, and A. Saboori, “Laser powder bed fusion of metallic components: Latest progress in productivity, quality, and cost perspectives,” *Journal of Materials Research and Technology*, vol. 27, pp. 6484–6500, Nov. 2023, doi: 10.1016/j.jmrt.2023.11.049.

[85] C. Guo *et al.*, “Effect of processing parameters on surface roughness, porosity and cracking of as-built IN738LC parts fabricated by laser powder bed fusion,” *J Mater Process Technol*, vol. 285, p. 116788, Nov. 2020, doi: 10.1016/j.jmatprotec.2020.116788.

[86] V. Mercurio, F. Calignano, and L. Iuliano, “Sustainable production of AlSi10Mg parts by laser powder bed fusion process,” *International Journal of Advanced Manufacturing Technology*, vol. 125, no. 7–8, pp. 3117–3133, Apr. 2023, doi: 10.1007/s00170-023-11004-0.

[87] R. Ghanavati, E. Lannunziata, E. Norouzi, S. Bagherifard, L. Iuliano, and A. Saboori, “Design and development of SS316L-IN718 functionally graded materials via laser powder bed fusion,” *Mater Lett*, vol. 349, p. 134793, Oct. 2023, doi: 10.1016/j.matlet.2023.134793.

[88] M. H. Mosallanejad, B. Niroumand, A. Aversa, D. Manfredi, and A. Saboori, “Laser Powder Bed Fusion in-situ alloying of Ti-5%Cu alloy: Process-structure relationships,” *J Alloys Compd*, vol. 857, p. 157558, Mar. 2021, doi: 10.1016/j.jallcom.2020.157558.

[89] A. Behjat, M. Shamanian, F. Sadeghi, L. Iuliano, and A. Saboori, “Additive manufacturing of a novel in-situ alloyed AISI316L-Cu stainless steel: Microstructure and antibacterial properties,” *Mater Lett*, vol. 355, p. 135363, Jan. 2024, doi: 10.1016/j.matlet.2023.135363.

[90] E. M. Kiass, K. Zarbane, and Z. Beidouri, “Optimizing AlSi10Mg Part Quality Aspects in Laser Powder Bed Fusion: A Literature Review,” Dec. 01, 2024, *Springer*. doi: 10.1007/s40516-024-00267-4.

[91] W. J. Sames, F. A. List, S. Pannala, R. R. Dehoff, and S. S. Babu, “The metallurgy and processing science of metal additive manufacturing,” *International Materials Reviews*, vol. 61, no. 5, pp. 315–360, Jul. 2016, doi: 10.1080/09506608.2015.1116649.

[92] A. Eliasu, A. Czekanski, and S. Boakye-Yiadom, “Effect of laser powder bed fusion parameters on the microstructural evolution and hardness of 316L stainless steel,” *The International Journal of Advanced Manufacturing Technology*, vol. 113, no. 9–10, pp. 2651–2669, Apr. 2021, doi: 10.1007/s00170-021-06818-9.

[93] M. R. Jandaghi, A. Saboori, L. Iuliano, and M. Pavese, “On the effect of rapid annealing on the microstructure and mechanical behavior of additively manufactured stainless steel by Laser Powder Bed Fusion,” *Materials Science and Engineering: A*, vol. 828, p. 142109, Nov. 2021, doi: 10.1016/j.msea.2021.142109.

[94] C. A. Biffi, J. Fiocchi, and A. Tuissi, “Laser Weldability of AlSi10Mg Alloy Produced by Selective Laser Melting: Microstructure and Mechanical Behavior,” *J Mater Eng Perform*, vol. 28, no. 11, pp. 6714–6719, Nov. 2019, doi: 10.1007/s11665-019-04402-7.

[95] I. Yadroitsev and I. Smurov, “Selective laser melting technology: From the single laser melted track stability to 3D parts of complex shape,” *Phys Procedia*, vol. 5, pp. 551–560, 2010, doi: 10.1016/j.phpro.2010.08.083.

[96] Q. B. Nguyen, D. N. Luu, S. M. L. Nai, Z. Zhu, Z. Chen, and J. Wei, “The role of powder layer thickness on the quality of SLM printed parts,” *Archives of Civil and Mechanical Engineering*, vol. 18, no. 3, pp. 948–955, Jul. 2018, doi: 10.1016/j.acme.2018.01.015.

[97] X. Shi *et al.*, “Performance of High Layer Thickness in Selective Laser Melting of Ti6Al4V,” *Materials*, vol. 9, no. 12, p. 975, Dec. 2016, doi: 10.3390/ma9120975.

[98] K. Kempen, L. Thijs, J. Van Humbeeck, and J. P. Kruth, “Mechanical Properties of AlSi10Mg Produced by Selective Laser Melting,” in *Physics Procedia*, Elsevier B.V., 2012, pp. 439–446. doi: 10.1016/j.phpro.2012.10.059.

[99] P. Ashwath, M. A. Xavior, A. Batako, P. Jeyapandiarajan, and J. Joel, “Selective laser melting of Al–Si–10Mg alloy: microstructural studies and mechanical properties assessment,” *Journal of Materials Research and Technology*, vol. 17, pp. 2249–2258, Mar. 2022, doi: 10.1016/j.jmrt.2022.01.135.

[100] K. Kempen, K. U. Leuven, E. Yasa, and M. Badrossamay, “Process Optimization and Microstructural Analysis for Selective Laser Melting of AlSi10Mg.” [Online]. Available: https://www.researchgate.net/publication/262698754

[101] G. A. Dzukey and K. Yang, “Process Parameter Optimization for Selective Laser Melting of 316L Stainless Steel Material using Taguchi’s Statistical Design of Experiment Procedure,” *International Journal of Engineering and Technology*, vol. 11, no. 1, pp. 6–13, Feb. 2019, doi: 10.21817/ijet/2019/v11i1/191101014.

[102] M. Letenneur, A. Kreitcberg, and V. Brailovski, “Optimization of Laser Powder Bed Fusion Processing Using a Combination of Melt Pool Modeling and Design of Experiment Approaches: Density Control,” *Journal of Manufacturing and Materials Processing*, vol. 3, no. 1, p. 21, Feb. 2019, doi: 10.3390/jmmp3010021.

[103] Alireza Moradi Ghasemabadi, “Machine Learning Assisted Laser-Powder Bed Fusion Process Optimization for AISI 316L-Cu Alloy.,” Corso di laurea magistrale in Ingegneria Meccanica (Mechanical Engineering), Politeccnico di torino, 2024. [Online]. Available: http://webthesis.biblio.polito.it/id/eprint/34357

[104] Giovanni Del Greco, “Correlation between the productivity and mechanical performance of AISI 316L parts produced via Laser powder bed fusion process.,” Corso di laurea magistrale in Ingegneria Meccanica (Mechanical Engineering), Politecnico di torino, 2021. [Online]. Available: http://webthesis.biblio.polito.it/id/eprint/20095

[105] C. T. R. W. I. A. E. R. and R. H. M. Baumers, “Combined build-time, energy consumption and cost estimation for direct metal laser sintering,” in *23rd Annual International Solid Freeform Fabrication Symposium (SFF)*, An Additive Manufacturing Conference, 2012, pp. 932–944. [Online]. Available: https://www.researchgate.net/publication/287719627_Combined_build-time_energy_consumption_and_cost_estimation_for_direct_metal_laser_sintering